REVIEW ARTICLE

Check for updates

Extraordinary optical fields in nanostructures: from sub-diffraction-limited optics to sensing and energy conversion

Xiangang Luo, ID *[a] Dinping Tsai, ID [bc] Min Gu ID [d] and Minghui Hong ID [e]

Along with the rapid development of micro/nanofabrication technology, the past few decades have seen the flourishing emergence of subwavelength-structured materials and interfaces for optical field engineering at the nanoscale. Three remarkable properties associated with these subwavelength-structured materials are the squeezed optical fields beyond the diffraction limit, gradient optical fields in the subwavelength scale, and enhanced optical fields that are orders of magnitude greater than the incident field. These engineered optical fields have inspired fundamental and practical advances in both engineering optics and modern chemistry. The first property is the basis of sub-diffraction-limited imaging, lithography, and dense data storage. The second property has led to the emergence of a couple of thin and planar functional optical devices with a reduced footprint. The third one causes enhanced radiation (e.g., fluorescence), scattering (e.g., Raman scattering), and absorption (e.g., infrared absorption and circular dichroism), offering a unique platform for single-molecule-level biochemical sensing, and high-efficiency chemical reaction and energy conversion. In this review, we summarize recent advances in subwavelength-structured materials that bear extraordinary squeezed, gradient, and enhanced optical fields, with a particular emphasis on their optical and chemical applications. Finally, challenges and outlooks in this promising field are discussed.

[a] State Key Laboratory of Optical Technologies on Nano-Fabrication and Micro-Engineering, Institute of Optics and Electronics, Chinese Academy of Sciences, Chengdu, 610209, China. E-mail: lxg@ioe.ac.cn

[b] Research Center for Applied Sciences, Academia Sinica, Taipei, Taiwan. E-mail: dptasi@sinica.edu.tw

[c] Department of Physics, National Taiwan University, Taipei, Taiwan

[d] Artificial-Intelligence Nanophotonics Laboratory, School of Science, RMIT University, Melbourne, VIC 3001, Australia. E-mail: min.gu@rmit.edu.au

[e] Department of Electrical & Computer Engineering, National University of Singapore, Engineer Drive 3, 117576, Singapore. E-mail: elehmh@nus.edu.sg

Professor Xiangang Luo is currently the director of the State Key Laboratory of Optical Technologies on Nano-fabrication and Micro-engineering (SKLOTNM), in the Institute of Optics and Electronics (IOE), Chinese Academy of Sciences (CAS). He received his PhD from the Chinese Academy of Sciences in 2001. His research interests are micro/nano-optics, plasmonics, subwavelength electro-magnetics, and catenary optics. He has published more than 300 scientific papers and 100 patents in optics and related fields. He is an elected Fellow of OSA, SPIE, and IAPLE, and COS.

Xiangang Luo

Professor DinPing Tsai received his PhD degree in Physics from the University of Cincinnati, USA, in 1990. He has been the director and Distinguished Research Fellow of the Research Center for Applied Sciences, Academia Sinica since 2012. He is also a Distinguished Professor of Department of Physics at National Taiwan University. He is an elected Fellow of AAAS, APS, IEEE, JSAP, OSA, SPIE and EMA. His current research interests are nano-photonics, plasmonics, meta-materials, green photonics, quantum photonics, and their applications.

Dinping Tsai

1. Introduction

The wave nature of light manifests itself in the diffraction process, which hampers attempts to trap and confine light into a deep-subwavelength volume. As a consequence, a common dielectric lens cannot resolve two objects located closer than λ/2NA, where λ is the wavelength of light and NA is the numerical aperture of the lens. Meanwhile, a dielectric optical waveguide cannot support the stable propagation of light when its transverse dimension is too small compared with the wavelength. Technologies that can squeeze electromagnetic waves into tiny structures are thus highly desired and could yield a far-reaching influence on optical and other related sciences.[1,2]

Recent investigations have illustrated that the operation principle of metallic lens and waveguides is quite distinct from their dielectric counterparts, thus they could overcome the limitations above. When the free electronics in metallic structures interact with incoming photons, surface wave modes, which are better known as surface plasmon polaritons (SPPs), emerge. These can take various forms according to the structures of the metal, ranging from freely propagating electron density waves along metal surfaces to localized charge oscillations in metallic nanoantennas or nanoparticles (NPs).[3] The surface plasmon features fields that are tightly bound to the metal surface and decay rapidly into the free space region, involving three unique properties: squeezed optical fields beyond the diffraction limit, gradient optical fields in the subwavelength scale, and enhanced optical fields that are greater than the incident field by several orders of magnitude.

Since the optical fields in metallic nanostructures are confined to the surfaces, a strong energy loss exists as a result of the Ohmic damping and inter-band transition.[4] In order to overcome this, high-index dielectrics have attracted renewed attention in recent years.[5,6] Because of their considerable localizing ability and low-loss, widespread applications, such as flat lenses, sensors, and solar cells, have been intensively investigated.

1.1 Squeezed and enhanced optical fields

The interest in squeezed optical fields with the ability to penetrate into the subwavelength size was initiated in 1998, when the extraordinary optical transmission (EOT) effect was first reported.[7] As shown in Fig. 1a, by exciting surface plasmons, plane waves can be squeezed and transmitted through a sub-wavelength holes array, which is not possible with single holes.[8,9] The original work of Ebbesen et al. is thought of as the starting point of modern plasmonics.

Upon resonant excitation, the collective oscillation of free electrons gives rise to large local electric field enhancements.[10,11] The local electric field intensity is maximal at the metal surface
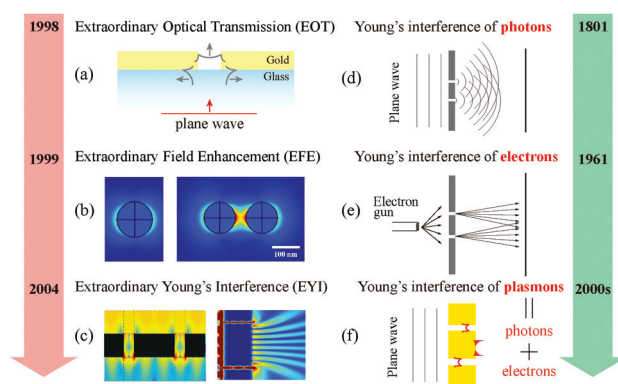

Fig. 1 (a–c) Three extraordinary effects in subwavelength structures. (d–f) Schematic of the Young's interferences of photons, electrons, and plasmons. (a) Reproduced from ref. 9 with permission. Copyright (2012) Macmillan Publishers Limited. (b) Reproduced from ref. 14 with permission. Copyright (2011) The Authors. (c) Left: Reproduced from ref. 30 with permission. Copyright (2004) American Institute of Physics. Right: Reproduced from ref. 31 with permission. Copyright (2007) Optical Society of America.

Min Gu

Professor Min Gu is a Distinguished Professor and associate deputy vice-chancellor at RMIT University and was a Laureate Fellow of the Australian Research Council. He is an author of four standard reference books and has over 500 publications in nano/biophotonics. He is an elected Fellow of the Australian Academy of Science and the Australian Academy of Technological Sciences and Engineering as well as Foreign Fellow of the Chinese Academy of Engineering. He is also an elected Fellow of the AIP, the OSA, the SPIE, the InstP, and the IEEE. He has been awarded the Einstein Professorship, and the W. H. (Beattie) Steel Medal, among others.

Minghui Hong

Professor Minghui Hong specializes in laser microprocessing and nanofabrication, optical engineering and laser applications. He is a Fellow of the Academy of Engineering, Singapore (FSEng), Fellow of Optical Society of America (OSA), Fellow of International Society for Optics and Photonics (SPIE), Fellow of International Academy of Photonics and Laser Engineering (IAPLE), and Fellow and Council Member of Institute of Engineers, Singapore (IES). Professor Hong is currently a full professor and the director of the Optical Science and Engineering Centre (OSEC), Department of Electrical and Computer Engineering, National University of Singapore. He is also the chairman of an NUS spin-off company Phaos Technology Pte. Ltd.

and then decays exponentially away from it, leading to both surface-enhanced Raman scattering (SERS) and other surface-enhanced spectroscopic processes. Fig. 1b illustrates a comparison of the field enhancement supported by a single metallic sphere and a spherical dimer. Compared with the field enhancement induced by localized plasmon resonance of a single sphere, the gap between two coupled particles forms a hot spot that results in an extraordinary field enhancement (EFE).[12–14] The isolated and coupled particles are referred to as the first and second generations of SERS hotspots.[15] It should be noted that although there is a strong correlation between the localized surface plasmon resonance (LSPR) and SERS wavelengths for single particles, the near-field SERS enhancement and far-field Rayleigh scattering may be separated in many coupled systems, such as in dimers and trimmers.[16] Besides SERS, enhanced optical fields are helpful to increase the performances of photovoltaic cells,[17–21] plasmonic or metal–semiconductor junction photocatalysts,[22–25] and other nonlinear processes.[26–29]

What distinguishes SPPs from regular photons is that SPPs have a much smaller wavelength than photons in free space at the same frequency, owing to the special dispersion curve lying below the light line.[32,33] Such a property has been demonstrated by Young's interference experiments in 2004 with subwavelength metallic slits.[30] Since the period of the interference fringes on a thin metallic film could be reduced to smaller than one-quarter of the vacuum wavelength rather than the half-wavelength of classic Young's interference, it is referred to as extraordinary Young's interference (EYI),[30,34] as shown in the left panel of Fig. 1c. Interestingly, the EYI is associated with the collective excitations of photons and electrons, namely SPPs. Different from other work focusing on the influence of SPPs on the transmission spectra,[35] here the interference patterns are more concerned, which could be recorded by photoresist. In numerical simulations, periodic boundary conditions were used, so that the double slits act as a basic building block for a plasmonic mask. Historically, the Young's interference of photons and electrons has provided valuable guidance on the development of wave optics and quantum physics.[36] Consequently, it is expected that the EYI effects may also have a significant impact on the development of subwavelength optics and engineering optics 2.0, as illustrated in Fig. 1d–f.[1,2,37–39]

Theoretical investigations have indicated that by decreasing the metallic film thickness, the SPPs at the two sides would couple with each other to form a catenary-shaped optical field, thus the effective wavelength of SPPs could be further shrunk to below one-tenth of the incidence wavelength.[33,34] This unique property means that coupled SPPs can surpass the diffraction limit of light and realize super-resolution imaging,[40,41] nanolithography,[30,42] and high-density data storage,[43–45] among others. For example, plasmonic superlenses, hyperlenses, and cavity lenses have evolved into the key components of plasmonic nanolithography, which further enables the optical fabrication of nanostructures with characteristic dimensions smaller than 22 nm.[33,46,47]

In parallel with the plasmonic approach, high-index dielectrics and semiconductors also provide an effective means to localize and enhance light.[6] Generally, low-loss dielectric structures are diffraction-limited and are therefore unable to focus light below $\lambda/2n_d$, where n_d is the refractive index of the dielectric material in which the optical mode is confined. Fortunately, the cavities in photonic crystals provide for the ultrafine confinement of light in lossless dielectric materials,[48–50] with an effective mode volume proportional to (λ/n_d).[3] By further introducing an engineered slot,[51] one can simultaneously enhance the maximum field intensity and localize the fields to a region of lower refractive index with an effective mode volume of $\sim 0.01\lambda^3$.

Recently, deeper subwavelength confinement was realized by a dielectric bowtie photonic crystal structure that supports mode volume commensurate with plasmonic elements.[52] A bowtie-shaped subwavelength dielectric inclusion added to the lattice holes enables redistribution of the optical mode to the tips of the bowtie as a result of the electromagnetic boundary conditions. Moreover, the cross-talk of silicon optical waveguides can be suppressed by introducing specially-designed subwavelength structures among dense waveguides, even with a separation distance smaller than $\lambda/2$.[53,54] Consequently, the density of the photonic circuit can be greatly improved.

1.2 Gradient optical fields

In many functional subwavelength optical devices, such as flat lenses and meta-holograms,[55–57] the optical fields should be space-variant to provide a gradient change of the wavefront. Basically, both plasmonic and dielectric materials have been investigated over the last two decades.

On the one hand, the short wavelength property of SPPs implies they possess a larger wavevector than the waves in free space,[58] which opens up new horizons for gradient phase modulation. SPP modes in metallic slits/holes can realize a tremendous phase change even within a subwavelength propagation distance. The local phase-engineering ability of subwavelength metallic slits has been illustrated by another EYI experiment using two subwavelength metallic slits with different widths (see the right panel of Fig. 1c),[31] where SPPs experienced different phase retardation through the double slits, thus causing a counterintuitive dark stripe at the center of the interference pattern. Based on the local phase engineering ability at a thin interface, the laws of refraction and reflection can be extended.[58,59] As a consequence, traditional bulky and curved optical devices can be replaced by thin and planar ones, opening a door to optical engineering at the subwavelength scale.[60,61]

On the other hand, dielectric nanopillars with a wavelength-scale thickness can also be utilized as highly efficient phase-shift elements.[62–65] Gradient-phase properties were achieved by engineering the diameter of nanopillars while maintaining the same periodicity[66] or *vice versa*.[67] This approach promises the miniaturization and improved performance of optical flat lenses with the ability to efficiently route (split/bend) the light over a broad range of wavelengths.[65,68,69] In addition, high-index dielectric disks that simultaneously support electric and magnetic resonances have also been utilized to construct Huygens' metasurfaces,[70] although they suffer from a narrow operation bandwidth.

In this review, we give an overview of the electromagnetic theories for localized fields generation and engineering, as well as their practical applications. In the introduction part, we present a brief description of the background. In Section 2, the basic theories of the extraordinary optical fields in isolated and coupled units are discussed. In Section 3, squeezed optical fields for sub-diffraction-limited imaging, nanolithography, and data storage are discussed in detail. In Section 4, gradient optical fields for dynamic lensing, directional radiating, and color filtering are reviewed. In Section 5, enhanced optical fields for biochemical sensing are summarized. In Section 6, we review the applications of enhanced optical fields in broadband absorption and high-efficiency energy conversion. In Section 7, a brief conclusion is given and future developing trends are discussed.

2. Theoretical basis

For a source-free and non-magnetic system, the Maxwell's wave equations can be written as:

$$\nabla^2 \mathbf{E} + \nabla \left[\mathbf{E} \cdot \frac{\nabla \varepsilon}{\varepsilon} \right] + k_0{}^2 \varepsilon \mu \mathbf{E} = 0$$

$$\nabla^2 \mathbf{H} + \frac{\nabla \varepsilon}{\varepsilon} \times (\nabla \times \mathbf{H}) + k_0{}^2 \varepsilon \mu \mathbf{H} = 0, \tag{1}$$

where $\mathbf{E}$ and $\mathbf{H}$ are the electric and magnetic fields, ε and μ are the permittivity and permeability of the constitutive materials, and k_0 is the wavenumber in free space. Generally, the second term in eqn (1) can be neglected for homogenous constitutive materials, which reduces the equation to the ordinary Helmholtz equation. Nevertheless, at the subwavelength scale, this term could not be ignored any more since the spatial variation of permittivity and permeability may occur on a scale far smaller than the wavelength of light,[60] which has led to many interesting solutions of wave equations, such as strongly localized waves, including surface plasmons,[71] and negatively refracted waves.[72] In order to clearly illustrate them, we respectively discuss the extraordinary optical fields in fundamental units and coupled structures in the subsequent sections.

2.1 Extraordinary optical fields in individual films and particles

For a thick metallic film whose thickness is larger than the decaying length of the SPP mode in it, the dispersion of SPP waves can be written as:

$$k_{\text{spp}} = \sqrt{\frac{\varepsilon_{\text{d}} \varepsilon_{\text{m}}}{\varepsilon_{\text{d}} + \varepsilon_{\text{m}}}} k_0, \tag{2}$$

where k_0 is the wavenumber of light in free space, and ε_{m} and ε_{d} are the dielectric constants of the metal and surrounding dielectric, respectively. Owing to its dispersion curve lying below the light line, SPP has an ultrashort effective wavelength, which ensures the localization of light below the classic diffraction limit.[33,73,74]
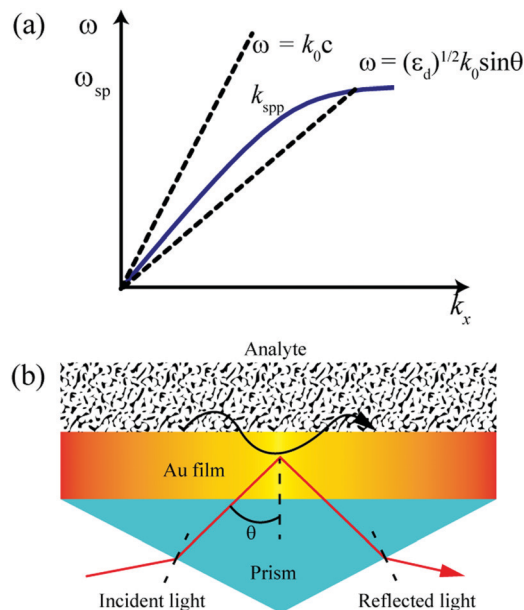

Fig. 2 (a) Schematic illustration of the wavevector-matching condition for SPR and (b) its application in biochemical sensing.

If light is incident on the metallic film with an angle θ, the wavevector of the light parallel to the surface is expressed as:

$$k_x = \sqrt{\varepsilon_{\text{d}}} k_0 \sin \theta. \tag{3}$$

As indicated in Fig. 2a, when $\varepsilon_{\text{d}} > 1$, a high wavevector can propagate in the prism and reach the metal–analyte interface. In this case, the evanescent coupling between the two sides of the metallic film can be neglected and there exists an angle of incidence where eqn (2) and (3) match with each other:

$$\theta_{\text{SPR}} = \sin^{-1} \left(\sqrt{\frac{\varepsilon_{\text{m}}}{\varepsilon_{\text{m}} + \varepsilon_{\text{d}}}} \right). \tag{4}$$

This surface plasmon resonance (SPR) angle is very sensitive to the refractive index of the surrounding medium. By measuring the intensity of the reflected light at that constant angle, changes in the refractive index of about 10^{-5} can be easily detected owing to the sharpness of the resonance spectrum, which can be utilized for high-sensitivity biochemical sensing (Fig. 2b).

When a surface plasmon is confined to a NP of a size comparable to the wavelength of light, it may excite localized surface plasmons. Different from propagating SPPs, the plasmonic modes in such structures change into a discrete set of resonant modes. For a metal spherical NP of radius $a \ll \lambda$, these modes have field patterns that correspond to the spherical harmonics, which would be expected from their symmetry. A full theoretical treatment of this is covered by the well-known Mie theory. However, the complete derivation is quite lengthy and beyond the scope of this review. Here, according to the quasistatic analysis of particle polarizability, the extinction spectrum of the metal sphere can be written as follows:[75]

$$\sigma_{\text{ext}} = \frac{24\pi^2 N a^3 \varepsilon_{\text{d}}{}^{3/2}}{\lambda \ln(10)} \left[\frac{\text{Im}(\varepsilon_{\text{m}})}{(\text{Re}(\varepsilon_{\text{m}}) + 2\varepsilon_{\text{d}})^2 + \text{Im}(\varepsilon_{\text{m}})^2} \right], \tag{5}$$

where N is the areal density of the NPs. From eqn (5), one can see that σ_{ext} approaches infinite when the dielectric function of the metal reaches the value $-2\varepsilon_d$, the so-called LSPR condition. Two important physical effects should be noted here. First, the optical extinction of Au NP has a maximum at the LSPR frequency, which can be much larger than their geometrical sizes. Second, this peak position depends on the refractive index of the surrounding medium. Thus, changes in the local environment—such as through the presence of an adsorbed species—should cause a shift in peak wavelength λ_{max}. This leads to the following relationship:[75]

$$\Delta\lambda_{max} = m\Delta n[1 - \exp(-2d/l_d)]. \qquad (6)$$

Here, m is the refractive-index sensitivity (nm per refractive index unit (RIU)) of the NPs, Δn is the change in refractive index induced by the adsorbate, d is the effective adsorbate layer thickness, and l_d is the characteristic field-decay length.

An intuitionistic way to understand the light–matter interaction in a nanostructure is taken from a vision of the separation of free charge carriers under the influence of an external electric field. This separation creates an additional field that oscillates at the same frequency as the external field, as indicated in Fig. 3.[76] Under the resonance condition, an extremely localized, enhanced light field is created close to the metal structure. Note that the enhancement factor strongly depends on the shape and size of the metallic nanostructures. High local field enhancement can be achieved by triangles and cones, owing to their sharp edges producing a strong concentration of free charge carriers at the apexes.[77]

Besides the metallic nanostructures, all-dielectric nano-structures with a high index have recently been adopted for the control of light in the near field. From the viewpoint of scattering theory, the field scattered by a single dielectric sphere with a radius of r_0 situated in homogeneous surroundings can be expanded into an infinite series of the vector spherical harmonics and can be fully described by the electric and magnetic Mie coefficients a_m and b_m of the expansion,

$$\sigma_{sca} = \frac{2\pi}{|k|^2} \sum_{m=1}^{\infty} (2m+1)\left(|a_m|^2 + |b_m|^2\right), \qquad (7)$$
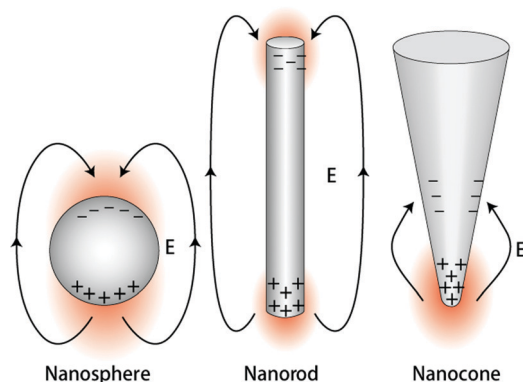

Fig. 3 Light field enhancement at metallic nanostructures. Illustration of some commonly used metallic nanostructures showing field enhancement. Reproduced from ref. 76 with permission. Copyright (2009) Nature Publishing group.

$$\sigma_{ext} = \frac{2\pi}{|k|^2} \sum_{m=1}^{\infty} (2m+1)\text{Re}(a_m + b_m), \qquad (8)$$

$$\sigma_{abs} = \sigma_{ext} - \sigma_{sca}, \qquad (9)$$

where the scattering electric field is proportional to:

$$a_m = \frac{n\psi_m(nx)\psi_m{}'(x) - \psi_m(x)\psi_m{}'(nx)}{n\psi_m(nx)\xi_m{}'(x) - \xi_m(x)\psi_m{}'(nx)}, \qquad (10)$$

and the scattering magnetic field is proportional to:

$$b_m = \frac{\psi_m(nx)\psi_m{}'(x) - n\psi_m(x)\psi_m{}'(nx)}{\psi_m(nx)\xi_m{}'(x) - n\xi_m(x)\psi_m{}'(nx)}, \qquad (11)$$

where $x = k_0 r_0$, and $\psi_m(x)$ and $\xi_m(x)$ are the Riccati–Bessel functions.[78]

The lowest-order scattering peak corresponds to the magnetic dipole mode of a nanosphere (Fig. 4a), which is induced by the coupling of incoming light to the circular displacement currents of the electric field.[6] The generated magnetic field is similar to that generated by the molecule-based magnets in the compound $[Ni(MeDABCO)_2Cl_3](ClO_4)$, as illustrated in Fig. 4b.[79] Since dielectric materials often have a smaller loss compared with metals in the optical regime, they are considered to be promising alternatives in many applications. Experimental observations of magnetic resonances at visible frequencies in silicon (Si)[80] and gallium arsenide (GaAs)[81] NPs have been reported.

The next higher-order mode in a high-index dielectric sphere is the electric dipole mode with a coefficient a_1. The simultaneous excitation of electric and magnetic resonance
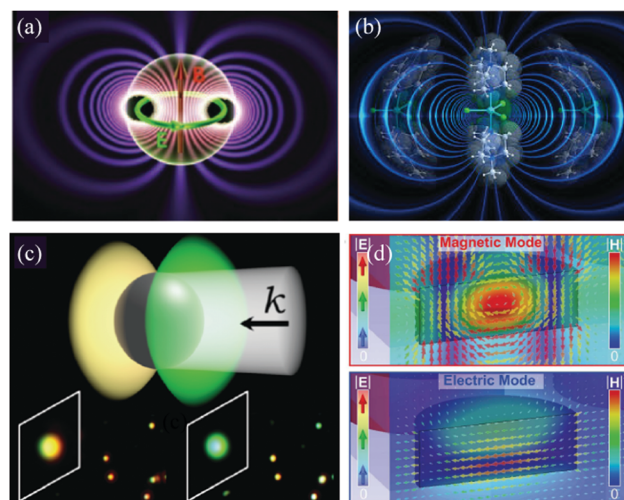

Fig. 4 (a) Structure of the electromagnetic fields near the magnetic dipole resonance. (b) Schematic of a molecular structure and the magnetic fields. (c) Unidirectional light scattering by a single dielectric NP for over-lapping electric and magnetic dipole resonances, where k is the wave-vector of the incident light. (d) Electric (colored arrows) and magnetic (plain-color coded) field distributions of the magnetic (top) and electric (bottom) modes of a silicon nanodisk. The two modes are dominated by strong magnetic and electric dipole moments, respectively. (a and c) Reproduced from ref. 6 with permission. Copyright (2016) AAAS. (b) Reproduced from ref. 79 with permission. Copyright (2018) Royal Society of Chemistry. (d) Reproduced from ref. 70 with permission. Copyright (2015) Wiley-VCH Verlag.

offers an effective method to manipulate the scattering properties. At some wavelengths that satisfy the Kerker condition,[82] the particles can act as 'Huygens' sources, scattering the whole energy in the forward direction, while for another wavelength range, light is almost completely scattered backward, as illustrated in Fig. 4c.[6]

While the Mie theory in its original formulation is strictly valid for spherical NPs only, Mie-type resonances can be observed for many different NP geometries. By adjusting the geometry of a dielectric disk, the electric and magnetic resonances can be superimposed at the same frequency, namely, spectrally overlapping crossed electric and magnetic dipole resonances of equal strength, as indicated in Fig. 4d.[70] Consequently, near-unity transmission with a phase coverage of 360° has been realized, which promises Huygens' metasurfaces.

Besides, when the dielectric sphere is larger than λ, it may focus light on the shadow-side surfaces of the microsphere, depending on the refractive index. The full width at half maximum (FWHM) of the beam stays below the diffraction limit and the intensity reaches a very high value. This beam has been called a photonic nanojet (PNJ) because of the analogy between the high-speed gradient of a jet in fluidic mechanics and the observed high light flux gradient.[83] These specific properties are not possessed by classical Gaussian beams generated by high NA objectives. PNJ provides a new means to detect and image nanostructures of a size well below the diffraction limit.[84]

2.2 Extraordinary optical fields in coupled films and particles

By arranging nanostructures in pairs and even more intricate multi-particle arrangements, one could realize complex antenna structures capable of directing light emission[85] and particle clusters that exhibit Fano-like resonances.[86–89] Plasmon hybridization theory (Fig. 5a),[90] inspired by molecular orbital theory (Fig. 5b),[91] has achieved great success in describing the near-field coupling of plasmonic interfaces or NPs.

When a metallic film is thin enough to be recognized as an insulator–metal–insulator (IMI) waveguide (Fig. 6a), the SPPs confined at the both sides of the film couple with each other and generate two new modes, the so-called symmetric mode and antisymmetric mode. Compared with the antisymmetric mode, the symmetric mode exhibits stronger field localization in the core, whose dispersion can be described by the following equation:

$$\tanh\left(\sqrt{\beta^2 - \varepsilon_m k_0^2}\, w/2\right) = -\frac{\varepsilon_d \sqrt{\beta^2 - \varepsilon_m k_0^2}}{\varepsilon_m \sqrt{\beta^2 - \varepsilon_d k_0^2}}. \quad (12)$$

While for the complementary structure of metallic film (Fig. 6a), *i.e.*, a metallic slit, or a metal–insulator–metal (MIM) waveguide, the antisymmetric mode has a larger propagation constant than that of the symmetric mode, which can be deduced from the following equation:

$$\tanh\left(\sqrt{\beta^2 - \varepsilon_d k_0^2}\, w/2\right) = -\frac{\varepsilon_d \sqrt{\beta^2 - \varepsilon_m k_0^2}}{\varepsilon_m \sqrt{\beta^2 - \varepsilon_d k_0^2}}. \quad (13)$$
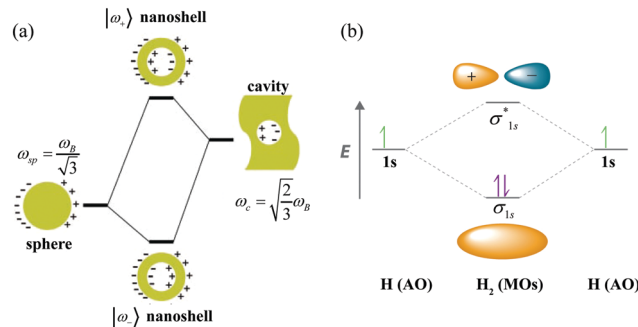

Fig. 5 (a) Plasmon hybridization theory: an energy-level diagram describes the plasmon hybridization in metal nanoshells resulting from the interaction between the sphere and cavity plasmons. The two nanoshell plasmons are an antisymmetrically coupled (antibonding) ω_+ plasmon mode and a symmetrically coupled (bonding) ω_- plasmon mode. (b) Molecular orbital theory: the two available electrons (one from each H atom) in this diagram fill the bonding σ_{1s} molecular orbital. Because the energy of the σ_{1s} molecular orbital is lower than those of the two H 1s atomic orbitals, the H_2 molecule is more stable (at a lower energy) than the two isolated H atoms. (a) Reproduced from ref. 90 with permission. Copyright (2003) AAAS. (b) Reproduced from ref. 91 with permission. Copyright (2013) The Authors.

As illustrated in eqn (13), the propagation constant depends on the gap width between the metal films,[59,92] thus gradient local phase modulation could be realized by varying the gap width, which is taken as one of the three approaches to realize the generalized Snell's law.[55] By further stacking metal–dielectric multilayers, SPPs may couple more strongly to form an effective material with hyperbolic dispersion,[93] in which light propagates nearly without diffraction.

From a viewpoint of near-field coupling, the field inside the core of the MIM waveguide can be expressed as a summation of two counter-propagating evanescent waves, as indicated in Fig. 6a and b:[34]

$$E_x \propto A \exp(i\beta x + \alpha z) + B \exp(i\beta x - \alpha z), \quad (14)$$

where $\beta^2 = \alpha^2 + \varepsilon k_0^2$, ε is the permittivity of the core material, and A and B are coefficients. For the symmetric mode of the MIM waveguide, A and B should be equal in amplitude and same in sign, thus the field profile exhibits a catenary shape (hyperbolic cosine function):

$$E_x \propto \exp(\alpha z) + \exp(-\alpha z) = 2\cosh(\alpha z). \quad (15)$$

A recent investigation showed that the catenary optical field is an intrinsic mode resulting from evanescent coupling, which must be considered in subwavelength metallic slits (Fig. 6b).[34] From another viewpoint, this catenary-shaped field is coincident with the physics behind the mechanical catenary, because both of them could be interpreted using the minimal potential energy principle. Interestingly, atomic coupling is very similar to electromagnetic coupling, since both of them are described by using evanescent wave functions,[91] as shown in Fig. 6c and d. In general, the catenary optical field is a basic property of the meta-surface-wave, which is a special waveform on structured surfaces with on-demand optical properties and which forms the core of engineering optics 2.0.[2,58,94]
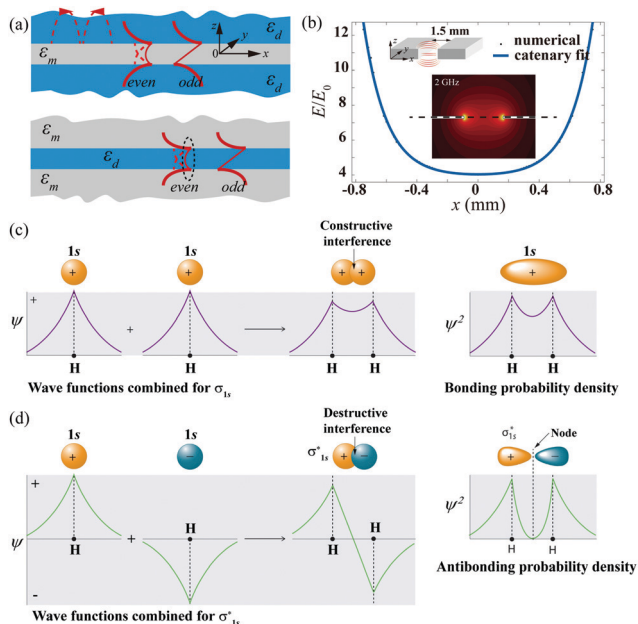
Fig. 6 (a) Coupled plasmonic modes in IMI (upper panel) and MIM (middle panel) waveguides. The dashed lines show the electric force lines. The solid curves show the amplitude of E_x for even and odd modes. For the even mode, E_x follows a catenary function. For the odd mode, H_y and E_z have a catenary shape (bottom panel). (b) Normalized E_x between two metallic sheets made of a perfect electric conductor (numerical), as well as the curve fitted using a hyperbolic cosine function (catenary fit). The fitted value for α is 6.639 mm^{-1}, which is about 158 times the vacuum wavenumber at 2 GHz. (c and d) Molecular orbitals formation of a bonding σ_{1s}, and an antibonding σ^*_{1s} for the H$_2$ molecule. (a and b) Reproduced from ref. 34 with permission. Copyright (2018) American Chemical Society. (c and d) Reproduced from ref. 91 with permission. Copyright (2013) The Authors.

Fig. 7 (a) Schematic illustration of a dimer of a subwavelength metallic sphere illuminated by a light polarized along their axes. (b) Left: Schematic arrangements of the transition dipoles. The red and orange arrows represent the in-line dipole along the dimer axial direction and the parallel dipole perpendicular to the dimer axial direction, respectively, which are superimposed on the molecular units. Right: Energy–resolved photon images for the five modes. (c) Simulated electric field distribution of the spherical metallic dimer with a separation of 2 nm. (d) SEM image of a silicon nanodisk dimer and (e) corresponding calculated electric-field enhancement. Scale bar: 100 nm. (a–c) Reproduced from ref. 95 with permission. Copyright (2015) Nature Publishing group. (d and e) Reproduced from ref. 96 with permission. Copyright (2015) Macmillan Publishers Limited.

When two nanospheres are placed close together (metallic dimer) and illuminated by a light polarized along their axes (Fig. 7a), all modes of the individual spheres couple to each other, just like the recently observed coherent dipole–dipole coupling in a molecule dimer (Fig. 7b).[95] Such near-field coupling generates a catenary-shaped field profile and provides field enhancement at a level far beyond what a single sphere can provide, as indicated in Fig. 7c.

Apart from the dimeric NPs, more complex nanoclusters (NCs), as an ordered assembly of coupled NPs, such as trimmers[97–99] and tetramers,[100,101] have also been developed. The coupling plasmonic modes in these structures play an important role in their high local-field enhancements and special spectra responses. Specifically, in the case of the trimer, the symmetry for the plasmonic modes should also be considered.[97,98] Fig. 8a–c show a plasmonic heptamer structure and its optical intensity distribution for both horizontally and vertically polarized pump light. The plasmonic NCs support unique spectral features known as Fano resonances due to the coupling between their subradiant and superradiant plasmonic modes.

Although high-field enhancement has been achieved in metallic NCs, it is generally accompanied by high optical loss and heating due to abso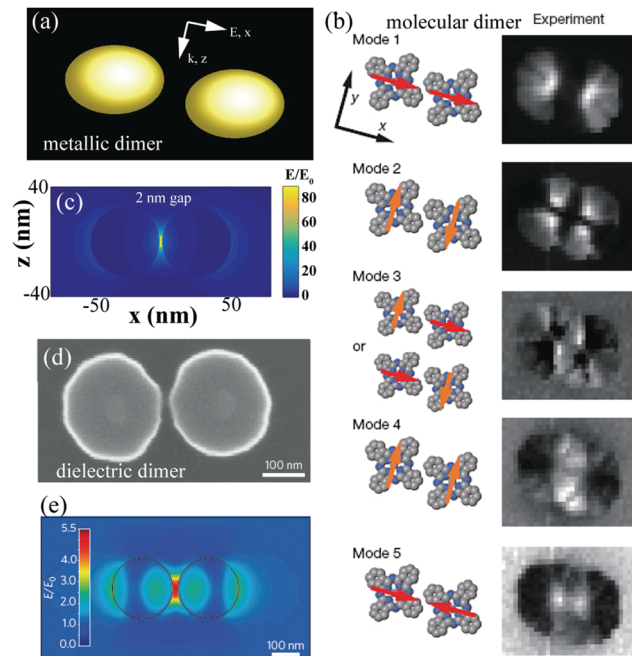rption in the metal. A novel non-plasmonic platform based on dielectric nanostructures with ultralow light-into-heat conversion was proposed, as indicated in Fig. 7d and e. Silicon dimers can produce both high SERS and surface-enhanced fluorescence (SEF), while at the same time generating a negligible temperature increase in their hot spots and surrounding environments.[96] Furthermore, it has been demonstrated that an asymmetric dimer of silicon NPs showed tunable directional scattering depending on the frequency of excitation.[102] Based on the directional scattering of an asymmetric dimer of silicon NPs, large-angle beam deflection and high numerical aperture lens have been demonstrated recently.[103,104]

Similar to the optical field confinement by NCs, surface electrons can be confined by "quantum corrals" on a metal surface, as indicated in Fig. 8d.[105] Recent investigations demonstrated that such electron confinement can also be realized based on individual ring-shaped [8]cycloparaphenylene (CPP) molecules, made up of eight paralinked phenylenes, which are the shortest-possible fragments of armchair carbon nanotubes, as displayed in Fig. 8e and f. Subsequently, it has been demonstrated that their all-dielectric counterparts also have the ability to generate strong local fields and sharp Fano resonances.[107] Light enhancement by quasi-bound states in the continuum in dielectric arrays has also been reported,[108] which represent
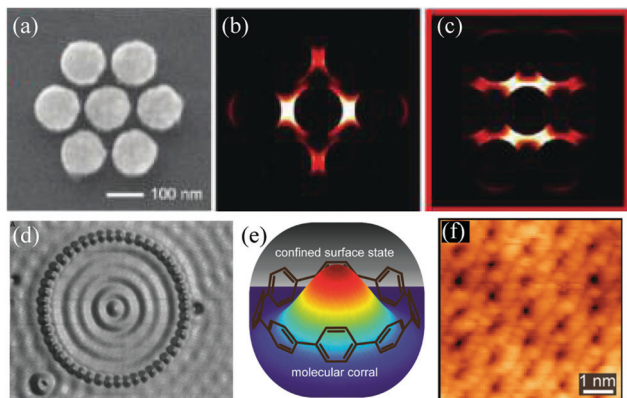
Fig. 8 (a) SEM image of plasmonic NCs and the optical intensity maps under the illumination of horizontally (b) and vertically (c) polarized pump light. (d) Spatial image of the eigenstates of a quantum corral made of a 48-atom Fe ring on the Cu(111) surface. Average diameter of the ring (atom center to atom center) is 142.6 Å. The ring encloses a defect-free region of the surface. (e) Schematic illustration of quantum confinement of surface electrons by [8]CPP molecules. (f) High-resolution scanning tunneling microscopy (STM) image of a well-ordered, two-dimensional crystal of [8]CPPs adsorbed on Au(111). (a–c) Reproduced from ref. 86 with permission. Copyright (2012) American Chemical Society. (d) Reproduced from ref. 105 with permission. Copyright (1993) AAAS. (e and f) Reproduced from ref. 106 with permission. Copyright (2016) American Chemical Society.
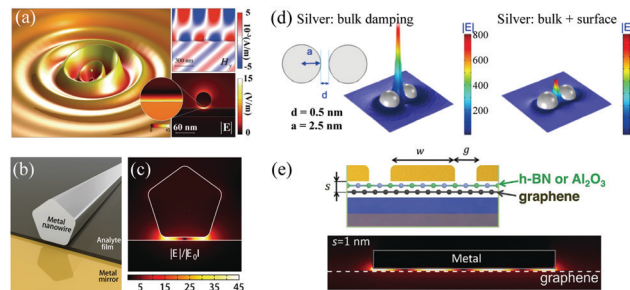
Fig. 9 (a) Simulation of a single-film-coupled NPs. Left: Relative electron surface density shows the excited surface plasmon polariton propagating over the metal film. The NP can be seen at the center. Upper right: A plane wave is incident at 75° from the normal on the NP. Lower right: A close-up of the near fields surrounding the nanosphere. (b) A metal nanowire is separated from a metal mirror by a thin film, whose thickness change can be precisely probed. (c) Local electric field distribution between the nanowire and metallic film at resonant frequency. (d) SPP field distribution in the silver dimer ($a = 2.5$ nm and $d = 0.5$ nm) taking into account only bulk damping and both bulk and surface damping at the dipole resonance $\lambda = 663$ nm. (e) Schematic of a metallic–graphene hybrid system and simulated plasmonic field magnitude profiles for a metal–graphene separation of 1 nm. (a) Reproduced from ref. 109 with permission. Copyright (2012) AAAS, (b and c) Reproduced from ref. 111 with permission. Copyright (2018) the authors. (d) Reproduced from ref. 116 with permission. Copyright (2017) American Chemical Society. (e) Reproduced from ref. 117 with permission. Copyright (2018) AAAS.

localized states with the eigenfrequency embedded into a continuum of propagating solutions.

Fig. 9a–c show some excellent local-field enhancement structures consisting of a plasmonic nanosphere or nanowire coupled to a flat, semi-infinite metal substrate with various nanogaps.[109–111] From electromagnetic theory, these configurations can be considered as a NP interacting with its mirror image. The enhancement factor continually increases with the shrinking of the gap until it is scaled down into the quantum regime, where a saturation effect appears.[112–115] At such a scale, the underlying assumption of the plasmonic material breaks down, that is, the quantum nature of the electrons and the nonlocal screening associated with them significantly alter the plasmonic response.[114]

Fig. 9d shows the influence of the quantum effect on the shape and magnitude of the optical field in the SPP mode of the same silver dimer.[118] The enhancement is reduced by almost 2 orders of magnitude when the quantum effect is taken into account compared with that analyzed by classic electromagnetic theory. It was also found that the plasmonic resonance undergoes a blue-shift with linewidth broadening when the size of NPs approaches a critical size, which is drastically different to the predictions of classical electromagnetism.[119] Two quantum phenomena, *i.e.*, electron tunneling between the two constituent particles, and a non-local effect, which is a manifestation of Landau damping, contribute to the ultimate response for limiting the maximally achievable field confinement.[114,116]

In other words, plasmons offer an appealing avenue to confine light; however, the quantum effects of the metallic nanostructures impose a trade-off between the optical field confinement and losses. Recently, Iranzo *et al.*[117] showed that a

graphene–insulator–metal heterostructure could overcome this trade-off and offer plasmon confinement down to the ultimate limit of the length scale of one atom, as shown in Fig. 9e. These ultraconfined plasmonic modes enable a route to new regimes of ultrastrong light–matter interactions.

3. Squeezed optical fields for sub-diffraction-limited imaging, lithography, and data storage

In 1873, Ernst Abbe[120] discovered a fundamental "diffraction limit" in optics: whenever an object is imaged by an optical system, such as the lens of a camera, the resolution Δ is limited by the wavelength of light, λ, and the numerical aperture (NA) of the objective lens to $\Delta = 0.61\lambda/\text{NA}$. The fundamental reason for this is that the near fields that contain all the finest details of an object decay rapidly with increasing distance. To achieve super-resolution microscopy, Synge conceived the idea of detecting the optical signal in the near field of the object in 1928,[121] which ultimately resulted in the development of scanning near-field optical microscopy (SNOM).[122] As one of the most popular microscopy techniques so far, SNOM forms its image with a high spatial resolution by scanning an ultrasharp tip in the vicinity of the object and collecting the signal point by point.[123–125]

3.1 Super-resolution lithography based on superlens, cavity lens, and hyperlens

In 1967, Victor Veselago[72] proposed a material that simultaneously possessed a negative electric permittivity and a negative

magnetic permeability, termed as a left-handed material or negative index metamaterial (an artificial material with physical properties not occurring in nature). Although a slab made of negative index material has the ability to realize perfect focusing without aberration, it is thought to be still diffraction limited, *i.e.*, the image resolution is restricted by the wavelength and aperture size. In 2000, the concept of a superlens for perfect imaging beyond the classic diffraction limit was proposed by John Pendry,[40] which could be simply implemented by a thin metallic film with negative permittivity. In essence, when the thickness of a metallic film is decreased to below 100 nm, the coupling of SPPs on both sides of the metallic film form a catenary optical fields and compensate the decaying of the evanescent wave, which contributes to super-resolution imaging in the optical band.[33,34]

In 2003, a patent was applied to realize nanolithography based on plasmonic effects,[126] where common light sources, such as the g-line (436 nm) and i-line (365 nm) spectra of a mercury lamp are utilized. In 2004, the proposal was experimentally validated at a wavelength of 436 nm, and 50 nm ($\sim \lambda/9$) half-pitch lithographic patterns were demonstrated,[30] as shown in Fig. 10a–c. Objects with a characteristic dimension of 60 nm ($\sim \lambda/6$) were also successfully imaged and recorded on a photoresist layer at a wavelength of 365 nm,[42] as indicated in Fig. 10d. Subsequently, the lithographical structures have been continually optimized to realize much smaller critical dimensions and more complex interference patterns. According to Abbe's imaging theory, the imaging process consists of many interference effects. For example, as experimentally demonstrated in 2013, by using a reflective slab, catenary plasmons could be constructed in the photoresist layer to realize a better image.[127] More recently, by

employing catenary optical fields, it was demonstrated that spatially-variant patterns could be defined by combining the EYI and photonic spin–orbit interaction.[34]

Owing to surface scattering and a relatively high material loss, the resolution of the superlens in the original experimental demonstrations was far from that theoretically predicted (as high as $\lambda/20$). In order to overcome this problem, plasmonic cavity lenses constructed by MIM triple-layer structures were proposed to enhance the photolithography qualities, including the resolution, contrast, and exposure depth. In such configurations, the top metallic film behaves as a superlens to magnify the evanescent wave and the bottom metallic film acts as a reflector to further enhance the local optical field. Fig. 11a illustrates a plasmonic lithography system based on a Ag–photoresist–Ag cavity lens.[128] When the thickness of the photoresist layer is thin enough, SPPs confined at the upper and lower Ag–photoresist interface will couple with each other, as indicated in the inset of Fig. 11b. This coupling effect causes the formation of a catenary profiled optical field distribution in the photoresist,[34] which can greatly improve the imaging contrast ratio and exposure depth. Furthermore, the coupling modes can further decrease the effective wavelength of SPPs, just as that occurs on a thin metallic film. Based on this unique property, resist patterns with 22 nm and even 16 nm half-pitch dense lines have been experimentally demonstrated,[47,128] as illustrated in Fig. 11b.

In general, single-film-based and cavity-based superlenses require the permittivity to be matched for the sake of achieving a broadband enhancement of evanescent waves. This limitation can be alleviated by replacing a single metallic slab with sub-wavelength metal–dielectric multilayers, which can be taken as a homogenous medium with macroscopic electromagnetic
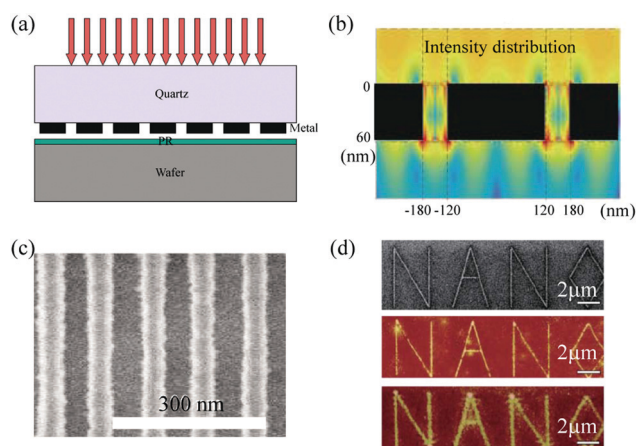

Fig. 10 (a) Schematic representation of surface plasmon lithography with a perforated silver film. (b) Simulated near field. (c) SEM image of a resist pattern. (d) Imaging lithography with a continuous silver film. Top: SEM image of an object with a 40 nm line width, middle: AFM image of topographic characterization in the resist layer with a silver superlens; bottom: AFM image of topographic characterization in the resist layer with the 35 nm thick superlens replaced by a PMMA spacer as a control experiment. (a–c) Reproduced from ref. 30 with permission. Copyright (2004) AIP Publishing. (d) Reproduced from ref. 42 with permission. Copyright (2005) AAAS.
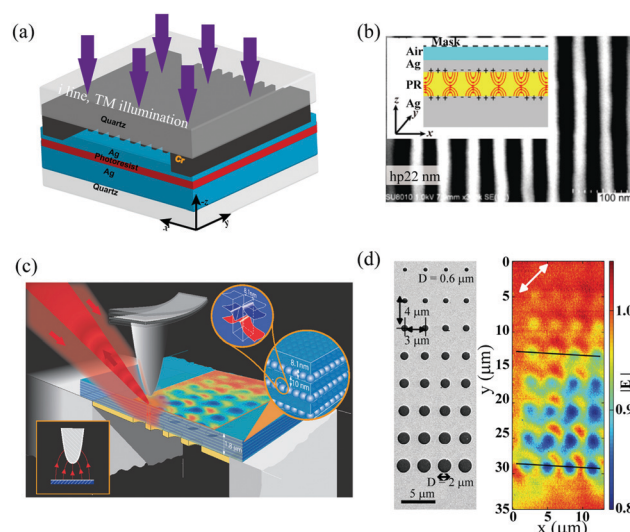

Fig. 11 (a) Scheme of the lithographic experimental setup. (b) Resist patterns of 22 nm half-pitch dense lines. Inset: SPP coupling in a plasmonic cavity lens. (c) Schematic of a superlens based on QM. (d) SEM image of the metal mask and SNOM image of the mask, taken in reflection mode, through the QM superlens. (a and b) Reproduced from ref. 128 with permission. Copyright (2015) AIP Publishing. (c and d) Reproduced from ref. 129 with permission. Copyright (2016) American Chemical Society.

properties determined by the permittivities and geometries of the composites.[130] For instance, Bak et al. proposed "quantum metamaterials" (QM), as shown in Fig. 11c.[129] In this scale, one can design new materials. For instance, a QM superlens with arbitrary elliptical iso-frequency dispersion was developed by utilizing inter-subband transitions between the confined electron states in a III–V semiconductor multiquantum-well. When the anisotropy is strong enough, the iso-frequency dispersion is quite flat even at a high spatial frequency. This means light can transmit through the QM with low loss. Consequently, it can image with a resolution down to $\sim\lambda/10$ (Fig. 11d).

When the anisotropy of the metal–dielectric further increases, such that the equivalent permitivities exhibit opposite signs in different direction, hyperbolic metamaterials are obtained, which can support the propagation of evanescent waves. Based on this unique property, Jacob et al. proposed the concept of a "hyperlens" in 2006.[93] Owing to the conservation of angular momentum, a magnified image carried by low wavevectors is ultimately formed at the outer boundary of a curved hyperlens before propagating into the far field. Then a conventional microscope can be utilized to capture the output of the hyperlens to achieve far-field super-resolution imaging. The emergence of new two-dimensional (2D) materials offers an alternative method to construct hyperlens. As indicated in Fig. 12a, hyperlens can be realized by graphene layers and h-BN layers in the ultraviolet band.[131] The simulated field distribution in Fig. 12b demonstrates that it can distinguish two sources with a distance of 100 nm.

Based on the reciprocity theorem, by simply reversing the operation direction of the magnifying superlens, a diffraction-limited pattern in a mask can be imaged to a sub-diffraction-limited one by virtue of tangential wavevector compression from the outmost layer to the innermost layer. Liu et al. reported the first experimental demonstration of a demagnifying hyperlens, which could compress the diffraction-limited features of an object (a mask) to a subwavelength pattern recorded on the photoresist using violet light.[132] The hyperlens was composed of multiple Ag/SiO$_2$ films (Fig. 12c), which permitted a sub-diffraction-limited resolution of about 55 nm line width, representing about a 1.8 demagnification factor at 365 nm light wavelength (Fig. 12d). A similar experiment carried out at 405 nm with a resolution of 170 nm line width was also reported.[133]

3.2 Microspheres and microcylinders for super-resolution imaging

Different from the high-performance and sophisticated super-resolution techniques based on superlens and hyperlens mentioned above, a dielectric lens with a spherical/cylindrical shape with an appropriate refractive index can also image objects with a precision well beyond the classical diffraction limit. The super-resolution capability of such structures stems from the extraordinary sharp focusing properties of PNJ. The PNJ is a narrow and high-intensity electromagnetic beam that propagates into the background medium from the shadow-side surface of a lossless dielectric microsphere or microcylinder with a diameter greater than the illuminating wavelength λ.

3.2.1 Photonic nanojet. Lecler et al. applied Mie theory to analyze the general three-dimensional (3D) vectorial properties of PNJ generated by a plane-wave illuminating a dielectric microsphere in free space.[134] They reported that PNJ can be generated for a wide range of microsphere diameters d from $\sim2\lambda$ to greater than 40λ. Specifically, it was found that the PNJ waist remains subwavelength for a maximum propagation distance of $\sim2\lambda$ for an optimum microsphere refractive index of 1.3. Finally, PNJs were shown to have the same electric-field polarization as the incident plane wave, but with an asymmetric beamwidth (narrower in the direction of the incident magnetic field).

Itagi and Challener[135] provided a detailed optical analysis of PNJs in two dimensions for the case of a plane-wave illuminating on an infinitely long dielectric cylinder. Their starting point was an eigenfunction solution of the Helmholtz equation, which was recast into a Debye series (an infinite sum of inward and outward radially propagating cylindrical wave modes, each of which can undergo reflection and transmission at the cylinder surface). It was shown that the first term of the Debye series is of particular importance. This term yielded a compact expression, which connects the physical and geometrical optics properties of the PNJ and permits a straightforward field analysis. Overall, PNJ characteristics were concluded to arise from a "unique combination of features" in the angular spectrum involving the phase distribution and the finite content of propagating and evanescent spatial frequencies.

3.2.2 Engineered microspheres for PNJ modification. By engineering the microsphere, the generated PNJ can be modulated in different ways. Wu et al.[136] proposed surface-engineering designs on the microsphere, e.g., concentric rings design (Fig. 13a), to enhance the sharp focusing ability and to significantly reduce the FWHM of the PNJ. Compared with the microsphere without
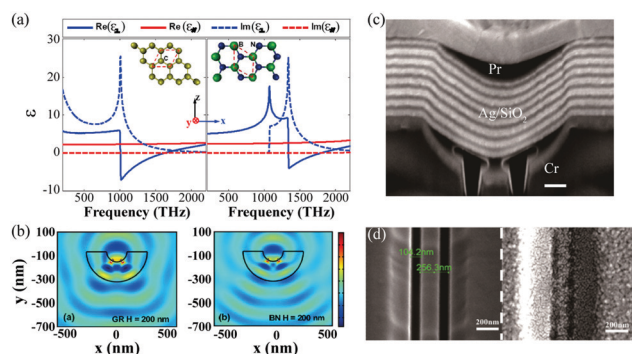

Fig. 12 (a) The anisotropy permittivity tensor for graphene (GR) and h-BN ("⊥" represents the x and z components and "∥" represents the y component). The insets show the atom unit cell of graphene and BN for dielectric constant calculation. (b) Simulated field distribution of two sources with a separation of 100 nm through the hyperlens. (c) SEM image of the cross-section of demagnifying hyperlens. (d) Left panel: Two slits mask pattern with 100 nm line width and 250 nm center-to-center distance. Right panel: Lithography result of the resist pattern. (a and b) Reproduced from ref. 131 with permission. Copyright (2012) American Chemical Society. (c and d) Reproduced from ref. 132 with permission. Copyright (2016) Royal Society of Chemistry.
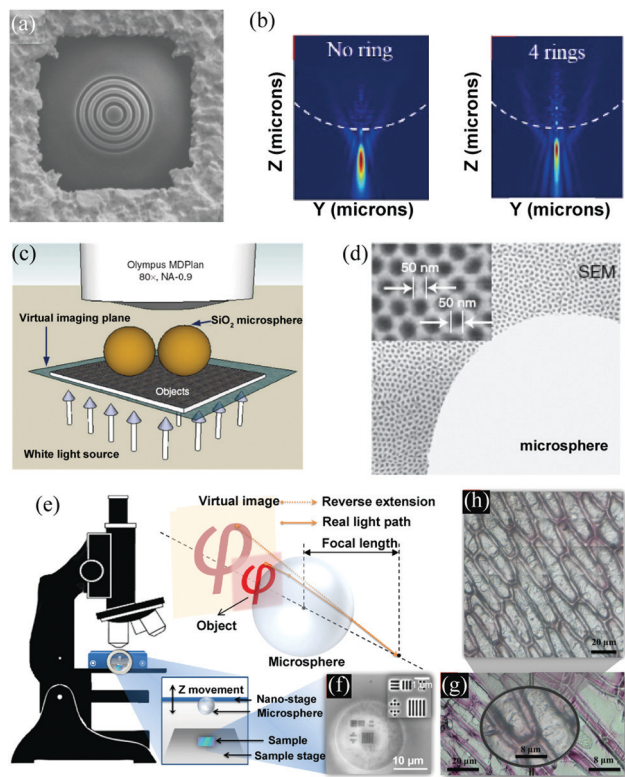
Fig. 13 (a) Engineered dielectric microsphere decorated by 4 ring grooves. (b) Simulated squeezed field through a pristine and the engineered microsphere. (c) Schematic of the transmission mode microsphere superlens with a classical optical microscope. (d) Imaging results of a gold-coated fishnet anodic aluminum oxide sample with a diameter and space of 50 nm. (e) Schematic diagram of the remote mode optical microsphere setup to generate an enlarged virtual image. (f) Optical image captured by this system (sample: semiconductor testing sample; scale bar: 10 μm; imaged by a 20 μm silica microsphere compiled to an oil-immersion optical microscope with a 100× objective lens, NA = 1.4). Inset: SEM image (scale bar: 1 μm). (g) Integrated image of onion cells and (h) a zoom view (scale bar: 20 μm). (a and b) Reproduced from ref. 136 with permission. Copyright (2015) the authors. (c and d) Reproduced from ref. 84 with permission. Copyright (2011) Nature Publishing group. (e–h) Reproduced from ref. 138 with permission. Copyright (2018) Institute of Optics and Electronics, Chinese Academy of Sciences.

such decorations, a 4-ring-decorated microsphere exhibited a more converged beam at the focal plane, as indicated in Fig. 13b. Creation of a high beam quality of a longitudinally polarized electromagnetic component of light was also demonstrated in the center-covered microsphere.[137]

3.2.3 Applications of microsphere-generated PNJ.

The PNJ possesses several key properties: (1) it is a propagating beam that can maintain a subwavelength FWHM transverse width along a path that can exceed 2λ beyond the dielectric microsphere; (2) its minimum FWHM beamwidth can be smaller than the classical diffraction limit; (3) as a consequence of light concentration, the intensity of the optical field in the focal region can be several orders of magnitude larger than the intensity of the incidence; and (4) it is a non-resonant phenomenon that can appear for a wide range of diameters d of the dielectric microsphere from $\sim 2\lambda$ to more than 40λ if the

refractive index contrast relative to the background medium is less than $2:1$. These properties combine to afford potentially important applications of PNJ for detecting and manipulating nanoscale objects, super-resolution imaging and nanolithography, and signal enhancement for substance fingerprint sensing.

Gérard et al.[139] investigated the strong electromagnetic confinement near a dielectric microsphere of 2 μm diameter, and experimentally demonstrated its effect in enhancing single-molecule fluorescence detection. When illuminated with a linearly polarized and tightly focused Gaussian beam, the microsphere increased the excitation intensity sensed by the molecule by up to a factor of 2.2, while at the same time it allowed for a collection efficiency of up to 60% by redirecting the large angle incidence toward the optical axis. By combining these two effects, the number of collected fluorescence photons could be increased by a factor of up to 5.

Fan et al.[140] also demonstrated a device integrated with solid immersed high-refractive index microspheres for high through-put and parallel detection in a microflow cytometer. In their work, glass microspheres (doped with titanium and barium) with a refractive index of 2.1 and a diameter of 75 ± 2 μm were chosen for generating a microlens array. With this device, a collimated laser beam with a wavelength of 532 nm was focused by a microball lens to excite a 2 mM resorufin fluorescent dye in the channel. The fluorescence spot size at the focal point was measured to be 5 μm in terms of FWHM and the peak intensity was located at 8 μm on top of the ball lens in the microfluidic channel. Measurements of the fluorescent dyes showed an improvement of the signal-to-noise ratio from 1.33 to 22.22 with the microball lens. Meanwhile, the 3D confinement of light by PNJ has been demonstrated and exploited to enhance the fluorescence of single molecules,[141] allowing them to out-perform conventional confocal microscopy.

The intensification of the local electromagnetic field originating from the subwavelength confinement of light around microspheres could be also exploited in Raman spectroscopy. Yi et al.[142] first observed that the Raman signal of a single-crystal Si substrate can be significantly increased when micron-sized SiO_2 spheres, acting as secondary lenses, are drop-casted over its surface. Alessandri et al.[143] tested SiO_2 microspheres as micro-lenses for detecting thin films and molecular species under different optical configurations. As a general trend, microspheres provide a systematic enhancement of Raman scattering that outperforms the results achievable by conventional Raman microspectroscopy. Such microspheres can boost the sensitivity of a Raman measurement, allowing the detection of layers of only a few nanometers. One unique advantage offered by microspheres is that they can be easily placed on any kind of coated surface by drop-casting from a solution and can then be easily removed after the measurement.

According to the Helmholtz reciprocity principle, evanescent waves are converted into propagating waves inside a microsphere. The subwavelength information of the object is thus magnified and transferred to the far-field region. Based on the configuration shown in Fig. 13c, nanoimaging of 50 nm resolution (Fig. 13d) with a magnification of up to ×8, was first demonstrated under

white light illumination.[84] Moreover, approximately 25 nm (λ/17 equivalent) resolution has been achieved by combining the microsphere lens with scanning laser confocal microscopy.[144]

Due to the non-resonant property of PNJ, microspheres can work under white light illumination, which enables multi-color imaging. Furthermore, a real *in vivo* imaging application was demonstrated to distinctly image a 75 nm adenovirus.[145] Finally, the simplicity of the microsphere imaging technique has led to a rapid demonstration of its applicability to biological imaging. Molecular and cellular characterizations along with the technique's compatibility with common fluorescent labeling have been demonstrated for a number of biological structures.[146]

Different from the previous configuration where microspheres were directly deposited on the sample surface, Chen *et al.* recently developed a remote-mode microsphere nano-imaging platform, which can scan freely and in real-time across the sample surfaces.[138] The setup is shown in Fig. 13e and f, where a microsphere is remotely integrated with the conventional objective lens. This method offers many unique advantages, such as enabling the detection to be performed in a non-invasive, dynamic, real-time, and label-free manner, thus extending the nanoscale observation power to a broad scope, with the smallest feature size down to 23 nm. The imaging results of onion cells shown in Fig. 13g and h demonstrate that a $20\times$ conventional objective lens combined with the microsphere could achieve an observation power similar to a $50\times$ objective lens.

3.3 Optical data storage

The emerging subwavelength-structured materials make it possible to tremendously increase the storage capacity of current optical memory, through the encoding of information in more physical dimensions (*e.g.*, frequency, polarization, and 3D space),[43] as shown in Fig. 14. Benefiting from the size- and shape-dependent spectral responses of LSPR, subwavelength-structured materials allow for sharp color and polarization selectivity in light–matter interactions, which makes them suitable for implementation for spectrally encoded memory. Similarly, the anisotropy of subwavelength-structured materials can be utilized for selective excitation by different polarization states of a writing beam.[147]

Besides increasing the storage dimensions, decreasing the spot size of the writing beam is also an effective method to increase the storage capacity. Once a writing beam with sub-diffraction-limited spot size is realized,[148] the maximal capacity of a single disc can be greatly improved.[149] In order to boost the writing/reading throughput, various optical parallel methods for generating multifocal arrays in single laser shots have been proposed and experimentally demonstrated. For instance, an ultrathin plasmonic microlens array based on geometric meta-surfaces, consisting of an array of plasmonic nanoantennas with the same geometry but spatially varying orientations, was utilized for parallel focusing.[150] Alternatively, diffractive optical elements are also utilized for multichannel beam generation. For example, by using accurate phase manipulations assisted by spatial light modulators, a 2-orders-of-magnitude improvement in the data rate toward gigabits/second was demonstrated.[149] By taking full advantages of the spectra, polarization, local confined volume, and parallel read-in and read-out properties, plasmonic nanostructures provide an avenue toward ultrahigh-density ($>10^{12}$ GB) optical storage with ultrahigh security and ultrahigh throughput.

Ultralong lifetime data storage is another urgent demand, which means signal contrast and data errors rates should be unchanged over a very long period of time. Zhang *et al.* proposed the concept of optical long data memory with plasmonic hybrid glass composites.[45] Through the sintering-free incorporation of nanorods into an earth-abundant hybrid glass composite, the Young's modulus is enhanced by one to two orders of magnitude, which opens up new opportunities for long-time data memory.
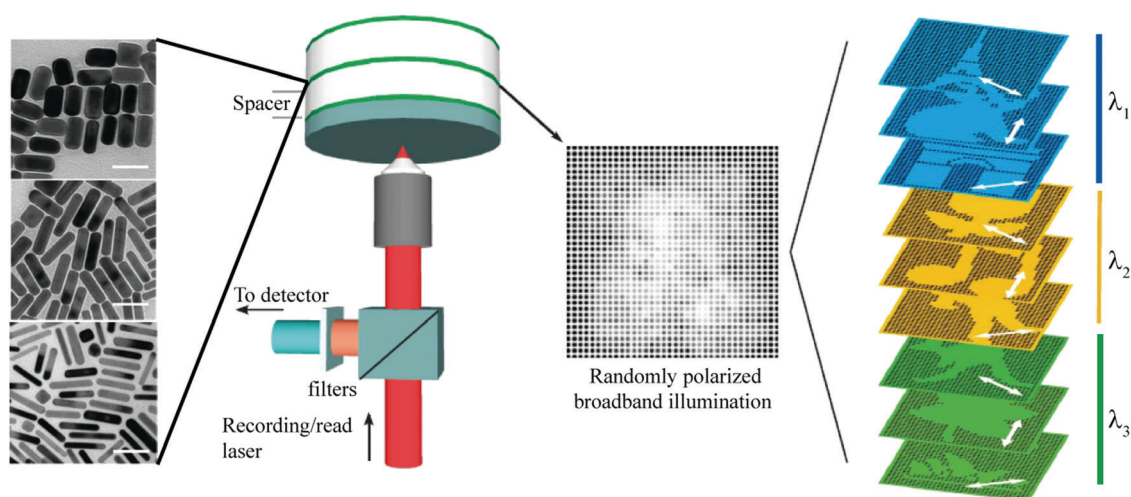

Fig. 14 Left: Transmission electron micrographs (TEM) of gold nanorods on a copper grid and a sample consisting of thin recording layers of spin-coated polyvinyl alcohol doped with gold nanorods on a glass substrate. Multiple images were patterned using different wavelengths and polarizations of the recording laser. Middle: When illuminated with unpolarized broadband illumination, a convolution of all patterns is observed on the detector. Right: When the right polarization and wavelength are chosen, the patterns can be read out individually without crosstalk. Reproduced from ref. 43 with permission. Copyright (2014) Nature Publishing group.

4. Gradient optical fields for lenses, directional radiating, and color filtering

4.1 Generalized Snell's law and tunable lenses

Although it is of fundamental importance to break the diffraction limit for high-resolution optical imaging, traditional optical engineering is often troubled with other issues, *e.g.*, the bulky size and curved profile of optical devices, which are limited by the classic refraction and reflection laws. Planar and thin devices are highly desirable for both compact and large-aperture optical systems. Along with the rapid development of nanotechnology, recently a completely new type of flat lens was proposed. By introducing a space-variant phase shift, the classic Snell's law has been generalized to the so-called generalized laws of reflection and refraction:[58,151]

$$n_1 k_0 \sin\theta_i + \nabla\Phi_r = n_1 k_0 \sin\theta_r,$$
$$n_1 k_0 \sin\theta_i + \nabla\Phi_t = n_2 k_0 \sin\theta_t,$$

(16)

where $\nabla\Phi$ is the phase gradient induced by the gradient metasurface-wave in the interface, which can be understood as a horizontal wavevector and can be dynamically tuned *via* external stimuli; n_1 and n_2 are the refractive indices of the media at the incident and transmit sides; and θ_i, θ_r, and θ_t are the angles for incident, reflected, and refracted light.

In general, subwavelength structures for phase modulation can be classified into three categories according to the physical mechanism.[55] The first kind is the metallic waveguide array made of subwavelength slits and their variations.[59,92,152] The second localized phase modulation scheme relies on the geometric phase, which is a frequency-independent phase originating from the photonic spin–orbit interaction during the process of polarization conversion.[68,69,153–156] The third approach for phase modulation is based on the circuit resonance in complex metallic or dielectric surface structures.[151,157]

Using a collection of slits with variant widths to form a special phase gradient induced by surface plasmon retardation, the wavefront can be arbitrarily manipulated, as demonstrated by a series of work, including abnormal deflection (Fig. 15a and b),[59] sub-diffraction-limited focusing (Fig. 15c),[92] and sub-wavelength imaging.[158] As shown in Fig. 15d, a p-polarized wave with a wavelength of 637 nm was focused at a focal length of 5.3 μm with a FWHM of 0.88 μm through a plasmonic lens.[152] To realize polarization-independent 2D focusing, these nanoslits were replaced by circular or square plasmonic holes with a variable radius to generate polarization-independent phase modulation.[159,160] Furthermore, compared with the slits array with modulated widths, catenary-inspired nanoapertures have more freedoms in deep subwavelength phase manipulation, which is indispensable for wide-angle focusing and imaging using a single metasurface.[161]

The nanoslits-based plasmonic lens was tunable by filling the nanoslits with Kerr nonlinear media. As illustrated in Fig. 16a–c,[162] each slit transmits light with a specific phase retardation controlled by the intensity of incident light, owing to the nonlinear response. This novel lens could actively control the deflection angle.
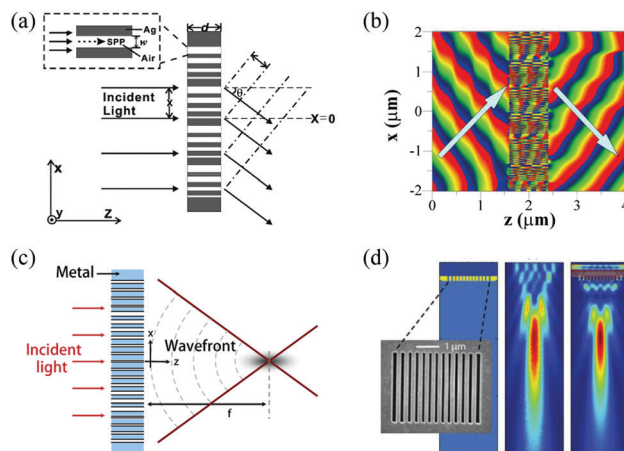

Fig. 15 (a) Schematic of a metallic beam deflector. The inset depicts the excitation and propagation of SPPs in the nanoslit when the incident light impinges on the metal surface. (b) Calculated phase distribution of the electric field. Incident and deflection angles are designed as 30° and −30°, respectively. (c) Schematic of the nanoslits lens for beam focusing. (d) Planar lens based on a nanoscale slit array in a metallic film and the simulated as well as measured focusing pattern. (a and b) Reproduced from ref. 59 with permission. Copyright (2008) the authors. (c) Reproduced from ref. 92 with permission. Copyright (2005) the authors. (d) Reproduced from ref. 152 with permission. Copyright (2009) American Chemical Society.

By filling a phase-change material, for example, Ge$_2$Sb$_2$Te$_5$ (GST-225) into the nanoslits-based plasmonic lens, active tuning could be obtained (Fig. 16d and e). When the crystallization level
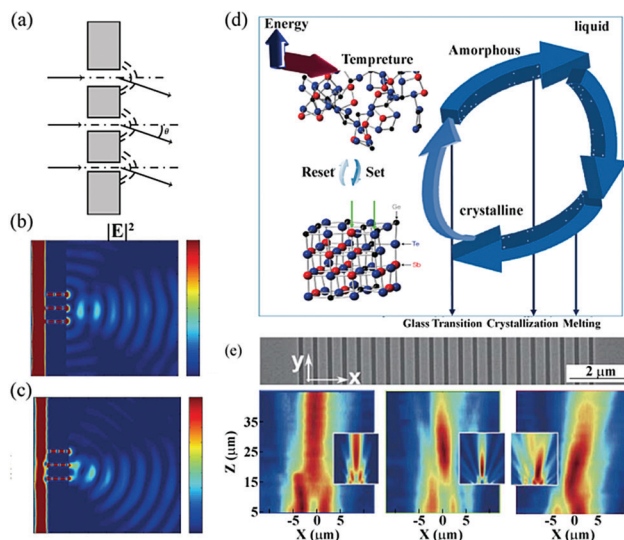

Fig. 16 (a) Schematic view of the three-slit structure filled by a nonlinear Kerr material. (b and c) FDTD simulations of electric-field intensity distribution at different incident amplitudes: (b) 1×10^8 V m^{-1} and (c) 2×10^8 V m^{-1}. (d) Schematic illustration of the phase transition of GST between amorphous and crystalline phases. (e) SEM image of the fabricated planar lens before sputtering GST (upper panel) and the focusing pattern measured in the *xz*-plane by confocal scanning optical microscopy for different statuses of GST (lower panel). (a–c) Reproduced from ref. 162 with permission. Copyright (2007) the authors. (d) Reproduced from ref. 164 with permission. Copyright (2017) MDPI. (e) Reproduced from ref. 163 with permission. Copyright (2015) the authors.

of GST was varied from 0% to 90%, a transmitted electromagnetic phase modulation as large as 0.56π was realized at the working wavelength of 1.55 μm.[163] Consequently, different phase fronts could be constructed by assigning the designed GST crystallization levels to the corresponding slits.

4.2 Directional radiation with nano-emitters

Directing the fluorescence from nanoscale emitters, such as single molecules and single quantum dots (QDs), plays a key role in quantum optics and fluorophore analysis in biotechnology, medical diagnostics, and cell imaging. However, efficient optical excitation and the detection of such nano-emitters involve large solid angles because their interaction with freely-propagating light is nearly omnidirectional. To overcome this limit, one approach developed during the past decades takes advantages of the modes of coupling between the evanescent waves and the propagating waves using metallic nanostructured surfaces.[165,166] It is now known that fluorophores at the excited state display interactions with surface plasmons, which can increase the radiative decay rate, modify the spatial distribution of the emission, and realize directional emission.

Recently, a multilayer metal–dielectric structure was proposed, which allows excitation with light perpendicular to the plane and provides emission within a narrow angular distribution normal to the plane. The intrinsic mechanism is the excitation of the optical Tamm states, or so-called Tamm plasmons (TPs), which trap the electromagnetic modes with highly confined optical fields between the metal film and the underlying Bragg grating. Tamm states can exist with zero in-plane wavevector components and can be created without the use of a coupling prism. So the fluorophores on top of the metal film can interact with the Tamm state under the metal film to display Tamm state-coupled emission TSCE.[167]

Fig. 17a shows the structure consisting of a thin silver film on top of a multilayer dielectric Bragg grating.[168] A bright disk on the center of back focal plane (BFP) image presented in Fig. 17b shows that the TPCE at 560 nm propagates normal to the surface of the structure. The TSCE angle is highly sensitive to the wavelength (Fig. 17c), which suggests the use of Tamm structures to provide both directional emission and wavelength dispersion. Another method to directionally radiate light by coupling the evanescent waves to the propagating waves is by using a subwavelength aperture decorated by periodic grooves, a so-called bull's eye structure.[169–172] In 2002, Lezec *et al.* experimentally observed that the bull's eye structure can break the traditional diffraction limit and achieve highly directional energy transfer with ultrahigh transmission, called the beaming effect.[170] Based on this effect, the enhancement factor of the fluorescence count rate per molecule was increased by up to 120-fold, simultaneously with a directional emission of the fluorescence into a narrow angular cone in the direction normal to the sample plane,[169] as indicated in Fig. 17d and e.

Directional radiation of nano-emitters can also be realized with nanoantennas, in analogy to the traditional concept of a directional antenna in radio and microwave. So far, monopole/dipole[173] and Yagi–Uda antennas[174,175] have been developed for
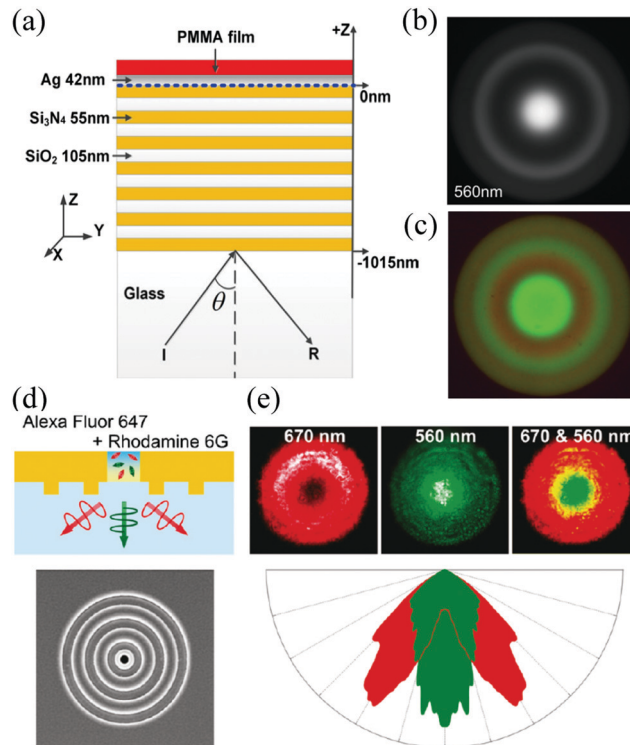

Fig. 17 (a) Schematic of the Tamm structure and layer dimensions. $Z = 0$ is at the metal/Bragg reflector interface. (b) BFP image of a spot on the Tamm samples. The Rhodamine 6G molecules were dissolved in the water solution. A bandpass filter with a center wavelength of 560 nm was used. (c) Color BFP image taken from the same spot as (b). The different colors represent different fluorescence wavelengths that emit into the corresponding angles. (d) Upper panel: Sketch of the experiment; the central aperture is filled with a mixed solution of Alexa Fluor 647 and Rhodamine 6G. Lower panel: SEM image of corrugated apertures with two grooves. (e) Upper panel: Radiation patterns in the back focal plane of the objective for emission centered at 670 nm, 560 nm, and a combination of the two color images. Lower panel: Fluorescence radiation patterns. (a–c) Reproduced from ref. 168 with permission. Copyright (2014) Wiley-VCH Verlag. (d and e) Reproduced from ref. 169 with permission. Copyright (2011) American Chemical Society.

realizing the full potential of the directional control of fluorescence radiation from molecules ions, and QDs. Fig. 18a shows a Yagi–Uda nanoantenna consisting of an actively driven feed element surrounded by a set of parasitic elements acting as reflectors and directors. The radiation pattern shows a single lobe, demonstrating the unidirectional emission of a QD due to coupling to the optical antenna, as shown in the corresponding emission patterns in Fig. 18b. The front-to-back ratio, defined as the intensity ratio between the point with maximum emitted power and the point diametrically opposite in the radiation pattern, is 6.0 dB (or alternatively, an intensity ratio of 4). The experimental angular radiation pattern, calculated from the Fourier-plane image, agrees well with the theoretical prediction (Fig. 18c).

4.3 Miniature and tunable color filters

Structural color, originating from the complex interaction between light and nanostructures, widely exists in the natural
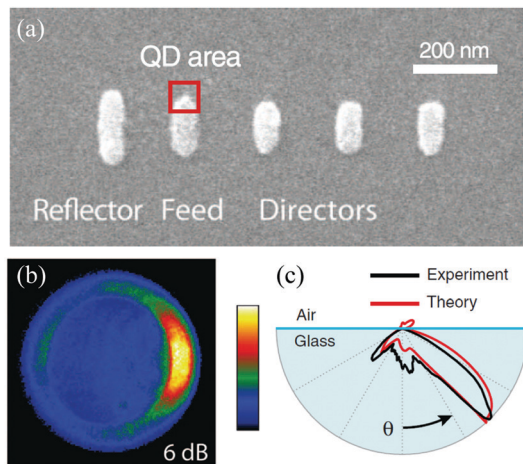
Fig. 18 (a) SEM image of a fabricated 5-element Yagi–Uda antenna. A QD is attached to one end of the feed element inside the marked area. (b) Radiation pattern (intensity distribution at the back focal plane of the objective) of the Yagi–Uda antenna. A 830 nm long-pass filter was used. (c) Angular radiation pattern in the polar angle (θ) for the Yagi–Uda antenna (black), which is in good agreement with the theoretical prediction (red). Reproduced from ref. 175 with permission. Copyright (2010) AAAS.

Fig. 19 (a) Holes in a dimple array generating the letters '$h\nu$' in transmission. In this case, the periods of the hole arrays were chosen to be 550 and 450 nm, respectively, to achieve the red and green colors. (b) Schematic diagram of the plasmonic nanoresonators. (c) Simulated transmission spectra for the RGB filters. (d) Simulated electric field intensities in the cross-section of the time-average magnetic field intensity and electric displacement distribution (red arrow) inside the MIM stack at a wavelength of 650 nm with 360 nm stack period. (e) Optical microscopy images of seven plasmonic color filters illuminated by white light. Scale bar: 10 μm. (a) Reproduced from ref. 178 with permission. Copyright (2007) Nature Publishing group. (b–e) Reproduced from ref. 37 with permission. Copyright (2011) Nature Publishing group.

world. Recently, structural color has been extensively studied with planar artificial structures.[176,177]

EOT through a metallic hole array has attracted tremendous attention due to its unique properties and potential applications in many fields, ranging from optical elements to sensors for chemistry and biology, since it was first observed in 1998.[7] The hole array structure can act like a tunable filter by taking advantage of the surface plasmon coupling between the holes nearby. Different colors can be obtained due to the wavelength selectivity of the array transmission. As shown in Fig. 19a, the letters "h" and "ν" with different colors were obtained when the structure was illuminated with white light.[73,178] Wavelength selective transmission can also be found in structures with a slit or hole surrounded by metallic grooves,[179] and in plasmonic nanoresonators with subwavelength MIM stack arrays.[37] Taking advantage of the near-linear dispersion of the antisymmetric mode in a MIM waveguide, the MIM resonator color filter is capable of filtering white light into individual colors across the entire visible spectrum (Fig. 19b–e).[37] The most significant advantage of a MIM resonator color filter over other plasmonic nanostructures is its high efficiency and ultrahigh spatial resolution (closed to the diffraction limit) due to the highly localized SPP fields.

Structural colors were also found in the metasurfaces with wavelength selective reflection or absorption.[180–188] Reflective imaging was realized by a hybridized nanodisk and nanohole arrays at a resolution of ~100 000 dots per inch, as shown in Fig. 20a–d.[180] Fig. 20e shows the structure combining the holes array and reflective ground,[181] which was originally studied in a perfect absorber.[189] This hybrid structure could modulate the localized fields distributions (Fig. 20f) and the reflective spectra, and colorful imaging could be obtained with proper design of the geometry, as shown in Fig. 20g.[181] High-purity structural
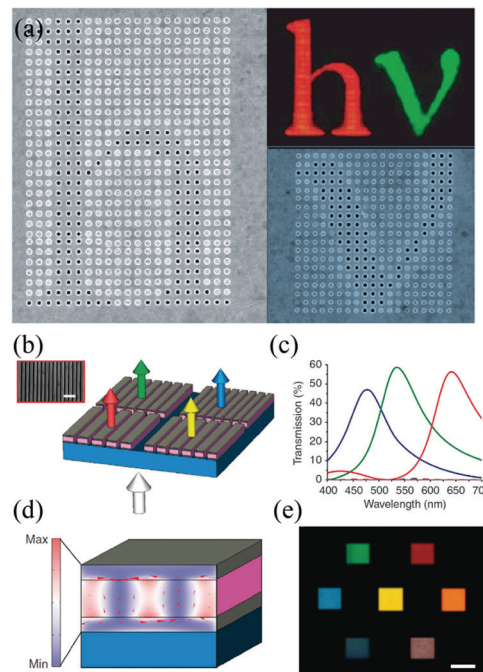
colors were achieved with a plasmonic shallow grating metamirror. Different from current designs, the metamirror reflected a circularly polarized (CP) light to its co-polarized state at specific wavelengths, and a FWHM of ~16 nm reflective spectra with high efficiency (~75%) was experimentally demonstrated.

There is a growing interest in dynamic color displays, which could permit real-time color manipulation of the images.[190–194] Mechanical modulation is a typical method to dynamically tune the performance of metamaterials or metasurfaces. A tensile substrate, e.g., polydimethylsiloxane, was introduced into conventional plasmonic structures as the substrate to actively tune the structural colors.[191] This system enabled the tuning of the resulting colors throughout the visible spectrum by varying the mechanical force. Chemical methods have also been used for color tuning by combining with propagating surface plasmon resonance (PSPR) and LSPR.

Fig. 21a illustrates a dynamic plasmonic display technique based on polyaniline (PANI) metasurfaces.[194] The chemical structures of PANI in the oxidized and reduced form are shown in Fig. 21c. First, high-contrast electrochromic switching was realized by enhancing the interaction of light with the metallic nanoslits coated of an electrochromic polymer on the slit sidewalls, as shown in Fig. 21b. By controlling the pitch of the nanoslit
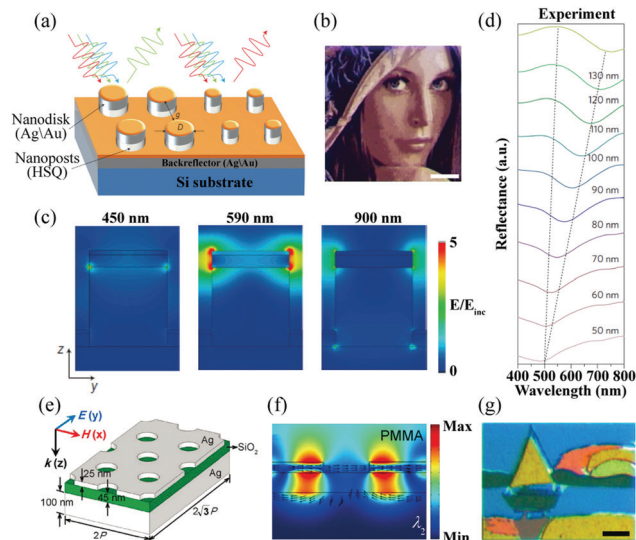
Fig. 20 (a) Schematic of the nanodisks and the interaction of white light with two closely spaced pixels. (b) Optical micrographs of the Lena image. (c) Electric field enhancement plots (top) and time-averaged power flow vector plots (bottom) for a single repeat structure with $D = 90$ nm at wavelengths of 450 nm (i), 590 nm (ii), and 900 nm (iii). (d) Experimental reflection spectra of nanodisks with varying sizes of diameter D, with a gap between the nanodisks of $g = 140$ nm. (e) Schematic of unit cells for triangular-lattice circular hole arrays fabricated on a silver−silica−silver three-layer structure. (f) Cross-section of the time-averaged magnetic field intensity (colored contours) and electric displacement (black arrows) distributions for the uncoated metasurface at the wavelength $\lambda_2 \sim$ 570 nm. (g) Optical microscopy image of the PMMA-coated plasmonic painting. Scale bars: 10 µm. (a–d) Reproduced from ref. 180 with permission. Copyright (2012) Nature Publishing group. (e−g) Reproduced from ref. 181 with permission. Copyright (2015) the authors.
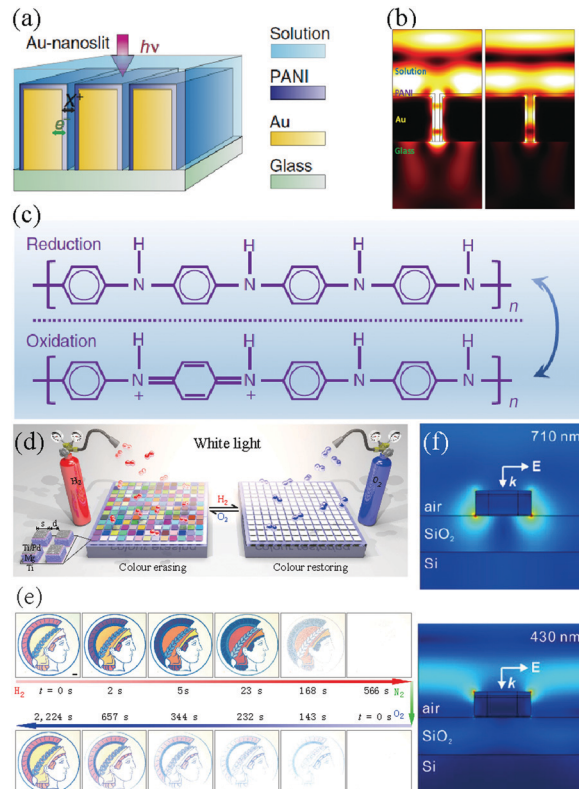

Fig. 21 (a) Schematic diagram of a plasmonic electrochromic electrode incorporating an Al-nanoslit array. (b) FDTD simulated electric field intensities in Au-nanoslit electrochromic devices with a PANI film in reduced form (left side) and oxidized form (right side). The operation wavelength was at 632.8 nm and the PANI film thickness was 15 nm. (c) Chemical structures of electrochromic polymers PANI in the reduced and oxidized form. (d) Schematic of the plasmonic metasurface composed of hydrogen-responsive Mg NPs interacting with incident white light. (e) Optical micrographs of the Minerva logo during hydrogenation and dehydrogenation for color erasing and restoring, respectively. Scale bar: 20 µm. (f) Simulated electric field distributions at 710 nm and 430 nm. (a–c) Reproduced from ref. 194 with permission. Copyright (2016) the authors. (d–f) Reproduced from ref. 192 with permission. Copyright (2017) the authors.

arrays, it was possible to achieve a full-color response with high contrast. Dynamic color tuning has also been accomplished by using catalytic magnesium metasurfaces.[192] The colors were tuned, erased, or restored during the process of the hydrogenation and dehydrogenation of Mg NPs, as shown in Fig. 21d–f.

5. Enhanced optical fields for biochemical sensing

Chemical identification and probing by optical means to obtain higher sensitivity is a challenging task and usually requires a large enhancement of the local fields acting on the molecules. As indicated in Fig. 22, plasmonic localized-field enhancement, one of the most effective approaches to improve light–matter interaction, has been widely utilized for detecting or sensing through enhanced radiation, scattering, and absorption, which are discussed in the following sections.

5.1 Surface plasmon resonance sensing

It is highly desired to develop biochemical sensors with high sensitivity, low-cost, and miniature size.[196,197] Both PSPR[198] and LSPR[199] can be used in surface-based optical sensing. Compared with PSPR, LSPR sensors offer the advantages of simple optical

extinction measurement and of being temperature-insensitive. Moreover, advances in both synthetic and lithographic fabrication techniques allow researchers to tune the LSPR wavelength throughout the EM spectrum, by varying the shape, size, and material of the NPs that support the surface plasmons.[200–203] It offers additional flexibility in designing LSPR sensors. However, LSPR-based sensors are known to provide at least an order of magnitude lower sensing response to refractive index change as well as a 10 times smaller probe depth compared with sensors based on PSPR.[204]

In order to improve the sensitivity, plasmonic metamaterials consisting of an assembly of Au nanorods are utilized to mimic the dispersion of SPPs confined on a metal film.[204] When the distance between the nanorods is smaller than the wavelength, the plasmonic metamaterials support a guided mode that has resonant excitation conditions similar to the SPP mode of a smooth metal film. This metamaterial provides an enhanced sensitivity to refractive index variations of the medium between the rods (more than 30 000 nm per RIU).
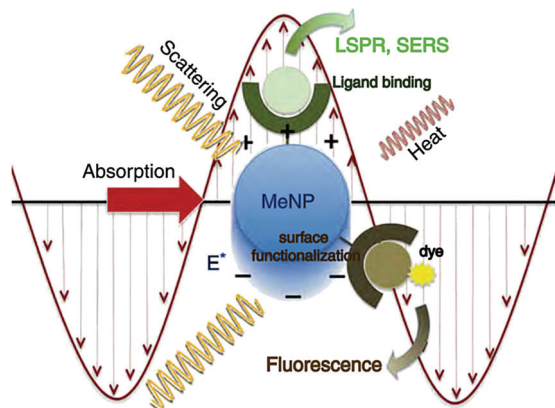
Fig. 22 Schematic representation of the induced surface charge oscilla-tions of a metal nanoparticle by an external light field and possible spectro-scopic responses for sensitive biomolecular detection. Reproduced from ref. 195 with permission. Copyright (2012) Cambridge University Press.
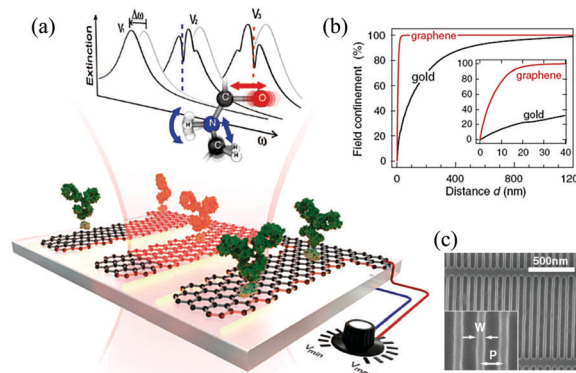

Fig. 23 (a) Conceptual view of a graphene biosensor. An infrared beam excites a plasmonic resonance across the graphene nanoribbons. The electromagnetic field is concentrated at the ribbon edge, enhancing light interaction with the protein molecules adsorbed on graphene. Protein sensing is achieved by detecting a plasmon resonance spectral shift accompanied by narrow dips corresponding to the molecular vibration bands of the protein. The plasmonic resonance is electrostatically tuned to sweep continuously over the protein vibrational bands. (b) Percentage of space-integrated near-field intensity confined within a volume extending a distance d outside the nanoantenna. Inset shows a zoom-in for d between 0 and 40 nm. (c) SEM image of a graphene nanoribbon array (width W = 30 nm, period P = 80 nm). Vertical nanoribbons are electrically interconnected by horizontal strips to maintain the graphene surface at uniform potential. Reproduced from ref. 208 with permission. Copyright (2015) AAAS.

Although the sensitivity is an important indicator to assess an SPP sensor, the detection limit is also strongly restricted by the spectral width of the resonance. Therefore, the figure of merit (FOM), defined as the sensitivity divided by the resonance line width, is preferred to evaluate the performance of a sensor. Reducing the line width of an SPP mode is an effective way to improve the FOM and hence the sensitivity of the plasmonic mode. Many efforts have been devoted to achieving a narrow line width by mode coupling. Cetin et al.[205] experimentally demonstrated a Fano resonant asymmetric ring/disk system fabricated on a conducting substrate. On the one hand, such a platform enables a high refractive index sensitivity as large as 648 nm per RIU; while on the other hand, this cavity system supports Fano-type resonances that can exhibit spectrally sharp features with a line width as narrow as 9 nm.

For chiral nanostructures, circular dichroism (CD) offers an alternative to extinction-based sensing techniques. Their polarization-dependent spectra provide additional and sharper spectral features than that of achiral particles. These character-istics make chiral plasmonic nanohelices possess remarkable refractive index sensitivities (1091 nm per RIU at λ = 921 nm) and FOM (42 800 per RIU).[206] An alternative strategy to improve the sensitivity is to employ the nonlinear effect. Mesch et al. introduced nonlinear plasmonic sensing to enhance the sensi-tivity of LSPR sensors.[207] A distinct increase of the sensor signal was observed due to the strong dependence on the local electric fields of the nanoantennas in the process of the third harmonic generation for pure water and an 8.5 M aqueous ethanol solution, which made it possible to detect a refractive index change as small as 10^{-3}.

IR absorption spectroscopy is a powerful technique that provides exquisite biochemical information in a nondestructive label-free fashion by accessing these vibrational fingerprints. Nevertheless, vibrational absorption signals are prohibitively weak because of the large mismatch between mid-IR wave-lengths (2 to 6 μm) and biomolecular dimensions (<10 nm). In order to overcome this problem, Rodrigo et al.[208] demon-strated a high-sensitivity tunable plasmonic biosensor for the

chemically specific label-free detection of protein monolayers. As illustrated in Fig. 23, the SPR of nanostructured graphene could be dynamically tuned to selectively probe the protein at different frequencies. Additionally, the extreme spatial light confinement in graphene—up to two orders of magnitude higher than that in metals—produces an unprecedentedly high overlap with nanometric biomolecules, enabling superior sensitivity in the detection of their refractive index and vibra-tional fingerprints. The combination of tunable spectral selec-tivity and the enhanced sensitivity of graphene opens exciting prospects for biosensing.

For medical diagnosis, high-throughput sensing technolo-gies that can enable the simultaneous detection of a wide range of proteins is highly desired. Cetin et al.[209] demonstrated a handheld on-chip biosensing technology that employs plasmonic microarrays coupled with a lens-free computational imaging system toward the multiplexed and high-throughput screening of biomolecular interactions for point-of-care applications and resource-limited settings.

In the last few decades, a lot of efforts have also been made toward the development of gas sensors so as to protect the environment and workplace from harmful and toxic gases. Compared with traditional semiconductor-based gas sensors, LSPR-based optical gas sensors have several advantages includ-ing simplicity, high reliability, room temperature operation, and fast response. By placing a single palladium NP near the tip region of a gold nanoantenna and detecting the optical properties changes of the system upon hydrogen exposure by dark-field microscopy, Liu et al. demonstrated antenna-enhanced hydrogen sensing at the single-particle level (Fig. 24).[210]
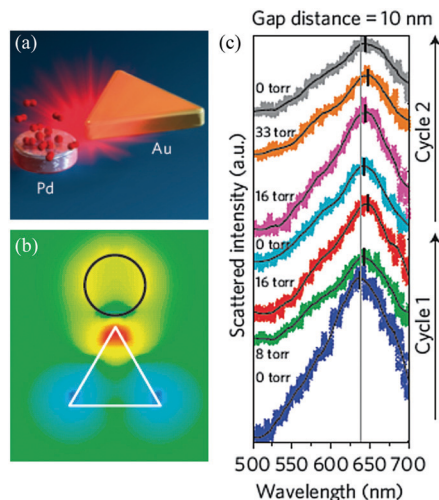
Fig. 24 (a) Schematic representation of antenna-enhanced single-particle hydrogen sensing. (b) Electromagnetic finite-difference time-domain simulation of the local electric fields. (c) Optical-scattering measurements of a single palladium–gold triangle antenna upon hydrogen exposure when the separation between the gold antenna and the palladium particle d = 10 nm. Reproduced from ref. 210 with permission. Copyright (2011) Nature Publishing group.

Recently, some novel 2D materials, such as graphene, molybdenum disulfide (MoS_2), and black phosphorous (BP), have also been utilized for LSPR-based gaseous sensors. With optimized sensing parameters, a bilayer of BP has shown a 35% enhancement in sensitivity compared with a conventional gaseous sensor based on the LSPR of metal, which could be further enhanced to 73% by adding a monolayer of MoS_2.[211]

5.2 Surface-enhanced Raman scattering

Among all molecular spectroscopies, Raman spectroscopy is the one most commonly used to characterize molecular vibrational energy levels and to identify molecular groups.[196,212–215] However, due to the small molecular cross-sections for the Raman process, it is challenging to detect vibrational signals unambiguously for minuscule amounts of molecules. To overcome the limitation of the small cross-sections, plasmonic metal nanostructures have been employed to realize SERS. The enhancement factor for SERS can be expressed as:[75,216]

$$EF_{SERS}(\omega_v) = \frac{|E_{out}(\omega)^2||E_{out}(\omega - \omega_v)^2|}{E_0^4}, \quad (17)$$

where ω_v is the Stokes shift caused by the vibrational frequency of the molecule. For a spherical particle:

$$E_{out} = E_0\hat{z} - \left[\frac{\varepsilon_{in} - \varepsilon_{out}}{\varepsilon_{in} + 2\varepsilon_{out}}\right]a^3 E_0\left[\frac{\hat{z}}{r^3} - \frac{3z}{r^5}(x\hat{x} + y\hat{y} + z\hat{z})\right]. \quad (18)$$

where ε_{in} is the dielectric constant of the metal NP, ε_{out} is the dielectric constant of the external environment, and a is the radius of the sphere. If the Stokes shift is small, the enhancement factor for SERS is nearly proportional to the fourth power of electric-field enhancement.

The investigation history of plasmon-enhanced Raman scattering can be dated back to 1974, when Fleischmann *et al.* first reported the dramatic enhancement of the Raman scattering cross-section of molecules on rough metal surfaces,[217] which was then effectively confirmed in 1977 by Van Duyne and co-authors.[196] Two decades later, this technique, known as SERS, has enabled the detection of single molecules.[213,218] Enhancement factors in the range of 10^{10}–10^{14} have been reported to occur at 'hot spots'—regions of high electromagnetic fields associated with localized plasmonic resonances.[12,219]

Generally, two mechanisms account for the enhancement of SERS signals, including electromagnetic enhancement and chemical enhancement.[15] The tremendous electromagnetic field, around two orders of magnitude larger than that of incidence, is highly localized in narrow regions. These hot-spots play a pivotal role in determining the SERS signals' intensity.[220,221] Generally, rationally engineered hot-spots can significantly contribute to the increase in SERS signals, with a theoretical enhancement factor of 10^{14}–10^{15} based on the electromagnetic enhancement.

SERS substrates initially were metal colloids, such as Au or Ag, freely suspended in aqueous solutions.[213,218,222,223] The analyte molecules in suspensions can be adsorbed on the NPs for signal enhancement. This SERS detection approach is mostly used in current applications due to their stability and ease of use. As the localized near field of a single spherical NP is relatively weak, two main routes have been widely applied to enhance the metal colloids-based SERS substrates. The first approach relies on the judicious synthesis of NPs with sharp tips or corners, such as nanorods, triangle, star, cube, and dendrite-shaped NPs, which can generate intensive localized electric fields.[224] The other strategy is based on the aggregation of NPs, rendering the production of a high density of hot-spots.[225] However, the SERS detection by using NPs in suspensions faces challenges because of aggregation of the NPs, which leads to a poor reproducibility of the systems.

In order to overcome the aggregation of NPs in solution and then to achieve substrate reproducibility, Tian *et al.* proposed shell-isolated NPs-enhanced Raman spectroscopy (SHINERS) in 2010 (Fig. 25),[226] which presents a couple of advantages.[25,227] First, the shell protection prevents the NPs from aggregation, oxidation, and the degradation of plasmonic properties. Second, the features of core–shell NPs can be flexibly tuned by tailoring not only the size, shape, and component of the cores, but also the thickness and components of the shells. Third, the SERS measurement by bare plasmonic NPs usually suffers from photobleaching, distortion of the vibrational information, and even metal-catalyzed site reactions, but the noble metal NPs with shells' coating can be spread over the objective surfaces adsorbed with analytes without chemical interaction with the probed molecules. Fourth, in practical bioapplications, one of the important issues lies in biocompatibility and here, the core–shell NPs are able to improve the biocompatibility. Until now, plenty of materials have been applied as shells, such as SiO_2, TiO_2, Al_2O_3, Fe_3O_4, graphene, and polymers. Because of the rapid decay of near fields, the thickness of the shell should be carefully controlled in case of significant loss of SERS performance.[25]
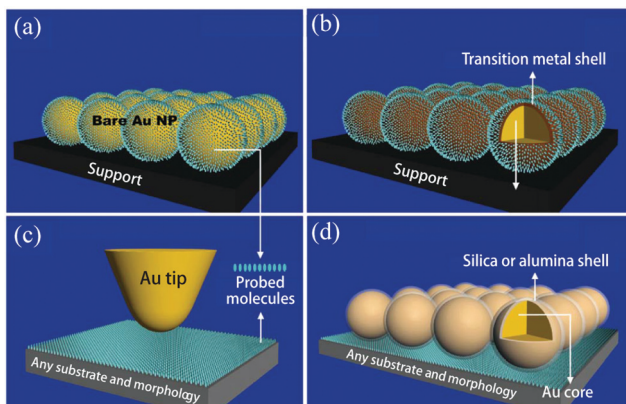
Fig. 25 Different working principles of SERS modes. Schematic of the contact mode. (a) Bare Au NPs: contact mode. (b) Au core–transition metal shell NPs adsorbed by probed molecules: contact mode. (c) Tip-enhanced Raman spectroscopy: noncontact mode. (d) SHINERS: shell mode. Reproduced from ref. 226 with permission. Copyright (2010) Nature Publishing group.

Overall, the strategy of plasmonic core–shell NPs improves the reproducibility and reliability of the quantitative detection of SERS signals.

To achieve the higher reproducibility and uniformity of SERS signals, scientists tend to develop SERS systems on solid materials. Due to the rapid advances made in nanofabrication technologies, especially the state-of-art lithographic methods, SERS-active substrates with nanogaps of one to several nanometers can be made,[221] which are usually supported by solid substrates, such as Si, quartz, or metal plates.[228]

Recently, Ag-nanorod bundle arrays (Fig. 26a and b) were fabricated as SERS substrates,[229] and have shown a SERS

enhancement as high as 10^8. Simulation results revealed that "hot spots" were generated due to strong EM field coupling among the neighboring Ag-nanorods with narrow $\sim$2 nm gaps at the top end (Fig. 26c and d). The SERS substrates with good uniformity (Fig. 26e) and reproducibility could be used to simultaneously detect multiple trace organic pollutants in water (Fig. 26f).

Due to the superior features, such as high sensitivity, ease of operation, label-free, and fingerprint detection of diverse analytes, SERS has been widely applied in a variety of fields, including environmental monitoring, biomedical diagnostics, and homeland security.[230] In terms of environmental monitoring, SERS has been used in the detection of pesticides, explosives, and heavy metal ions as well as volatile organic compounds, *etc.* Since the initial research on the SERS detection of pesticides, such as dithiocarbamate and cyromazine, on gold and silver surfaces, much attention has been drawn to the detection of pesticide pollutants using SERS over the past few decades.[231]

In order to achieve the promising goal of the *in situ* detection of pesticides, the SHINERS method discussed in the previous section using an ultrathin silica or alumina shell-coated gold NPs has been adopted.[25] Besides, the detection of explosives has thus attracted much research attention. To date, many explosives have been successfully detected by the SERS technique, including trinitrotoluene, dinitrotoluene, dinitroanisole, trinitrobenzene, and their mixtures.[232] As most explosives have relatively low Raman cross-sections, the effective detection of explosives require highly sensitive SERS-active substrates with the capability of detecting extremely low concentrations.

Another significant application of the SERS technique is biomedical diagnostics, which usually consists of label-free
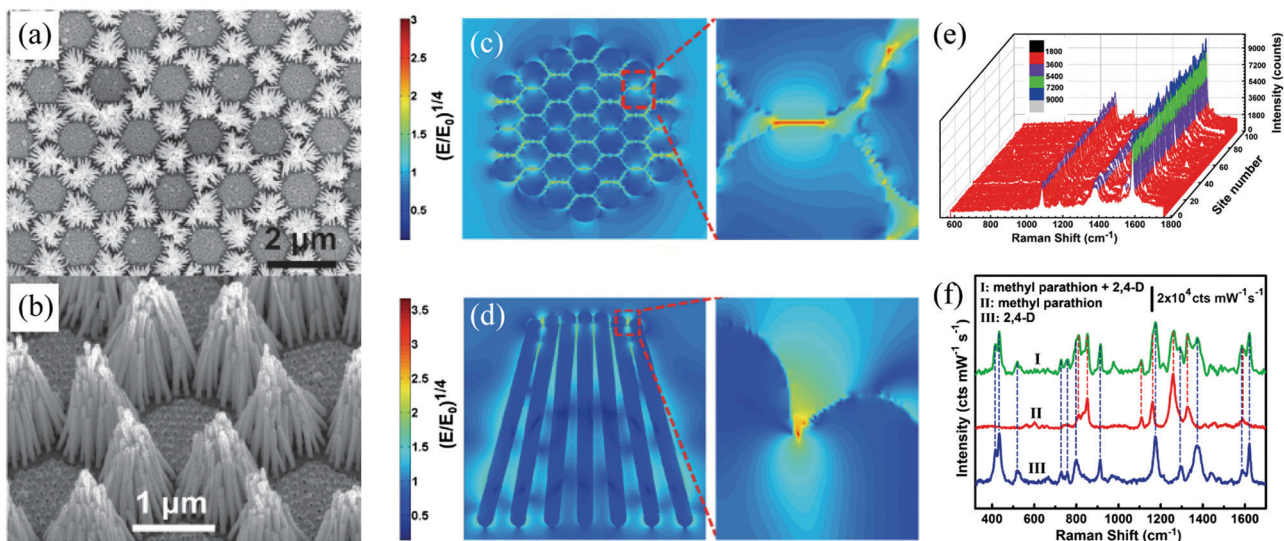

Fig. 26 SEM images of the as-prepared Ag-nanorod bundle arrays: (a) top view and (b) side view. (c and d) FDTD-simulated EM-field distribution around a bundle of 37 Ag-nanorods under normal incidence with a wavelength of 633 nm. The peak EM field $(E/E_0)^2$ was found to be 3×10^4. (e) 100 randomly selected SERS spectra from the SERS mapping. (f) SERS detection of multiple trace organic pollutants using the as-prepared Ag-nanorod bundle arrays. (curve I) SERS spectrum of the mixture of 0.3×10^{-6} M methyl parathion and 2×10^{-6} M 2,4-D, and SERS spectra of pure aqueous solutions of (curve II) 0.3×10^{-6} M methyl parathion and (curve III) 2×10^{-6} M 2,4-D, respectively. Reproduced from ref. 229 with permission. Copyright (2016) Wiley-VCH Verlag.

detection and multiplexed tagging diagnostics.[233] In the past decade, scientists have attempted to achieve profile spectral signatures of biomolecules, such as proteins, glucose, nucleic acids, and cancer cells, with a sensitivity down to the single molecule level. Xu *et al.* overcome protein denaturation to achieve reproducible SERS signals by introducing an iodide layer, which could prevent the changes in protein structures, but the reliability of this method needs to be examined and improved.[234] As for nucleic acid detection, a method was developed to produce reliable SERS spectra of DNA sequences *via* decorating citrate-stabilized silver NPs with positively charged spermine molecules, thus contributing to the adhesion of the negatively charged DNA and to stable aggregation kinetics.[235] This technique can obtain information about the content of the nucleotide bases as well as the spectral characteristics from the methylated base pairs.

5.3 Surface-enhanced fluorescence

Currently, single-molecule spectroscopy mostly relies on fluorescence, as it provides for fast, high-contrast, and low background detection of single molecules. The key requirement of this technique is that the molecules under investigation must have a sufficiently high photon emission rate.[203,236,237] However, a large fraction of strongly absorbing molecules, including many biologically relevant proteins and metal complexes, fluoresce weakly. Plasmonic particles are ideal SEF substrates. When the localized surface plasmon is resonantly matched with the frequency of the molecular vibration, a tremendous enhancement achieves. The strongly confined fields near the metallic nanostructures can profoundly alter the light-emission properties of nearby optical emitters or molecules by: (1) increasing the optical excitation rates; (2) modifying the radiative and nonradiative decay rates; and (3) altering the emission directionality.[238]

Fluorescence enhancement by plasmonic NPs has been studied extensively over the past few decades. Khatua *et al.* demonstrated that the fluorescence of a weak emitter, crystal violet, can be enhanced more than 1000-fold by a single nanorod with an SPR of 629 nm excited at 633 nm.[239] This strong enhancement results from both an excitation rate enhancement of $\sim$130 and an effective emission enhancement of $\sim$9. Subsequently, much effort has been spent to prepare nanostructures that can generate a higher fluorescence enhancement based on the high local-field enhancement of gold bowties. A single molecule's fluorescence enhancement of up to a factor of 1340 was observed by exploiting gold bowties, which provides a useful balance between enhancement and losses for single-fluorescent-molecule-emission applications.[203]

Crystalline monolayers of transition metal dichalcogenides (TMDCs) are direct band gap 2D semiconductors and are promising as light-active materials for optoelectronic applications. Although TMDCs have shown great potentials in ultrafast and ultrasensitive photodetectors, their applications are limited by their low photoluminescence due to their low quantum efficiency and weak absorption. By suspending WSe$_2$ flakes onto a gold substrate with sub-20 nm-wide trenches (Fig. 27a),
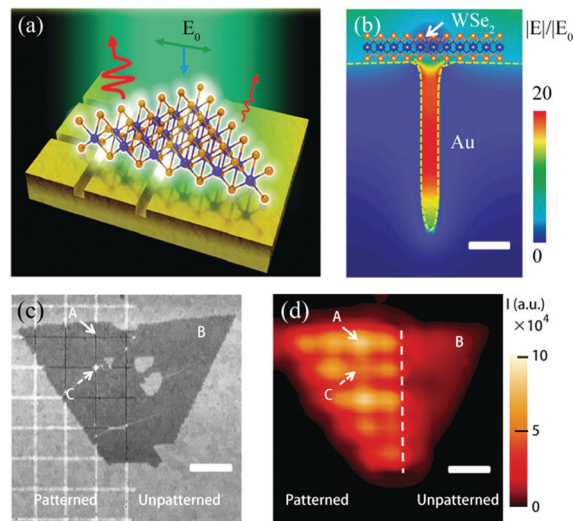

Fig. 27 (a) Schematic of PL emission from a single-crystal monolayer of a WSe$_2$ flake on a gold substrate. Part of the triangular flake rests on the patterned region of the substrate consisting of sub-20 nm-wide trenches. (b) Representative simulation of the electric-field distribution of the lateral gap plasmons with a WSe$_2$ monolayer flake suspended over a single trench. The polarization of the incident laser field is across the gap. The dashed yellow line denotes the boundary between air and gold. Scale bar: 20 nm. (c) SEM image of a crystalline WSe$_2$ monolayer flake transferred onto a template-stripped substrate with a pitch of 760 nm. 'A' points to a portion of WSe$_2$ suspended above an intersection of two underlying trenches, while 'B' corresponds to the reference point, that is, WSe$_2$ on unpatterned smooth gold. 'C' points to a tear defect in the monolayer. Scale bar: 1 μm. (d) PL intensity (*I*) mapping on the WSe$_2$–gold plasmonic hybrid structure showing larger signals from the patterned regions and resolvable modulations in the intensity. Scale bar: 1 μm. The intensity value at each pixel was obtained by integrating the PL spectrum across the spectrum window of 700–820 nm. A 532 nm pump laser was chosen here for a fine PL mapping resolution. Reproduced from ref. 240 with permission. Copyright (2016) the authors.

Wang *et al.* reported a giant photoluminescence enhancement of $\sim$20 000-fold.[240] In their work, the resonances were in the form of lateral gap plasmons in the trenches with *E*-fields predominantly parallel to the plane of WSe$_2$ to promote strong light absorption (Fig. 27b), which could be tuned to be matched with the pump laser wavelength by varying the pitch of the structures. The enhanced Purcell factor by the plasmonic substrate gave rise to a 37-fold photoluminescence (PL) enhancement compared with the emission from WSe$_2$ on sapphire (Fig. 27c and d).

All-dielectric nanophotonics can also serve as a platform for high-efficiency single-molecule detection and exhibit extra advantages compared with plasmonic structures. On the one hand, the low Ohmic losses in dielectric NPs prevent parasitic heating of the analyzed objects. On the other hand, the high radiative part of the Purcell factor and directivity improve signal extraction. Regmi *et al.* utilized all-dielectric nanoantennas based on silicon dimers to enhance the fluorescence detection of single molecules.[241] The silicon antenna design was optimized to confine the near-field intensity in the 20 nm nanogap and achieved a 270-fold fluorescence enhancement in a nanoscale volume of $\lambda^3/1800$. As shown in Fig. 28a, an
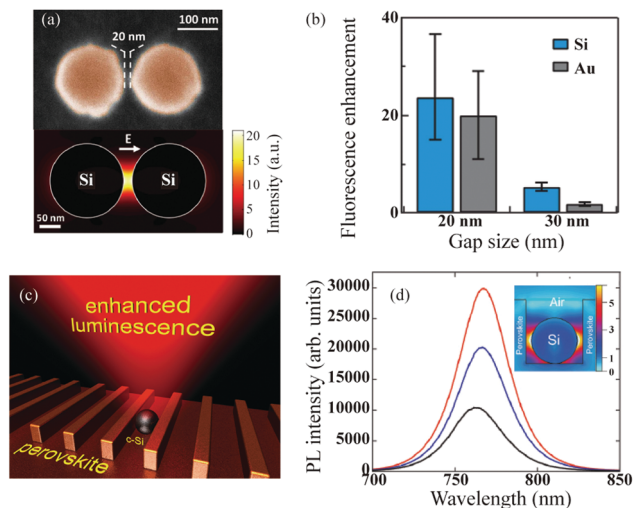
Fig. 28 (a) SEM image of a silicon dimer of 170 nm diameter with a 20 nm gap. The silicon thickness is 60 nm. FDTD simulation of the electric–field-intensity enhancement at the plane located at the center height of the silicon dimer. The antenna is normally illuminated at λ = 633 nm from the glass substrate with a linear electric field polarized parallel to the dimer axis. (b) Comparison of the fluorescence enhancement between a dielectric dimer and metallic dimer of similar gap size, with the excitation electric field parallel to the dimer axis. (c) Schematic illustration of luminescence enhancement from a hybrid perovskite metasurface decorated by resonant silicon NPs. (d) Photoluminescence modulation by Si NPs: signal from the blank perovskite (black line), perovskite metasurface (blue line), and perovskite metasurface with Si NPs (red line). (a and b) Reproduced from ref. 241 with permission. Copyright (2016) American Chemical Society. (c and d) Reproduced from ref. 242 with permission. Copyright (2017) Royal Society of Chemistry.

electric-field-intensity enhancement around 21.5 was achieved in the 20 nm gap when the incident polarization was along the dimer axis, with a spatial distribution typical of electric dipolar resonance. Furthermore, the results displayed in Fig. 28b indicate that the silicon antennas have fluorescence enhancement and optical confinement properties that are very similar to the gold antennas with similar gap sizes. If a silicon NP is located onto perovskite metasurface, the coupling between them causes a 200% enhancement of the photoluminescence intensity,[242] as illustrated in Fig. 28c and d.

5.4 Surface-enhanced infrared absorption

Mid-IR spectroscopy is an especially powerful technique that directly excites the vibrational transitions in the 3–20 μm ($\sim$3000–500 cm^{-1}) range, which is relevant to most organic molecules, as displayed in Fig. 29a.[243] By virtue of the 'chemical fingerprint,' infrared measurements can be exploited for automated tissue classification and cancer identification. Despite their potentials, IR absorption measurements are fundamentally limited as a result of the small cross-sections of molecules.[244,245] Besides, the strong IR absorption of liquid water presents additional obstacles to perform measurements in biomolecules' native, aqueous environments. One promising method for increasing sensitivity is to leverage the electric-field enhancement associated with the excitation of plasmonic resonances
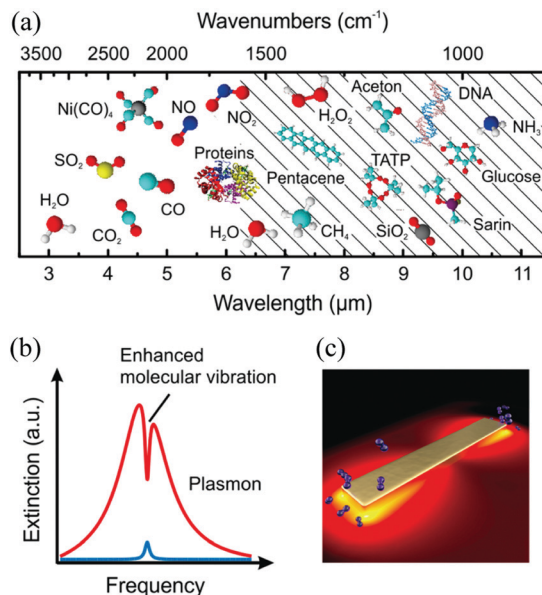

Fig. 29 (a) Characteristic infrared vibrations of selected molecular species. The fingerprint region containing skeletal vibrations is hatched. (b and c) Principle of resonant SEIRA: infrared vibrations of molecules located in the enhanced electromagnetic near field of a plasmonic nanostructure (nanoantenna) are enhanced if the plasmon (red) is resonantly matched to the molecular vibration (blue). Reproduced from ref. 243 with permission. Copyright (2017) Royal Society of Chemistry.

(Fig. 29b and c), i.e., so-called surface-enhanced infrared absorption (SEIRA). The enhancement of IR vibrational modes scales as $|E|^2$ of the local field. Although this was first proposed in the infrared band, a similar idea has been extended to the terahertz and far IR band.[246]

Early studies mostly relied on metal island films, prepared either by physical vapor deposition or chemical means.[247] Subsequent work has shown that using plasmonic nanoantennas is an extremely promising approach, with a number of important advantages.[248] The resonant frequencies, determined by the size, shape, and composition of the metal structure can be tuned across specific frequency ranges of the electromagnetic spectrum. If a metallic antenna structure has a plasmon resonance at the same frequency as a molecular vibration, the metal and molecule systems can couple, resulting in spectral features with Fano line shapes characteristic of a coupling between broad and narrow energy states.[243,248]

Nanorods and nanoslits are two typical structures. Many SEIRA antennas investigated thus far are based on a rod-shaped geometry that exploits the "lightning-rod effect" in the mid-IR region of the spectrum. Systematic investigations of plasmonic nanoslits and nanorods have been performed.[249] Also, nano split-ring resonators with a nanometer-sized gap offer potentially larger near-field enhancement inside the gap region, which would lead to higher signal enhancements. Based on such structures, Cubukcu et al. reported a surface-enhanced molecular detection technique with zeptomole sensitivity.[250]

The bowtie antenna, another widely used design, improves the localization of the near field. Recently, a transformation
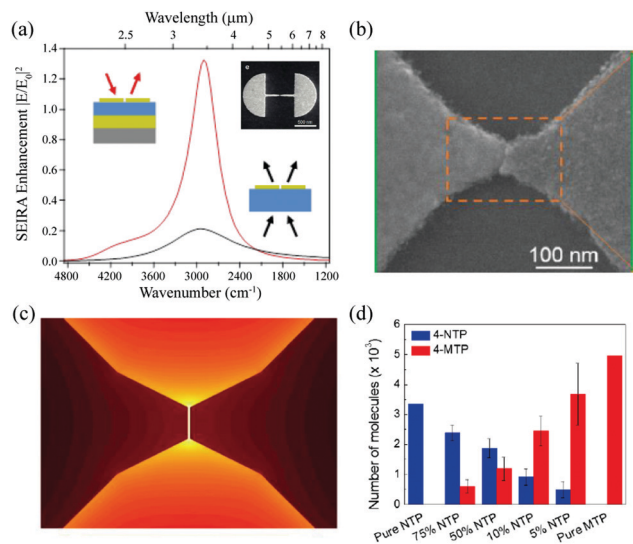
Fig. 30 (a) SEIRA enhancement for a fan antenna on a reflective substrate (red) and on a SiO$_2$ substrate (black) inset: SEM images of a fan antenna. (b) SEM image of the nanogap at the center of a bowtie antenna. (c) 2D map of peak field enhancement (at 1536 cm^{-1}). (d) Quantitative analysis of a number of 4-NTP (blue) and 4-MTP (red) molecules on Au surface in the gap after functionalization in mixed solutions of varied molar percentages. Error bars represent the standard deviations of the number of molecules obtained from five individual antennas on the same substrate. (a and b) Reproduced from ref. 251 with permission. Copyright (2015) American Chemical Society. (c and d) Reproduced from ref. 252 with permission. Copyright (2017) American Chemical Society.

of a bowtie antenna, *i.e.*, a fan-rod antenna, was introduced (Fig. 30a). This design combines the advantages of both the rod and bowtie antennas, with high spatial confinement and enhancement of the near-field intensity. The optimum enhancement was achieved for a layer thickness slightly smaller than a quarter of the wavelength. Following this approach, the near-field intensity could be increased by nearly an order of magnitude, enabling the detection of 10^4 alkanethiol molecules ($\sim$20 zeptomoles) using a single antenna structure and a standard commercial Fourier transform infrared (FTIR) spectrometer.

Dong *et al.* investigated the SEIRA responsivity of a bowtie plasmonic antenna design incorporating a sub-3 nm gap positioned above an Au film with a SiO$_2$ spacer layer (Fig. 30b–d).[252] They reproduced a self-aligned technique to fabricate antennas with ultrasmall gaps not typically achievable using standard e-beam lithographic approaches. This 3D geometry tightly confines incident mid-IR radiation into its ultrasmall junction, yielding a hot spot with a theoretical SEIRA enhancement factor of more than 10^7. They quantitatively evaluated the IR detection limit of this antenna design using mixed monolayers of 4-nitrothiophenol (4-NTP) and 4-methoxythiolphenol (4-MTP). The optimized antenna structure allowed the detection of as few as $\sim$500 molecules of 4-NTP and $\sim$600 molecules of 4-MTP.

It should be noted that, most of these structures tend to be designed to be excited with a specific polarization of the incident light. Such polarization-sensitive structures suffer from a loss of

half of the incident light energy from an unpolarized source, thus failing to maximize the photon numbers interacting with biomolecules. In order to overcome this limitation, Cetin *et al.* proposed a polarization-insensitive mid-IR nanoring antenna fabricated on a dielectric nanopedestal to provide maximum field overlap with the target biomolecules.[253] With the engineered ring NPs on the nanopedestal, they successfully detected the Amide-I and II vibrational modes of a protein–antibody bilayer.

Generally, SEIRA based on resonant antenna is narrowband and thus cannot cover the whole vibrational bands of molecules. However, by combining two resonant antennas together, dual band absorption enhancement has been realized.[254] Log-periodic trapezoidal optical antennas have been utilized as multifrequency optical antennas for operating with a bandwidth of several octaves.[255]

Hu *et al.* demonstrated a hybrid graphene plasmonic structure on a CaF$_2$ nanofilm (Fig. 31), enabling an electrically tunable plasmon that covers the entire molecular fingerprint region for molecular detection with extremely high sensitivity down to the submonolayer level.[256] A 20-fold enhancement of sensitivity was achieved for the unambiguous identification of vibrational fingerprints in polymers at the nanoscale with an FTIR spectroscope. Furthermore, undisturbed and highly confined graphene plasmon offers the simultaneous detection of in-plane and out-of-plane vibrational modes with ultrahigh
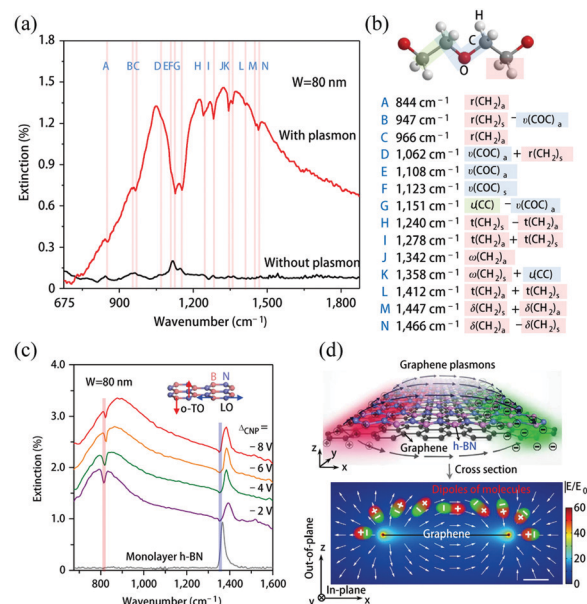

Fig. 31 (a) Comparison of the sensing results for an 8 nm-thick polyethylene oxide (PEO) film with (red curve) and without (black curve) graphene plasmon enhancement. The corresponding Fermi level was $\sim$0.2 eV. The red vertical lines indicate various PEO molecular vibrational modes. (b) List of the PEO vibrational modes in the molecular fingerprint region and their positions in (a). (c) Extinction spectra (colored lines) of the graphene plasmon sensor covered with an h-BN monolayer. The vertical lines indicate the positions of the optical phonon modes of the h-BN monolayer. (d) Schematic diagram of the interaction between the electric field of the graphene plasmon and the monolayer h-BN structure vibrations. Scale bar: 20 nm. Reproduced from ref. 256 with permission. Copyright (2016) the authors.

detection sensitivity down to the sub-monolayer level, significantly pushing the current detection limit of far-field mid-IR spectroscopies.

6. Enhanced optical fields for broadband absorption and energy conversion

The plasmon energy damping process involves the optical absorption and Ohmic loss of metal. On the one hand, this process gives rise to Joule heat. For strong field localization, it leads to a considerable concentration of temperature increase. This effect constitutes the basis of the emerging field of thermoplasmonics.[257] It has been exploited for optically assisted drug delivery, cancer therapy, optical switching, and heat-assisted photochemistry.[258,259] In all these applications, optimum designs of plasmonic structures are crucial to produce extraordinary field enhancement at designated spatial locations. On the other hand, after light absorption in the plasmonics structures, plasmons will decay, transferring the accumulated energy to electrons in the conduction band of the material. This process produces high energy electrons, also known as 'hot electrons' which can escape from the plasmonic nanostructures and be collected by, for example, putting the plasmonic nanostructures in contact with a semiconductor, thereby forming a metal–semiconductor Schottky junction. This scheme for solar energy conversion opens up a new way to realize novel photovoltaic, photodetector and photocatalytic devices,[260–263] whose performances may rival, or even exceed, those of conventional devices.

6.1 Broadband absorption

The study of ideal absorbers that can efficiently absorb light over a broad range of wavelengths is of fundamental importance as well as critical for many applications, from solar steam generation and thermophotovoltaics to light/thermal detectors.

Subwavelength structures find widespread applications in high-efficiency electromagnetic absorbers, where the reflection and transmission are simultaneously suppressed. In 2008, a perfect metamaterial absorber was proposed with a thickness of only $\lambda/40$ but high absorption peaks of up to 96%.[264] Landy et al. interpreted the principle of this absorber as the simultaneous control of the electric and magnetic responses, such that the impedance is matched to the free space. However, it is ambiguous to define the μ_{eff} and ε_{eff} in such complex structures, since a metamaterial perfect absorber cannot be strictly considered as an homogeneous bulk medium. In contrary to the metamaterial concept, it was shown that the effective impedance was more physically meaningful and beneficial in describing the electromagnetic properties of metasurface absorbers. A general equivalent model of a meta-mirror was proposed, where the subwavelength structure was taken as a thin impedance layer.[265] Following this principle, a wide-angle polarization-independent dual-band absorber was demonstrated at frequencies of 100 THz and 280 THz with absorption close to 100%.

Although near-perfect absorbers have been realized at different bands, from microwave to the optical band, most of them only operate at a narrow frequency due to the resonant nature of the metamaterial. Broadband absorption is highly desirable in many applications, such as solar energy harvesting and photovoltaic devices. As an attempt to extend the absorption band, multiple resonant structures at different frequencies are integrated into one unit cell. For instance, more than 20 metal–dielectric pairs with slow dimension-variation can be vertically cascaded to insure resonant frequencies close to each other.[266] Naturally though, the cascading method to extend the absorption bandwidth occurs at a cost of an increased device thickness and fabrication complexity. Therefore, it is quite challenging to realize an ultrabroadband absorber with limited thickness.

Dispersion engineered subwavelength materials offer an effective method to overcome the disadvantages mentioned above. By mimicking the impedance of a perfect impedance matched layer through frequency dispersion engineering of a cross-shaped metasurface, a broadband IR absorber was realized.[267] With a thin layer of structured nichrome, a polarization-independent absorber with an absorption larger than 97% was numerically demonstrated over a bandwidth larger than one octave. Similarly, both one dimensional[268] and two dimensional[269] dispersion engineering strategies have been proposed for broadband polarization conversion.

Based on heavily boron-doped silicon grating, another simple yet powerful broadband terahertz absorber was also demonstrated.[270–272] Through utilizing both the zero- and first-order diffractions in the doped silicon wafer, a relative absorption bandwidth larger than 100% was achieved. Furthermore, this design can be easily extended to higher frequencies as the optical property of doped silicon can be tuned through changing the doping concentration. Recently, lithography-free CMOS-compatible AlCu alloys have been demonstrated to possess >99% absorption at selected wavelengths, ranging from the visible to the near-infrared region of the spectrum, depending on its thickness.[273] The near-unit absorption can be maintained for an oblique angle of incidence up to 70°.

It should be mentioned that most of the absorbers mentioned above are based on noble metals, which suffer from the severe problem of low melting points.[274] In contrast, solar thermophotovoltaics (STPVs) generally require a working temperature of at least 800 °C, i.e., approaching or even surpassing the melting points of bulk Au and Ag. Based on a refractory plasmonic material, titanium nitride, a broadband absorber with an average absorption of 95% over the range of 400–800 nm and a total thickness of 240 nm, was demonstrated.[275] In contrast to noble metal optical absorbers, the TiN absorber performed well at high temperatures and endured strong light illumination due to its high melting point.

Based on diffraction/interference engineering, Huang et al. proposed an absorber showing absorption of over 95% spanning a broad range of frequencies from UV (200 nm) to the near-NIR (900 nm) even at high operation temperatures (Fig. 32).[276] Different from the typical metal–dielectric–metal profile, this design was
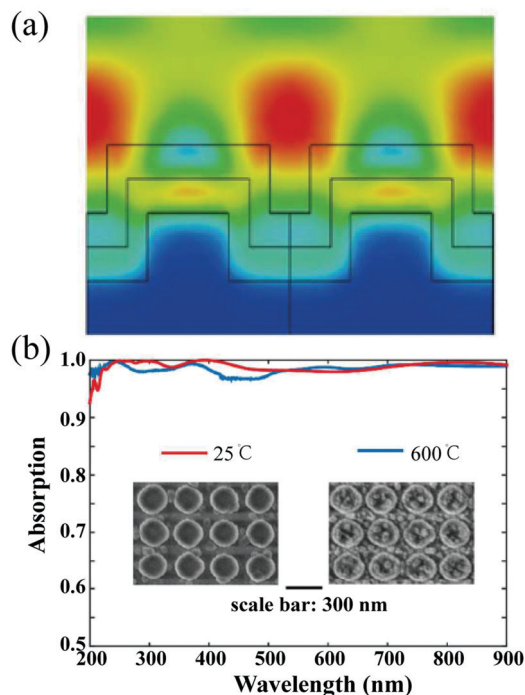
Fig. 32 (a) Electric field distribution at λ = 300 nm. (b) Absorption spectra and SEM image of the device at room temperature and after annealing at 600 °C. The absorption performance as well as the nanostructured configurations were nearly unchanged after annealing, which demonstrated the high temperature tolerance of the absorber. Reproduced from ref. 276 with permission. Copyright (2018) Royal Society of Chemistry.

formed by dielectric–semiconductor–metal tri-layers with a period smaller than the working wavelength. Interference lithography was used to produce the nanostructure configuration, which was comparatively simple, cost-effective, and more suitable for large-scale fabrication. Since the adopted absorption material is refractory, this ultrabroadband absorber can be used in solar-thermal harvesting industry and STPV applications.

Zhou et al. reported a plasmonic absorber fabricated through the self-assembly of metallic NPs onto a nanoporous template by a one-step deposition process.[277] A nanoporous alumina template was used to form a percolated scaffold for hosting the gold NPs, as shown in Fig. 33a and b. This structure could enable an average measured light absorbance of ~99% throughout the visible to mid-IR regimes (400 nm to 10 μm) (Fig. 33c and d). Two key components contributed to the high efficient and broadband absorption: (1) the gold NPs with random sizes and distributions enable a high density of hybridized LSPR to effectively absorb light in a wide wavelength range; (2) the nanoporous templates provide an impedance match for efficient reflection reduction and coupling to the optical modes. Such plasmonic absorbers can be used directly for efficient solar steam generation because of the highly efficient, broadband absorption, unique porous nature of the templates, and widely spread hot spots.

6.2 Photothermal therapy

Photothermal heating is an inherent effect resulting from the strong absorption of optical energy.[278] Recent years have seen a
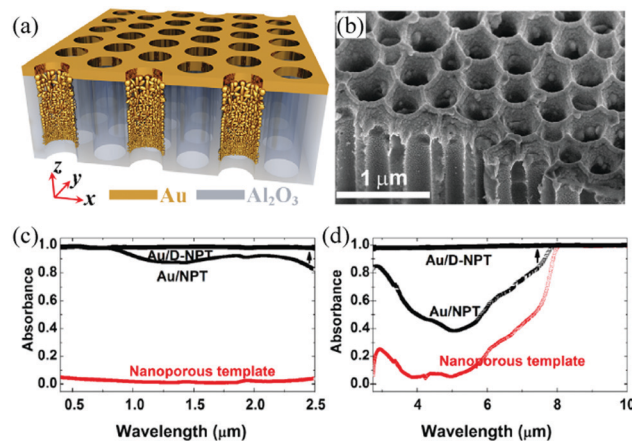

Fig. 33 (a) 3D schematic of self-assembled plasmonic absorbers. (b) 3D SEM image of a typical Au/NPT sample. (c) Experimental absorption spectra measured by an integrated sphere in the visible and near-IR regimes. (d) Experimental absorption spectra measured by specular reflectance in the mid-IR regime. Reproduced from ref. 277 with permission. Copyright (2016) the authors.

growing interest in using nanostructures to control the temperature on the nanoscale. Under illumination, a NP features enhanced light absorption, turning it into an ideal localized nano-source of heat, which is controllable remotely using light. Such a powerful and flexible photothermal scheme is particularly useful for the hyperthermia/thermal ablation of cancer cells in so-called photothermal therapies (PTT).[279–282] For the purpose of the thermal therapy of tumors, it is necessary to induce well-localized heating so that a significant temperature increase is achieved in the tumor while keeping the temperature of the surrounding tissue at a normal level. An ideal NP for photothermal therapy should have the following features: (1) NIR absorption between 700–1000 nm, which should also show minimal absorption and scattering by water, hemoglobin, skin, and other biomolecules of tissue components, (2) a large absorption cross-section, (3) a size below 100 nm to enhance tumor uptake and to reduce sequestration by the reticulo-endothelial system, (4) low toxicity and biocompatibility of the chemical components, and (5) good solubility in biocompatible liquids.[278,282] Recently, metallic NPs,[283–285] semiconductor quantum dots,[282] carbon nanotubes,[286,287] and single-layered nano-reduced graphene oxide[288,289] have been used as light-activated heating nanosystems that can be incorporated into tumors, allowing high heat administration in the tumor area in PTT, and minimizing the damage in the surrounding healthy tissue.

The use of plasmonic NPs as highly enhanced photoabsorbing agents for efficient cancer therapy is named plasmonic photothermal therapy (PPTT). On account of the phenomenon of LSPR of the metal NPs, strongly enhanced NIR light absorption that is several orders of magnitude more intense compared with conventional laser phototherapy agents can be induced. Gold NPs are especially suited to the thermal destruction of cancer due to their high efficiency absorption in the NIR and ease of surface functionalization as well as photothermal heating ability. In addition, Au is a particularly attractive material because of its biocompatibility and low cytotoxicity.
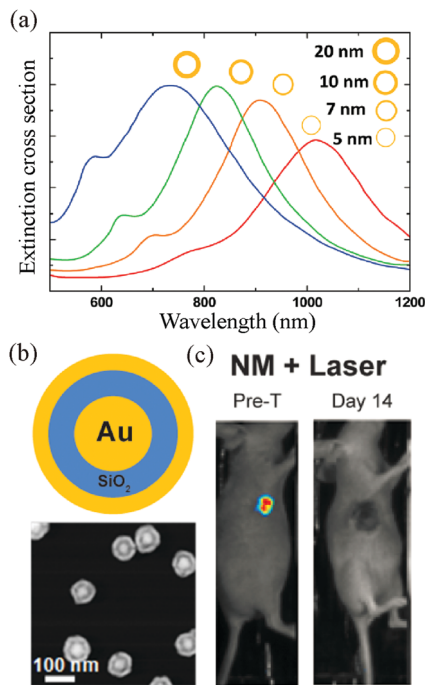
Fig. 34 (a) Extinction cross-section spectra (in arbitrary units) of core (silica)–shell (gold) NPs with different shell thicknesses. (b) Schematic and SEM image of nanomatryoshkas with the dimensions. (c) Photothermal therapy by bioluminescence imaging of mice injected with nanomatryoshkas on day 14. (a) Reproduced from ref. 290 with permission. Copyright (2004) SAGE Publishing. (b and c) Reproduced from ref. 291 with permission. Copyright (2014) American Chemical Society.

Various Au nanostructures have been prepared with controlled sizes and compositions, including nanoshells, nanorods, nanocages, nanostars, and nano matryoshkas.[278,283,284,290,292–294] These nanostructures have been demonstrated to be capable of being used for deep tissue penetrating applications of PTT. Fig. 34a shows a Mie scattering plot of the nanoshell plasmon resonance wavelength shift as a function of nanoshell composition for the case of a 60 nm core gold/silica nanoshell.[290] The optical response of gold nanoshells depends dramatically on the relative size of the NP core and on the thickness of the gold shell. By varying the relative core and shell thicknesses, the color of gold nanoshells can be varied across a broad range of the optical spectrum spanning the near-IR spectral regions in the first biological windows.[295] Ciceron *et al.* reported a study of ~90 nm diameter Au nanomatryoshkas (Au/SiO$_2$/Au) for PTT efficacy in highly aggressive triple negative breast cancer (TNBC) tumors in mice.[291] A schematic and SEM image of the nanomatryoshkas are shown in Fig. 34b. The authors demonstrated that nanomatryoshkas were strong light absorbers with 77% absorption efficiency. After an intravenous injection of Au nanomatryoshkas followed by a single NIR laser dose of 2 W cm^{-2} for 5 min, 83% of the TNBC tumor-bearing mice appeared healthy and tumor free >60 days later. The smaller size and larger absorption cross-section of the Au nanomatryoshkas combined to make this NP effective for photothermal cancer therapy, which was demonstrated in the mice treatment experiments as shown in Fig. 34c.
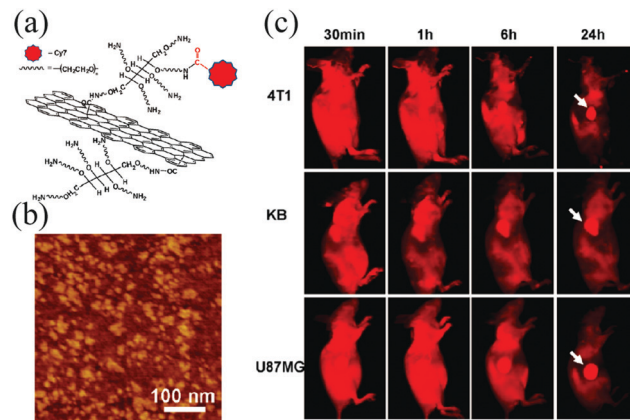

Fig. 35 (a) Scheme of a NGS with PEG functionalization and labeled by Cy7 dye. (b) AFM image of NGS-PEG. (c) Spectrally unmixed *in vivo* fluorescence images of 4T1 tumor-bearing Balb/c mice, KB, and U87MG tumor-bearing nude mice at different time points post injection of NGS-PEG-Cy7. Mouse autofluorescence was removed by spectral unmixing in the above images. High tumor uptake of NGSPEG-Cy7 was observed for all of the three tumor models. Hairs on Balb/c mice were removed before fluorescence imaging. Reproduced from ref. 288 with permission. Copyright (2010) American Chemical Society.

The *in vivo* PTT behaviors of nanographene sheets (NGS) with a polyethylene glycol (PEG) coating were also studied by Yang *et al.*[288] The strongly localized optical absorbance of NGS in the NIR region was utilized for *in vivo* PTT, achieving ultra-efficient tumor ablation after the intravenous administration of NGS and low-power NIR laser irradiation (close to 2 W cm^{-2}) on the tumor using an 808 nm laser beam, as shown in Fig. 35. The laser-induced heating effect was high enough to eliminate the tumor. Compared with gold nanomaterials, such as gold nanorods, the performance of PEGylated NGS appeared to be comparable to that of PEGylated Au nanorods in terms of the administration routes, injected doses, NIR laser densities, and irradiation durations. However, as the authors declared, graphene with all-sp^2 carbon atoms exposed on its surface has an ultrahigh surface area available for efficient drug loading with a uniquely high molecular loading capacity.

6.3 Photovoltaic energy conversion

Crystalline silicon is one of mostly used materials for photovoltaic cells, which can effectively convert sunlight into clean electrical power. However, traditional solar cells based on crystalline silicon wafers generally suffer from large thicknesses (typically between 180–300 μm). As an alternative, thin-film solar cells may provide a viable pathway toward the large-scale implementation of photovoltaic technology by offering low material and processing costs. An important challenge for lowering the cost of electricity produced by photovoltaic solar cells is to reduce their thickness without compromising on their high performance. In essence, this means that a high fraction of the incident light must be absorbed and converted to long-lived excited charge carriers, despite a reduction of the used amount (thickness) of semiconductor material. A method for achieving light trapping in thin-film solar cells is the use of

metallic nanostructures that support surface plasmons.[17–19] By proper engineering of these metallodielectric structures, light can be concentrated and squeezed into a thin semiconductor layer, thereby increasing the absorption. A seminal work was done by Green's group, which reported a 7-fold enhancement for wafer-based cells at λ = 1200 nm and an up to 16-fold enhancement at λ = 1050 nm for 1.25 μm thin silicon-on-insulator (SOI) cells.[19]

Compared with crystalline Si, hydrogenated amorphous silicon (a-Si:H) offers a much larger absorption coefficient across the solar radiation spectrum. To enable efficient solar cell operation, ∼500 nm thickness of a-Si:H is required. However, the high defect densities typically present in a-Si:H thin films limit the typical minority carrier diffusion lengths to ∼100 nm.[18] Derkacs et al. reported an enhancement in short-circuit current density and energy-conversion efficiency in amorphous silicon p–i–n solar cells via the improved transmission of electromagnetic radiation arising from forward scattering by SPP modes in Au NPs deposited above the amorphous silicon film.[18] For an Au NP density of ∼3.7 × 10^8 cm^{-2}, an 8.1% increase in short-circuit current density and an 8.3% increase in energy-conversion efficiency were observed.

There are mainly three plasmonic light-trapping geometries and schemes to improve the energy-conversion efficiency of thin-film solar cells.[296] First, light is scattered from metal NPs at the surface of the solar cell and experiences multiple reflections in the semiconductor film, causing an increase in the effective optical path length in the cell. Second, the excited SPPs cause the creation of electron–hole pairs in the semiconductor. Third, a corrugated metal back surface couples light to SPPs or photonic modes that propagate in the plane of the semiconductor layer. Thanks to these light-trapping techniques, one can significantly shrink the photovoltaic layer thickness, while keeping the optical absorption constant. An optimal condition for maximized optical absorption in ultrathin films has been derived,[20] determined by the ratio of the external media refractive indices.

Dielectric NPs can also provide sufficient scattering, especially if their dielectric permittivity is quite high. Moreover, a number of dielectrics possess a very low dissipation level at visible wavelengths. Therefore, it is expected that dielectric NPs would exhibit comparable or even better enhancement in solar cell performance, as indicated in Fig. 36.[297] In addition, such nanostructures can be synthesized using a variety of conventional deposition techniques similar to the ones used for solar cell manufacturing.

Recently, 10 μm-thick crystalline silicon photovoltaics with a peak efficiency of 15.7% were demonstrated using periodic 2D inverted nanopyramid surface texture and rear metallic reflector light-trapping structure.[298] Ha et al. proposed an antireflection coating based on silicon dioxide (SiO$_2$) nanospheres that improved solar cell absorption by coupling light from free space into the absorbing layer through excitation of the modes within the nanospheres. The deposited monolayer of nanospheres led to a significant increase in light absorption within an underlying semiconductor in the order of 15–20%.[299]
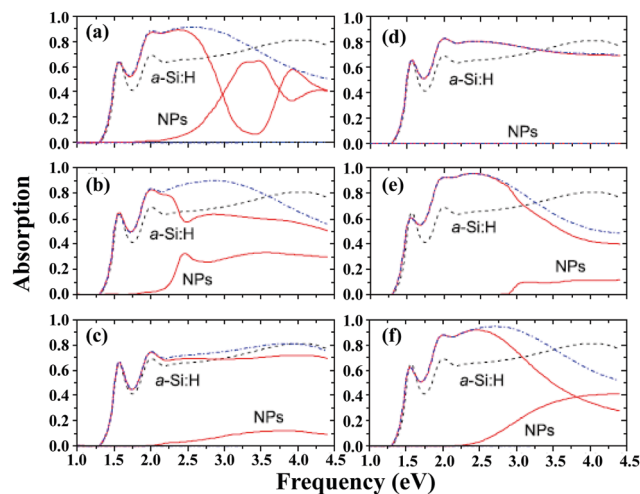

Fig. 36 Spectral absorption rates of an a-Si:H layer and a nanoparticle array (the solid lines) optimized for (a) Ag, (b) Au, (c) Cu, (d) SiO$_2$, (e) SiC, and (f) TiO$_2$ nanoparticles. The reference cell response is plotted as the dashed line; the dash-dotted lines show the contribution of the ideal nondispersive material. Reproduced from ref. 297 with permission. Copyright (2010) American Institute of Physics.

One notable single-junction silicon solar cell had an efficiency of 25.6% and short-circuit current of 41.8 mA cm^{-2}.

Organic solar cells (OSCs) offer a promising alternative to inorganic solar cells due to their low cost, easy fabrication, and compatibility with flexible substrates over a large area. Nevertheless, the power conversion efficiency of OSCs is strictly limited for practical applications, which is mainly attributed to the low carrier mobility of organic materials. An effective approach to enhance the efficiency of a thin film OSC is to increase the light absorption of the organic film without increasing the photoactive layer thickness. SPR enhancement is naturally suited to increase the optical absorption of organic semiconductors.

Fig. 37a and b show a schematic of an OSC based on a MIM structure.[300] The dielectric layer is composed of the organic semiconductors. One metal layer is continuous and acts as a cathode, and the other is a periodic nanowire structure simultaneously acting as a semi-transparent anode and converting the incident plane wave to surface plasmon waves. The MIM configuration forms a resonant cavity effect, which leads to a higher field intensity in the organic layers. For the TM illumination, the maximum fields are concentrated near the edges of the bottom and top Ag electrodes, as indicated in Fig. 37c. With such high local-field enhancement, about a 35% increase in the power-conversion efficiency was observed over that of conventional OSCs using a standard ITO electrode (Fig. 37d).

It should be noted that the use of metallic nanostructures has the tendency to increase parasitic optical absorption loss due to the metal, which competes with absorption in the active layer. Also, structuring the active layer can be challenging since it is solution-processed and must retain a short path to the electrical contacts for efficient charge-carrier extraction. Alternatively, Raman et al. demonstrated that 1D, 2D, and multi-level ITO-air
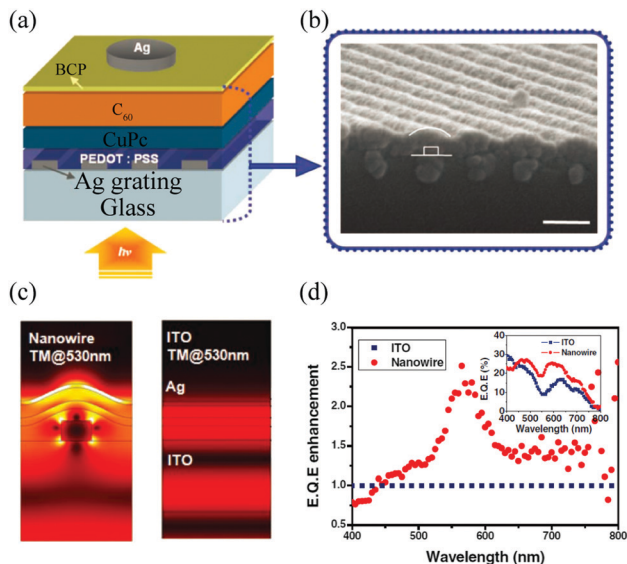
Fig. 37 (a) Schematic of a plasmonic organic cell with a Ag nanowire anode. (b) SEM image (cross-section) of a fabricated device where a 70 nm thick top Ag cathode is absent. Scale bar: 200 nm. (c) Simulated electric field profiles of nanowire and ITO devices at the wavelength of 530 nm for TM illumination. (d) External quantum efficiencies (EQE) enhancement of a nanowire device with reference to an ITO device. The inset gives the measured EQE of the nanowire and ITO devices. Reproduced from ref. 300 with permission. Copyright (2010) Wiley-VCH Verlag.

Fig. 38 Sunlight is converted into useful thermal emission and, ultimately, electrical power, *via* a hot absorber–emitter: (a) schematic and (b) optical image. (c) Relative improvements in efficiency and near-term predictions for nanophotonic area-ratio optimized STPVs. Reproduced from ref. 303 with permission. Copyright (2014) Nature Publishing Group.

gratings lying on top of the OSC stack could produce an 8–15% increase in photocurrent for organic solar cells.[301]

Le *et al.* theoretically investigated and compared the influence of square silver gratings and one-dimensional (1D) photonic crystal (1D PC)-based nanostructures on the light absorption of OSCs with a thin active layer. They showed that, by integrating the grating inside the active layer, excited localized surface plasmon modes may cause strong field enhancement at the interface between the grating and the active layer, which results in a broadband absorption enhancement of up to 23.4%. Apart from using silver gratings, they showed that patterning a 1D PC on top of the device may also result in a comparable broadband absorption enhancement of 18.9%. This enhancement is due to light scattering of the 1D PC, coupling the incoming light into 1D PC Bloch and SPR modes.[302]

It should be mentioned that photovoltaic power generation typically only exploits a portion of the solar spectrum efficiently. There is, therefore, an increasing need for hybrid technologies for solar power generation.[303] By converting sunlight into thermal emission tuned to energies directly above the photovoltaic band gap using a hot absorber–emitter, STPVs promise numerous benefits, such as high efficiency by harnessing the entire solar spectrum, scalability, and compactness, because of their solid-state nature.

A STPV cell mainly includes several processes: optically concentrated sunlight is converted into heat in the absorber, the absorber temperature rises, heat conducts to the emitter, and the hot emitter thermally radiates toward the photovoltaic cell, where radiation is ultimately harnessed to excite charge
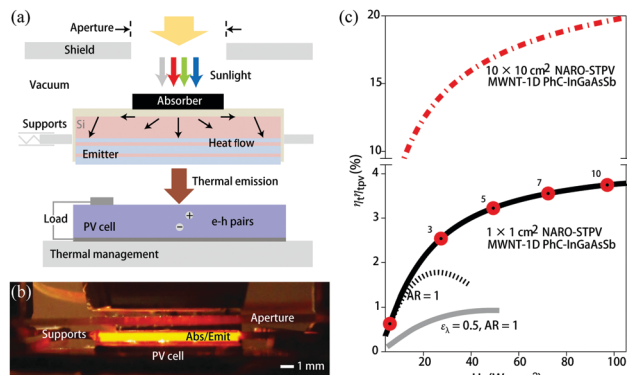
carriers and generate power. According to the processes above, the overall efficiency (η_{stpv}) can be expressed as a product of the optical efficiency of concentrating sunlight (η_o), the thermal efficiency of converting and delivering sunlight as heat to the emitter (η_t), and the efficiency of generating electrical power from the thermal emission (η_{tpv}):

$$\eta_{stpv} = \eta_o \eta_t \eta_{tpv}. \quad (19)$$

In order to improve the whole conversion efficiency, Lenert *et al.* proposed a device integrating a multiwalled carbon nanotube absorber and a 1D Si/SiO$_2$ photonic-crystal emitter on the same substrate, with the absorber–emitter areas optimized to tune the energy balance of the device, as shown in Fig. 38a and b.[303] The broad-spectrum absorptance of the nanotube array exceeded 0.99. Experimental results showed that the total energy conversion efficiency reached 3.2%. By using an improved InGaAsSb cell and a sub-band-gap photon-reflecting filter, the STPV efficiency approached 20% at moderate optical concentrations (Fig. 38c).

6.4 Surface plasmon-enhanced photodetectors

The ability of plasmonic structures to manipulate light well below the classical diffraction limit is giving rise to a myriad of new chip-scale photonic components. Among the many emerging applications, surface plasmon-enhanced photodetectors are particularly important.[238,304–307] Since the speed of a detector (determined by its carrier transit time) and power consumption are respectively proportional to the length and volume of the device, reducing the detector size would result in increased speed, decreased noise, and reduced power consumption.

As plasmonic structures can concentrate light both laterally and in the depth of a semiconductor material, they are ideally suited to this task. Plasmonic waveguide-based detectors have also recently been demonstrated and offer valuable integration advantages. Halas *et al.* made the seminal effort in integrating plasmonic antenna into a photodetector.[304] In their design, Au nanorod antennas integrated on n-type-doped silicon wafers were utilized to absorb incident light and generate hot

electrons. These hot electrons thereafter overcome the Schottky barrier at the metal–semiconductor interface and were injected into the semiconductor, contributing to a detectable photocurrent. In this configuration, photocurrent generation was no longer limited to photon energies above the band gap of the semiconductor, but rather to photon energies above the Schottky barrier height. Therefore, this device was capable of detecting light well below the band gap of the semiconductor at room temperature and without a bias voltage.

Conventional photodetection based on photoexcited electron–hole pairs in a semiconductor does not perform well for long-wavelength photons (especially for the millimeter and terahertz wave ranges) due to the relatively small photon energy and strong background thermal noise. Recently, Tong *et al.* proposed a new strategy for the direct detection of millimeter and terahertz wave photons based on LSPR-induced non-equilibrium electrons in antenna-assisted subwavelength Ohmic metal–semiconductor–metal (OMSM) structures (Fig. 39).[308] The subwavelength OMSM structure was used to convert the absorbed photons into localized SPPs, which then induced non-equilibrium electrons in the structure, while the antenna increased the number of photons coupled into the OMSM structure. When the structure was biased and illuminated, the unidirectional flow of the SPP-induced non-equilibrium electrons form a photocurrent. The energy of the detected photons was determined by the structure rather than the band gap of the semiconductor. The detection scheme was confirmed by simulation and experimental results of the devices, made of gold and InSb, and a room temperature noise equivalent power of 1.5×10^{-13} W Hz$^{-1/2}$ was achieved.

Graphene-based photodetectors have attracted strong interest for their exceptional physical properties, which include an ultrafast response across a broad spectrum, strong electron–electron interaction, and photocarrier multiplication.[309]
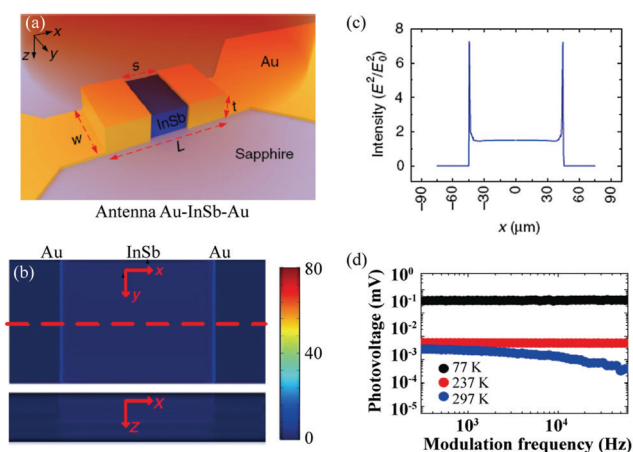

Fig. 39 (a) Schematic of an antenna-assisted subwavelength OMSM structure made of gold and InSb with $s = 90$ μm. (b) Numerical simulated 2D distributions of E^2/E_0^2 in x–y ($z = 0$) and x–z ($y = 0$) planes. (c) Retrieved field profile along the red dash in (b). (d) Photovoltage–frequency relations at three temperatures. The black, red, and blue dots correspond to 77, 237, and 297 K, respectively. Reproduced from ref. 308 with permission. Copyright (2017) the authors.
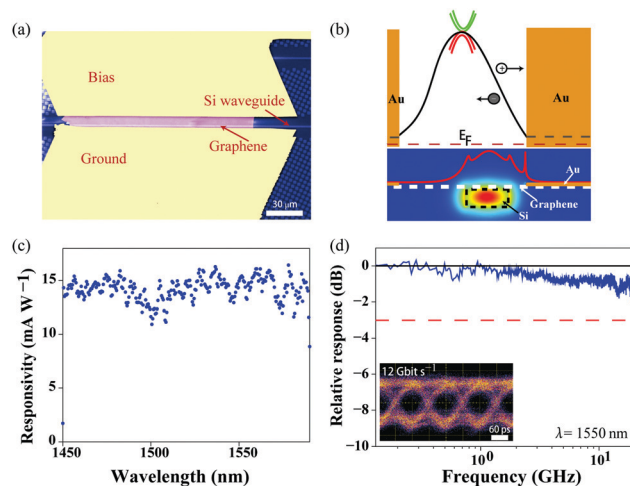

Fig. 40 (a) Optical microscopy top view of the device with a bilayer of graphene covering the waveguide. (b) Top: Potential profile (black solid line) across the graphene channel, showing band bending around the two metal electrodes. The red dashed line denotes the Fermi level. Bottom: Simulated electric field of the TE waveguide mode. The field intensity at the graphene position is shown as a red line. The top and bottom images are aligned horizontally by referring to the relative position of the waveguide; the position of the right electrode is symbolic. (c) Broadband uniform responsivity over a wavelength range from 1450 nm to 1590 nm at zero bias. (d) Dynamic optoelectrical response of the device. The relative a.c. photoresponse as a function of light-intensity-modulation frequency shows ∼1 dB degradation of the signal at a frequency of 20 GHz. Inset: 12 Gbit s^{-1} optical data link test of the device. Reproduced from ref. 311 with permission. Copyright (2013) Nature Publishing group.

However, the weak optical absorption of graphene limits its photoresponsivity. To address this issue, graphene has been integrated into nanocavities,[310] microcavities, and plasmon resonators, but these approaches restrict photodetection to narrow bands. Recently, Gan *et al.* demonstrated a waveguide-integrated graphene photodetector that simultaneously exhibited high responsivity, high speed, and a broad spectral bandwidth, as shown in Fig. 40.[311] Using a metal-doped graphene junction coupled evanescently to the waveguide, the detector achieved a photoresponsivity exceeding 0.1 AW^{-1} together with a nearly uniform response to wavelengths between 1450 and 1590 nm. Under zero-bias operation, the response rate exceeded 20 GHz.

6.5 Surface plasmon-enhanced photocatalysis

As one of the most promising solutions for energy shortages and environmental pollution, photocatalysis has attracted much attention because it is a green technology under the illumination of sunlight in ambient conditions.[262,263,312] Photocatalysis was first discovered by Aira Fujishima in 1967. Subsequent investigations have shown that this phenomenon should be attributed to initiating the reduction and/or oxidation of chemicals by utilizing a semiconductor to absorb photons to create active electrons and holes. When the semiconductor catalyst is illuminated with photons whose energy is equal to or greater than their band-gap energy, an electron is promoted from the valence band into the conduction band, leaving a hole behind. The excited electrons and holes migrate at the surface and exhibit a strong reduction and reductant capacity.
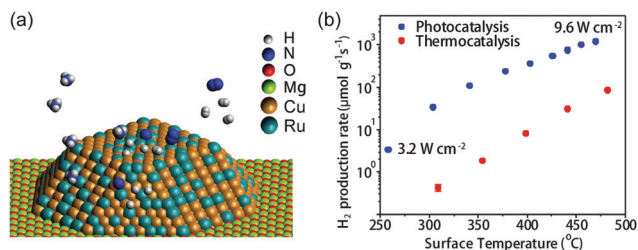
Fig. 41 (a) Schematic of the structure of Cu–Ru–AR consisting of a Cu NP antenna with a Cu–Ru surface alloy, where the Ru provides the reactor sites. (b) Comparison of the photocatalytic and thermocatalytic rates on Cu–Ru–AR. The horizontal axis corresponds to the surface temperature of the catalyst caused by photothermal heating (photocatalysis) or external heating (thermocatalysis). Reproduced from ref. 324 with permission. Copyright (2018) AAAS.

Up to date, although many efforts have been devoted to improving the performances of photocatalysts, there are still some drawbacks hindering their practical applications, such as short photogenerated electron–hole pair lifetime and a limited visible-light absorption. On the one hand, traditional high-performance photocatalytic materials, including TiO_2 and ZnO, generally operate at UV light, leading to a low-efficiency visible-light response. On the other hand, the recombination between the electrons and the holes is detrimental to the efficiency of a photocatalyst. For higher photocatalytic efficiency, the electron–hole pairs should be efficiently separated, and charges should be rapidly transferred across the surface/interface to restrain the recombination.[313] Fortunately, plasmonics provides an opportunity to overcome these difficulties.[25,314–323] Initially, metallic structures can generate LSPR at the visible band *via* tuning their shapes, dimensions, and materials. Utilizing metallic structures, the light can be localized and enhanced around the photocatalysts. Second, plasmons in the metal lead to the injection of energized charge carriers into the nearby adsorbate, which results in chemical transformation.

To differentiate the contributions of plasmon-induced hot electrons and photothermal heating, plasmonic antenna-reactor (AR) photocatalyst,[324] specifically a Cu–Ru surface alloy consisting of a Cu NP antenna and Ru reactor sites (Cu–Ru–AR), was prepared (Fig. 41a). The steady-state temperature on the photocatalyst surface was measured *in situ* with a thermal imaging camera. When NH_3 decomposition was performed without illumination, but with external heating temperatures equivalent to those achieved under illumination, the thermo-catalytic rates of H_2 production were one to two orders of magnitude below the observed photocatalytic rates (Fig. 41b). On the basis of this observation, one can conclude that plasmon-induced hot carriers are behind the predominant effect that catalyzes NH_3 decomposition.

7. Conclusions and future perspectives

In this review, we summarized the recent advances in the theoretical modeling, experimental realization, and practical applications of the extraordinary optical fields in various
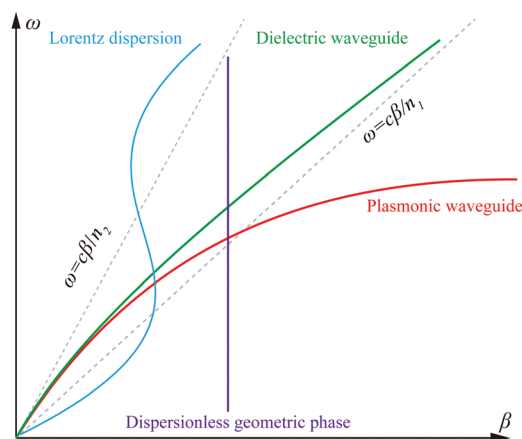

Fig. 42 Four typical dispersion curves in subwavelength-structured optical systems. The red, green, blue, and purple lines correspond to SPPs, dielectric waveguiding modes, Lorentz-type dispersion, and dispersionless geometric phase. Reproduced from ref. 326 with permission. Copyright (2019) Wiley-VCH Verlag.

subwavelength structures. Owing to the unique properties, these subwavelength structures have enabled many funda-mentally new optical applications. Also, they could boost the yield of chemical reactions through different mechanisms, involving photons, phonons, or energetic electrons.

It should be noted that, in most cases, the dispersion diagram is extremely important in the design of subwavelength structures and devices to realize the on-demand extraordinary optical fields. Fig. 42 shows the typical dispersion curves for waves in plasmonic and dielectric waveguides[30,69,152] and Lorentz-type resonant metasurfaces (2D metamaterials),[267,325] as well as in the dispersionless geometric phase.[326–328]

The most conspicuous property of the plasmonic dispersion is the fact that its propagation constant could be much larger than that in the dielectric host, as a result of the collective resonance of the free electrons and photons.[329] This property has led to many practical applications, such as plasmonic nanolithography, ultrathin plasmonic flat lens, and color filtering.[36,37,47,152]

As can be seen in the dispersion curve of the fundamental dielectric waveguiding modes, the propagation constant is limited in a region defined by the refractive index of the core and cladding materials. As a result, the dielectric devices often require a much larger thickness to obtain a particular phase shift than their plasmonic counterparts. Nevertheless, since dielectrics generally have a smaller optical loss in the visible band, dielectric metasurfaces have become a hot topic in recent years.[5,65,330–332] It is noted that the research into subwavelength dielectric optical elements has a venerable history dating back to the 1990s,[333] thus many existing technologies could be utilized in the design of novel optical devices and systems.

Besides the plasmonic and dielectric waveguiding modes, the Lorentz-type dispersion in subwavelength-structured materials has also been intensively studied over the years. Both broadband absorbers and polarization convertors can be designed with Lorentz-type dispersion.[267–269,325,334,335] Since Lorentz dispersion

is used as a basic building block for materials with a complex dispersion obeying the Kramers–Kronig relations,[336] it may be generalized to almost all kinds of metasurfaces. Moreover, by utilizing the catenary dispersion functions, the numerical simulation speed may be greatly increased. For example, the simulation time required for a broadband absorber unit cell has been decreased from more than 5 min to less than 2 s.[337]

The geometric phase induced by polarization conversion can also be plotted in the dispersion diagram. Different from the propagating phase shift, the geometric phase is independent of the working frequency and does not change with the thickness.[58] If we consider the wave in such a structure has an effective propagation constant of β, the dispersion relation will become $\beta = 2\sigma\xi/d$, which is also independent of the frequency. This property is helpful to realize ultrathin phase modulators and the generalized laws of reflection and refraction.[151,153]

Finally, it should be noted that localizing of the optical field at an even smaller scale with higher enhancement is continuously pursued due to its significance in various applications. Besides obtaining a higher resolution in imaging and lithography and more precise photothermal treatment of cancers without harming the surrounding healthy tissues, the nanometer- and sub-nanometer-scale localization of optical fields is also critical for the excitation of a single molecule or single quantum, resulting in detections at the single-molecule level[338–340] and the realization of single-photon sources.[341–344] The plasmonic probe with a very sharp tip is a straight way to construct a "super-hot spot" at a "super-small scale".[345] Tip-enhanced Raman scattering imaging with a spatial resolution of 0.5 nm was demonstrated by dramatically reducing the thermal drift of STM, thereby suppressing the lateral movement of molecules at ultralow temperature.[340] It is worth noting that, the sub-nanometer resolution not only originates from the plasmonic detection architecture, but also includes the role of the inter-action between the architectures and molecules.

Furthermore, benefitting from the newly emerging materials, especially the 2D materials and van der Waals materials,[160,346–348] new mechanisms of the interactions between localized fields and materials have been explored, resulting in a giant perfor-mance enhancement. For instance, a graphene–insulator–metal heterostructure was demonstrated to have a plasmon confinement down to the ultimate limit, i.e., the length scale of one atom.[117] It is foreseeable that further localizing and enhancing the optical field could be realized by combining the new material with extraordinary optical modes in novel nanostructured architectures.[339,349–353]

Conflicts of interest

There are no conflicts to declare.

Acknowledgements

Notes and references

1 X. Luo, *Adv. Mater.*, 2019, **31**, 1804680.
2 X. Luo, D. Tsai, M. Gu and M. Hong, *Adv. Opt. Photonics*, 2018, **10**, 757–842.
3 S. A. Maier, *Plasmonics: fundamentals and applications*, Springer Science & Business Media, 2007.
4 P. R. West, S. Ishii, G. V. Naik, N. K. Emani, V. M. Shalaev and A. Boltasseva, *Laser Photonics Rev.*, 2010, **4**, 795–808.
5 S. Jahani and Z. Jacob, *Nat. Nanotechnol.*, 2016, **11**, 23–36.
6 A. I. Kuznetsov, A. E. Miroshnichenko, M. L. Brongersma, Y. S. Kivshar and B. Luk'yanchuk, *Science*, 2016, **354**, 2472.
7 T. W. Ebbesen, H. J. Lezec, H. F. Ghaemi, T. Thio and P. A. Wolff, *Nature*, 1998, **391**, 667–669.
8 H. A. Bethe, *Phys. Rev.*, 1944, **66**, 163–182.
9 F. van Beijnum, C. Retif, C. B. Smiet, H. Liu, P. Lalanne and M. P. van Exter, *Nature*, 2012, **492**, 411–414.
10 J. B. Jackson and N. J. Halas, *Proc. Natl. Acad. Sci. U. S. A.*, 2004, **101**, 17930–17935.
11 A. J. Haes and R. P. Van Duyne, *Anal. Bioanal. Chem.*, 2004, **379**, 920–930.
12 H. Xu, E. J. Bjerneld, M. Käll and L. Börjesson, *Phys. Rev. Lett.*, 1999, **83**, 4357–4360.
13 J. A. Dieringer, A. D. McFarland, N. C. Shah, D. A. Stuart, A. V. Whitney, C. R. Yonzon, M. A. Young, X. Zhang and R. P. Van Duyne, *Faraday Discuss.*, 2006, **132**, 9–26.
14 T. Chung, S.-Y. Lee, E. Y. Song, H. Chun and B. Lee, *Sensors*, 2011, **11**, 10907–10929.
15 S. Y. Ding, E. M. You, Z. Q. Tian and M. Moskovits, *Chem. Soc. Rev.*, 2017, **46**, 4042–4076.
16 K. L. Wustholz, A.-I. Henry, J. M. McMahon, R. G. Freeman, N. Valley, M. E. Piotti, M. J. Natan, G. C. Schatz and R. P. Van Duyne, *J. Am. Chem. Soc.*, 2010, **132**, 10903–10910.
17 D. M. Schaadt, B. Feng and E. T. Yu, *Appl. Phys. Lett.*, 2005, **86**, 063106.
18 D. Derkacs, S. H. Lim, P. Matheu, W. Mar and E. T. Yu, *Appl. Phys. Lett.*, 2006, **89**, 093103.
19 S. Pillai, K. R. Catchpole, T. Trupke and M. A. Green, *J. Appl. Phys.*, 2007, **101**, 093105.
20 C. Hägglund, S. P. Apell and B. Kasemo, *Nano Lett.*, 2010, **10**, 3135–3141.
21 C. Clavero, *Nat. Photonics*, 2014, **8**, 95.
22 K. Awazu, M. Fujimaki, C. Rockstuhl, J. Tominaga, H. Murakami, Y. Ohki, N. Yoshida and T. Watanabe, *J. Am. Chem. Soc.*, 2008, **130**, 1676–1680.
23 Z. W. Seh, S. Liu, M. Low, Z. Zhang, Z. Lu, A. Mlayah and M.-Y. Han, *Adv. Mater.*, 2012, **24**, 2310–2314.
24 D. Tsukamoto, Y. Shiraishi, Y. Sugano, S. Ichikawa, S. Tanaka and T. Hirai, *J. Am. Chem. Soc.*, 2012, **134**, 6309–6315.
25 J. F. Li, Y. F. Huang, Y. Ding, Z. L. Yang, S. B. Li, X. S. Zhou, F. R. Fan, W. Zhang, Z. Y. Zhou, W. D. Yin, B. Ren, Z. L. Wang and Z. Q. Tian, *Nature*, 2010, **464**, 392–395.

26 J. Lee, M. Tymchenko, C. Argyropoulos, P.-Y. Chen, F. Lu, F. Demmerle, G. Boehm, M.-C. Amann, A. Alu and M. A. Belkin, *Nature*, 2014, **511**, 65–69.

27 A. Alabastri, A. Toma, M. Malerba, F. De Angelis and R. Proietti Zaccaria, *ACS Photonics*, 2015, **2**, 115–120.

28 E. Almeida, G. Shalem and Y. Prior, *Nat. Commun.*, 2016, **7**, 10367.

29 M. Rahmani, G. Leo, I. Brener, A. Zayats, S. Maier, C. De Angelis, H. Tan, V. F. Gili, F. Karouta and R. Oulton, *Opto-Electron. Adv.*, 2018, **1**, 180021.

30 X. Luo and T. Ishihara, *Appl. Phys. Lett.*, 2004, **84**, 4780–4782.

31 H. Shi, X. Luo and C. Du, *Opt. Express*, 2007, **15**, 11321–11327.

32 H. Raether, *Surface plasmons on smooth and rough surfaces and on gratings*, Springer-Verlag, Berlin, 1988.

33 X. Luo and T. Ishihara, *Opt. Express*, 2004, **12**, 3055–3065.

34 M. Pu, Y. Guo, X. Li, X. Ma and X. Luo, *ACS Photonics*, 2018, **5**, 3198–3204.

35 H. F. Schouten, N. Kuzmin, G. Dubois, T. D. Visser, G. Gbur, P. F. A. Alkemade, H. Blok, G. W. 't Hooft, D. Lenstra and E. R. Eliel, *Phys. Rev. Lett.*, 2005, **94**, 053901.

36 R. P. Crease, *Phys. World*, 2002, **15**, 19.

37 T. Xu, Y.-K. Wu, X. Luo and L. J. Guo, *Nat. Commun.*, 2010, **1**, 59.

38 R. Welti, *J. Opt. A: Pure Appl. Opt.*, 2006, **8**, 606.

39 R. Zia and M. L. Brongersma, *Nat. Nanotechnol.*, 2007, **2**, 426.

40 J. B. Pendry, *Phys. Rev. Lett.*, 2000, **85**, 3966–3969.

41 Z. Liu, H. Lee, Y. Xiong, C. Sun and X. Zhang, *Science*, 2007, **315**, 1686.

42 N. Fang, H. Lee, C. Sun and X. Zhang, *Science*, 2005, **308**, 534–537.

43 P. Zijlstra, J. W. M. Chon and M. Gu, *Nature*, 2009, **459**, 410–413.

44 M. Gu, Q. Zhang and S. Lamon, *Nat. Rev. Mater.*, 2016, **1**, 16070.

45 Q. Zhang, Z. Xia, Y.-B. Cheng and M. Gu, *Nat. Commun.*, 2018, **9**, 1183.

46 L. Pan, Y. Park, Y. Xiong, E. Ulin-Avila, Y. Wang, L. Zeng, S. Xiong, J. Rho, C. Sun, D. B. Bogy and X. Zhang, *Sci. Rep.*, 2011, **1**, 175.

47 X. Luo, *Natl. Sci. Rev.*, 2018, **5**, 137–138.

48 A. F. Koenderink, A. Alù and A. Polman, *Science*, 2015, **348**, 516–521.

49 Q. Quan and M. Loncar, *Opt. Express*, 2011, **19**, 18529–18542.

50 Q. Quan, P. B. Deotare and M. Loncar, *Appl. Phys. Lett.*, 2010, **96**, 203102.

51 P. Seidler, K. Lister, U. Drechsler, J. Hofrichter and T. Stöferle, *Opt. Express*, 2013, **21**, 32468–32483.

52 S. Hu, M. Khater, R. Salas-Montiel, E. Kratschmer, S. Engelmann, W. M. J. Green and S. M. Weiss, *Sci. Adv.*, 2018, **4**, eaat2355.

53 B. Shen, R. Polson and R. Menon, *Nat. Commun.*, 2016, **7**, 13126.

54 S. Jahani, S. Kim, J. Atkinson, J. C. Wirth, F. Kalhor, A. A. Noman, W. D. Newman, P. Shekhar, K. Han, V. Van, R. G. DeCorby, L. Chrostowski, M. Qi and Z. Jacob, *Nat. Commun.*, 2018, **9**, 1893.

55 Y. Xu, Y. Fu and H. Chen, *Nat. Rev. Mater.*, 2016, **1**, 16067.

56 X. Li, L. Chen, Y. Li, X. Zhang, M. Pu, Z. Zhao, X. Ma, Y. Wang, M. Hong and X. Luo, *Sci. Adv.*, 2016, **2**, e1601102.

57 G. Cao, X. Gan, H. Lin and B. Jia, *Opto-Electron. Adv.*, 2018, **1**, 180012.

58 X. Luo, *Sci. China: Phys., Mech. Astron.*, 2015, **58**, 594201.

59 T. Xu, C. Wang, C. Du and X. Luo, *Opt. Express*, 2008, **16**, 4753–4759.

60 X. Luo, *Adv. Opt. Mater.*, 2018, **6**, 1701201.

61 X. Luo, *ACS Photonics*, 2018, **5**, 4724–4738.

62 S. Astilean, P. Lalanne, P. Chavel, E. Cambril and H. Launois, *Opt. Lett.*, 1998, **23**, 552–554.

63 P. Lalanne, S. Astilean, P. Chavel, E. Cambril and H. Launois, *Opt. Lett.*, 1998, **23**, 1081–1083.

64 A. Arbabi, Y. Horie, A. J. Ball, M. Bagheri and A. Faraon, *Nat. Commun.*, 2015, **6**, 7069.

65 M. Khorasaninejad, W. T. Chen, R. C. Devlin, J. Oh, A. Y. Zhu and F. Capasso, *Science*, 2016, **352**, 1190.

66 P. R. West, J. L. Stewart, A. V. Kildishev, V. M. Shalaev, V. V. Shkunov, F. Strohkendl, Y. A. Zakharenkov, R. K. Dodds and R. Byren, *Opt. Express*, 2014, **22**, 26212–26221.

67 K. E. Chong, L. Wang, I. Staude, A. R. James, J. Dominguez, S. Liu, G. S. Subramania, M. Decker, D. N. Neshev, I. Brener and Y. S. Kivshar, *ACS Photonics*, 2016, **3**, 514–519.

68 W. T. Chen, A. Y. Zhu, V. Sanjeev, M. Khorasaninejad, Z. Shi, E. Lee and F. Capasso, *Nat. Nanotechnol.*, 2018, **13**, 220–226.

69 S. Wang, P. C. Wu, V.-C. Su, Y.-C. Lai, M.-K. Chen, H. Y. Kuo, B. H. Chen, Y. H. Chen, T.-T. Huang, J.-H. Wang, R.-M. Lin, C.-H. Kuan, T. Li, Z. Wang, S. Zhu and D. P. Tsai, *Nat. Nanotechnol.*, 2018, **13**, 227–232.

70 M. Decker, I. Staude, M. Falkner, J. Dominguez, D. N. Neshev, I. Brener, T. Pertsch and Y. S. Kivshar, *Adv. Opt. Mater.*, 2015, **3**, 813–820.

71 R. H. Ritchie, *Phys. Rev.*, 1957, **106**, 874–881.

72 V. G. Veselago, *Sov. Phys. USPEKHI*, 1968, **10**, 509–514.

73 W. L. Barnes, A. Dereux and T. W. Ebbesen, *Nature*, 2003, **424**, 824–830.

74 S. A. Maier, P. G. Kik, H. A. Atwater, S. Meltzer, E. Harel, B. E. Koel and A. A. G. Requicha, *Nat. Mater.*, 2003, **2**, 229–232.

75 K. A. Willets and R. P. Van Duyne, *Annu. Rev. Phys. Chem.*, 2007, **58**, 267–297.

76 S. Kawata, Y. Inouye and P. Verma, *Nat. Photonics*, 2009, **3**, 388.

77 J. J. Mock, M. Barbic, D. R. Smith, D. A. Schultz and S. Schultz, *J. Chem. Phys.*, 2002, **116**, 6755–6759.

78 Q. Zhao, J. Zhou, F. Zhang and D. Lippens, *Mater. Today*, 2009, **12**, 60–69.

79 G. A. Craig, A. Sarkar, C. H. Woodall, M. A. Hay, K. E. R. Marriott, K. V. Kamenev, S. A. Moggach, E. K. Brechin, S. Parsons, G. Rajaraman and M. Murrie, *Chem. Sci.*, 2018, **9**, 1551–1559.

80 Y. H. Fu, A. I. Kuznetsov, A. E. Miroshnichenko, Y. F. Yu and B. Luk'yanchuk, *Nat. Commun.*, 2013, **4**, 1527.

81 S. Person, M. Jain, Z. Lapin, J. J. Sáenz, G. Wicks and L. Novotny, *Nano Lett.*, 2013, **13**, 1806–1809.

82 M. Kerker, D.-S. Wang and C. L. Giles, *J. Opt. Soc. Am.*, 1983, **73**, 765–767.

83 Z. Chen, A. Taflove and V. Backman, *Opt. Express*, 2004, **12**, 1214–1220.

84 Z. Wang, W. Guo, L. Li, B. Luk'yanchuk, A. Khan, Z. Liu, Z. Chen and M. Hong, *Nat. Commun.*, 2011, **2**, 218.

85 P. Albella, T. Shibanuma and S. A. Maier, *Sci. Rep.*, 2015, **5**, 18322.

86 J. Ye, F. Wen, H. Sobhani, J. B. Lassiter, P. Van Dorpe, P. Nordlander and N. J. Halas, *Nano Lett.*, 2012, **12**, 1660–1667.

87 J. A. Fan, C. Wu, K. Bao, J. Bao, R. Bardhan, N. J. Halas, V. N. Manoharan, P. Nordlander, G. Shvets and F. Capasso, *Science*, 2010, **328**, 1135–1138.

88 Y. Zhang, F. Wen, Y.-R. Zhen, P. Nordlander and N. J. Halas, *Proc. Natl. Acad. Sci. U. S. A.*, 2013, **110**, 9215.

89 R. Shi, Y. Cao, Y. Bao, Y. Zhao, I. N. Waterhouse Geoffrey, Z. Fang, W. Wu, T. Tung, Y. Yin and T. Zhang, *Adv. Mater.*, 2017, **29**, 1700803.

90 E. Prodan, C. Radloff, N. J. Halas and P. Nordlander, *Science*, 2003, **302**, 419–422.

91 B. Averill and P. Eldredge, *Principles of General Chemistry*, 2012.

92 H. Shi, C. Wang, C. Du, X. Luo, X. Dong and H. Gao, *Opt. Express*, 2005, **13**, 6815–6820.

93 Z. Jacob, L. V. Alekseyev and E. Narimanov, *Opt. Express*, 2006, **14**, 8247–8256.

94 M. Pu, X. Ma, Y. Guo, X. Li and X. Luo, *Opt. Express*, 2018, **26**, 19555–19562.

95 Y. Zhang, Y. Luo, Y. Zhang, Y.-J. Yu, Y.-M. Kuang, L. Zhang, Q.-S. Meng, Y. Luo, J.-L. Yang, Z.-C. Dong and J. G. Hou, *Nature*, 2016, **531**, 623.

96 M. Caldarola, P. Albella, E. Cortés, M. Rahmani, T. Roschuk, G. Grinblat, R. F. Oulton, A. V. Bragas and S. A. Maier, *Nat. Commun.*, 2015, **6**, 7915.

97 L. Chuntonov and G. Haran, *Nano Lett.*, 2011, **11**, 2440–2445.

98 H. Lee, G.-H. Kim, J.-H. Lee, N. H. Kim, J.-M. Nam and Y. D. Suh, *Nano Lett.*, 2015, **15**, 4628–4636.

99 N. Zohar, L. Chuntonov and G. Haran, *J. Photochem. Photobiol., C*, 2014, **21**, 26–39.

100 M. Rahmani, D. Y. Lei, V. Giannini, B. Lukiyanchuk, M. Ranjbar, T. Y. F. Liew, M. Hong and S. A. Maier, *Nano Lett.*, 2012, **12**, 2101–2106.

101 S. J. Barrow, X. Wei, J. S. Baldauf, A. M. Funston and P. Mulvaney, *Nat. Commun.*, 2012, **3**, 1275.

102 T. Shibanuma, T. Matsui, T. Roschuk, J. Wojcik, P. Mascher, P. Albella and S. A. Maier, *ACS Photonics*, 2017, **4**, 489–494.

103 E. Khaidarov, H. Hao, R. Paniagua-Domínguez, Y. F. Yu, Y. H. Fu, V. Valuckas, S. L. K. Yap, Y. T. Toh, J. S. K. Ng and A. I. Kuznetsov, *Nano Lett.*, 2017, **17**, 6267–6272.

104 R. Paniagua-Domínguez, Y. F. Yu, E. Khaidarov, S. Choi, V. Leong, R. M. Bakker, X. Liang, Y. H. Fu, V. Valuckas,

L. A. Krivitsky and A. I. Kuznetsov, *Nano Lett.*, 2018, **18**, 2124–2132.

105 M. F. Crommie, C. P. Lutz and D. M. Eigler, *Science*, 1993, **262**, 218.

106 B. N. Taber, C. F. Gervasi, J. M. Mills, D. A. Kislitsyn, E. R. Darzi, W. G. Crowley, R. Jasti and G. V. Nazin, *J. Phys. Chem. Lett.*, 2016, **7**, 3073–3077.

107 K. E. Chong, B. Hopkins, I. Staude, A. E. Miroshnichenko, J. Dominguez, M. Decker, D. N. Neshev, I. Brener and Y. S. Kivshar, *Small*, 2014, **10**, 1985–1990.

108 E. N. Bulgakov and D. N. Maksimov, *Opt. Express*, 2017, **25**, 14134–14147.

109 C. Ciracì, R. T. Hill, J. J. Mock, Y. Urzhumov, A. I. Fernández-Domínguez, S. A. Maier, J. B. Pendry, A. Chilkoti and D. R. Smith, *Science*, 2012, **337**, 1072.

110 A. Moreau, C. Ciraci, J. J. Mock, R. T. Hill, Q. Wang, B. J. Wiley, A. Chilkoti and D. R. Smith, *Nature*, 2012, **492**, 86–89.

111 W. Chen, S. Zhang, Q. Deng and H. Xu, *Nat. Commun.*, 2018, **9**, 801.

112 K. J. Savage, M. M. Hawkeye, R. Esteban, A. G. Borisov, J. Aizpurua and J. J. Baumberg, *Nature*, 2012, **491**, 574.

113 J. Zuloaga, E. Prodan and P. Nordlander, *Nano Lett.*, 2009, **9**, 887–891.

114 W. Zhu, R. Esteban, A. G. Borisov, J. J. Baumberg, P. Nordlander, H. J. Lezec, J. Aizpurua and K. B. Crozier, *Nat. Commun.*, 2016, **7**, 11495.

115 D. Ji, A. Cheney, N. Zhang, H. Song, J. Gao, X. Zeng, H. Cheng, S. Jiang, Z. Yu and Q. Gan, *Adv. Opt. Mater.*, 2017, **5**, 1700223.

116 J. Khurgin, W.-Y. Tsai, D. P. Tsai and G. Sun, *ACS Photonics*, 2017, **4**, 2871–2880.

117 D. Alcaraz Iranzo, S. Nanot, E. J. C. Dias, I. Epstein, C. Peng, D. K. Efetov, M. B. Lundeberg, R. Parret, J. Osmond, J.-Y. Hong, J. Kong, D. R. Englund, N. M. R. Peres and F. H. L. Koppens, *Science*, 2018, **360**, 291.

118 R. Esteban, G. Aguirregabiria, A. G. Borisov, Y. M. Wang, P. Nordlander, G. W. Bryant and J. Aizpurua, *ACS Photonics*, 2015, **2**, 295–305.

119 J. A. Scholl, A. L. Koh and J. A. Dionne, *Nature*, 2012, **483**, 421.

120 E. Abbe, *Arch. Für Mikrosk. Anat.*, 1873, **9**, 413–418.

121 E. H. Synge, *Philos. Mag. J. Sci.*, 1928, **6**, 356–362.

122 E. Betzig, A. Lewis, A. Harootunian, M. Isaacson and E. Kratschmer, *Biophys. J.*, 1986, **49**, 269–279.

123 M. Parzefall and L. Novotny, *ACS Photonics*, 2018, **5**, 4195–4202.

124 C. Gong, M. R. S. Dias, G. C. Wessler, J. A. Taillon, L. G. Salamanca-Riba and M. S. Leite, *Adv. Opt. Mater.*, 2017, **5**, 1600568.

125 B. Pollard, F. C. B. Maia, M. B. Raschke and R. O. Freitas, *Nano Lett.*, 2016, **16**, 55–61.

126 X. Chen, X. Luo, H. Tian and J. Shi, *Chinese Pat.*, ZL03123574.3, 2003.

127 C. Wang, P. Gao, Z. Zhao, N. Yao, Y. Wang, L. Liu, K. Liu and X. Luo, *Opt. Express*, 2013, **21**, 20683–20691.

128 P. Gao, N. Yao, C. Wang, Z. Zhao, Y. Luo, Y. Wang, G. Gao, K. Liu, C. Zhao and X. Luo, *Appl. Phys. Lett.*, 2015, **106**, 093110.

129 A. O. Bak, E. O. Yoxall, P. Sarriugarte, V. Giannini, S. A. Maier, R. Hillenbrand, J. B. Pendry and C. C. Phillips, *Nano Lett.*, 2016, **16**, 1609–1613.

130 W. Wang, H. Xing, L. Fang, Y. Liu, J. Ma, L. Lin, C. Wang and X. Luo, *Opt. Express*, 2008, **16**, 21142–21148.

131 J. Wang, Y. Xu, H. Chen and B. Zhang, *J. Mater. Chem.*, 2012, **22**, 15863–15868.

132 L. Liu, K. Liu, Z. Zhao, C. Wang, P. Gao and X. Luo, *RSC Adv.*, 2016, **6**, 95973–95978.

133 J. Sun, T. Xu and N. M. Litchinitser, *Nano Lett.*, 2016, **16**, 7905–7909.

134 S. Lecler, Y. Takakura and P. Meyrueis, *Opt. Lett.*, 2005, **30**, 2641–2643.

135 A. V. Itagi and W. A. Challener, *J. Opt. Soc. Am. A*, 2005, **22**, 2847.

136 M. X. Wu, B. J. Huang, R. Chen, Y. Yang, J. F. Wu, R. Ji, X. D. Chen and M. H. Hong, *Opt. Express*, 2015, **23**, 20096–20103.

137 M. Wu, R. Chen, J. Soh, Y. Shen, L. Jiao, J. Wu, X. Chen, R. Ji and M. Hong, *Sci. Rep.*, 2016, **6**, 31637.

138 L.-W. Chen, Y. Zhou, M.-X. Wu and M. Hong, *Opto-Electron. Adv.*, 2018, **1**, 170001.

139 D. Gérard, J. Wenger, A. Devilez, D. Gachet, B. Stout, N. Bonod, E. Popov and H. Rigneault, *Opt. Express*, 2008, **16**, 15297.

140 Y. J. Fan, Y. C. Wu, Y. Chen, Y. C. Kung, T. H. Wu, K. W. Huang, H. J. Sheen and P. Y. Chiou, *Biomicrofluidics*, 2013, **7**, 044121.

141 J. J. Schwartz, S. Stavrakis and S. R. Quake, *Nat. Nanotechnol.*, 2010, **5**, 127–132.

142 K. J. Yi, H. Wang, Y. F. Lu and Z. Y. Yang, *J. Appl. Phys.*, 2007, **101**, 063528.

143 I. Alessandri, N. Bontempi and L. E. Depero, *RSC Adv.*, 2014, **4**, 38152.

144 Y. Yan, L. Li, C. Feng, W. Guo, S. Lee and M. Hong, *ACS Nano*, 2014, **8**, 1809–1816.

145 L. Li, W. Guo, Y. Yan, S. Lee and T. Wang, *Light: Sci. Appl.*, 2013, **2**, e104.

146 H. Yang, N. Moullan, J. Auwerx and M. A. M. Gijs, *Small*, 2014, **10**, 1712–1718.

147 B. Yao, M. Lei, L. Ren, N. Menke, Y. Wang, T. Fischer and N. Hampp, *Opt. Lett.*, 2005, **30**, 3060–3062.

148 T. L. Andrew, H.-Y. Tsai and R. Menon, *Science*, 2009, **324**, 917–921.

149 X. Li, Y. Cao, N. Tian, L. Fu and M. Gu, *Optica*, 2015, **2**, 567–570.

150 J. Jin, X. Zhang, P. Gao, J. Luo, Z. Zhang, X. Li, X. Ma, M. Pu and L. Xiangang, *Ann. Phys.*, 2017, **530**, 1700326.

151 N. Yu, P. Genevet, M. A. Kats, F. Aieta, J.-P. Tetienne, F. Capasso and Z. Gaburro, *Science*, 2011, **334**, 333–337.

152 L. Verslegers, P. B. Catrysse, Z. Yu, J. S. White, E. S. Barnard, M. L. Brongersma and S. Fan, *Nano Lett.*, 2009, **9**, 235–238.

153 M. Pu, X. Li, X. Ma, Y. Wang, Z. Zhao, C. Wang, C. Hu, P. Gao, C. Huang, H. Ren, X. Li, F. Qin, J. Yang, M. Gu, M. Hong and X. Luo, *Sci. Adv.*, 2015, **1**, e1500396.

154 F. Zhang, M. Pu, X. Li, P. Gao, X. Ma, J. Luo, H. Yu and X. Luo, *Adv. Funct. Mater.*, 2017, **27**, 1704295.

155 X. Xie, X. Li, M. Pu, X. Ma, K. Liu, Y. Guo and X. Luo, *Adv. Funct. Mater.*, 2018, **28**, 1706673.

156 Y. Guo, M. Pu, Z. Zhao, Y. Wang, J. Jin, P. Gao, X. Li, X. Ma and X. Luo, *ACS Photonics*, 2016, **3**, 2022–2029.

157 F. Ding, A. Pors and S. I. Bozhevolnyi, *Rep. Prog. Phys.*, 2018, **81**, 026401.

158 T. Xu, C. Du, C. Wang and X. Luo, *Appl. Phys. Lett.*, 2007, **91**, 201501.

159 S. Ishii, V. M. Shalaev and A. V. Kildishev, *Nano Lett.*, 2013, **13**, 159–163.

160 Y. Chen, C. Zhou, X. Luo and C. Du, *Opt. Lett.*, 2008, **33**, 753–755.

161 M. Pu, X. Li, Y. Guo, X. Ma and X. Luo, *Opt. Express*, 2017, **25**, 31471–31477.

162 C. Min, P. Wang, X. Jiao, Y. Deng and H. Ming, *Opt. Express*, 2007, **15**, 9541–9546.

163 Y. Chen, X. Li, Y. Sonnefraud, A. I. Fernández-Domínguez, X. Luo, M. Hong and S. A. Maier, *Sci. Rep.*, 2015, **5**, 8660.

164 N. Raeis-Hosseini and J. Rho, *Materials*, 2017, **10**, 1046.

165 J. R. Lakowicz, J. Malicka, I. Gryczynski and Z. Gryczynski, *Biochem. Biophys. Res. Commun.*, 2003, **307**, 435–439.

166 J. R. Lakowicz, *Anal. Biochem.*, 2004, **324**, 153–169.

167 R. Badugu, E. Descrovi and J. R. Lakowicz, *Anal. Biochem.*, 2014, **445**, 1–13.

168 Y. Chen, D. Zhang, D. Qiu, L. Zhu, S. Yu, P. Yao, P. Wang, H. Ming, R. Badugu and J. R. Lakowicz, *Laser Photonics Rev.*, 2014, **8**, 933–940.

169 H. Aouani, O. Mahboub, E. Devaux, H. Rigneault, T. W. Ebbesen and J. Wenger, *Nano Lett.*, 2011, **11**, 2400–2406.

170 H. J. Lezec, A. Degiron, E. Devaux, R. A. Linke, L. Martin-Moreno, F. J. Garcia-Vidal and T. W. Ebbesen, *Science*, 2002, **297**, 820–822.

171 H. Aouani, O. Mahboub, N. Bonod, E. Devaux, E. Popov, H. Rigneault, T. W. Ebbesen and J. Wenger, *Nano Lett.*, 2011, **11**, 637–644.

172 Y. C. Jun, K. C. Y. Huang and M. L. Brongersma, *Nat. Commun.*, 2011, **2**, 283.

173 T. H. Taminiau, F. D. Stefani, F. B. Segerink and N. F. van Hulst, *Nat. Photonics*, 2008, **2**, 234.

174 T. Kosako, Y. Kadoya and H. F. Hofmann, *Nat. Photonics*, 2010, **4**, 312–315.

175 A. G. Curto, G. Volpe, T. H. Taminiau, M. P. Kreuzer, R. Quidant and N. F. van Hulst, *Science*, 2010, **329**, 930–933.

176 A. Kristensen, J. K. W. Yang, S. I. Bozhevolnyi, S. Link, P. Nordlander, N. J. Halas and N. A. Mortensen, *Nat. Rev. Mater.*, 2016, **2**, 16088.

177 M. Keshavarz Hedayati and M. Elbahri, *Plasmonics*, 2017, **12**, 1463–1479.

178 C. Genet and T. W. Ebbesen, *Nature*, 2007, **445**, 39–46.

179 E. Laux, C. Genet, T. Skauli and T. W. Ebbesen, *Nat. Photonics*, 2008, **2**, 161–164.

180 K. Kumar, H. Duan, R. S. Hegde, S. C. W. Koh, J. N. Wei and J. K. W. Yang, *Nat. Nanotechnol.*, 2012, **7**, 557.

181 F. Cheng, J. Gao, T. S. Luk and X. Yang, *Sci. Rep.*, 2015, **5**, 11045.

182 X. M. Goh, Y. Zheng, S. J. Tan, L. Zhang, K. Kumar, C.-W. Qiu and J. K. W. Yang, *Nat. Commun.*, 2014, **5**, 5361.

183 J. Xue, Z.-K. Zhou, Z. Wei, R. Su, J. Lai, J. Li, C. Li, T. Zhang and X.-H. Wang, *Nat. Commun.*, 2015, **6**, 8906.

184 T. D. James, P. Mulvaney and A. Roberts, *Nano Lett.*, 2016, **16**, 3817–3823.

185 M. Miyata, H. Hatada and J. Takahara, *Nano Lett.*, 2016, **16**, 3166–3172.

186 Z. Yang, Y. Zhou, Y. Chen, Y. Wang, P. Dai, Z. Zhang and H. Duan, *Adv. Opt. Mater.*, 2016, **4**, 1196–1202.

187 W. Yue, S. Gao, S.-S. Lee, E.-S. Kim and D.-Y. Choi, *Sci. Rep.*, 2016, **6**, 29756.

188 W. Yue, S. Gao, S.-S. Lee, E.-S. Kim and D.-Y. Choi, *Laser Photonics Rev.*, 2017, **11**, 1600285.

189 C. Hu, Z. Zhao, X. Chen and X. Luo, *Opt. Express*, 2009, **17**, 11039–11044.

190 Y. J. Liu, G. Y. Si, E. S. Leong, N. Xiang, A. J. Danner and J. H. Teng, *Adv. Mater.*, 2012, **24**, OP131–OP135.

191 S. Song, X. Ma, M. Pu, X. Li, K. Liu, P. Gao, Z. Zhao, Y. Wang, C. Wang and X. Luo, *Adv. Opt. Mater.*, 2017, **5**, 1600829.

192 X. Duan, S. Kamin and N. Liu, *Nat. Commun.*, 2017, **8**, 14606.

193 D. Franklin, Y. Chen, A. Vazquez-Guardado, S. Modak, J. Boroumand, D. Xu, S.-T. Wu and D. Chanda, *Nat. Commun.*, 2015, **6**, 7337.

194 T. Xu, E. C. Walter, A. Agrawal, C. Bohn, J. Velmurugan, W. Zhu, H. J. Lezec and A. A. Talin, *Nat. Commun.*, 2016, **7**, 10479.

195 C. Höppener and L. Novotny, *Q. Rev. Biophys.*, 2012, **45**, 209–255.

196 D. L. Jeanmaire and R. P. Van Duyne, *J. Electroanal. Chem. Interfacial Electrochem.*, 1977, **84**, 1–20.

197 K. Saha, S. S. Agasti, C. Kim, X. Li and V. M. Rotello, *Chem. Rev.*, 2012, **112**, 2739–2779.

198 J. Homola, *Chem. Rev.*, 2008, **108**, 462–493.

199 M. E. Stewart, C. R. Anderton, L. B. Thompson, J. Maria, S. K. Gray, J. A. Rogers and R. G. Nuzzo, *Chem. Rev.*, 2008, **108**, 494–521.

200 L. J. Sherry, R. Jin, C. A. Mirkin, G. C. Schatz and R. P. Van Duyne, *Nano Lett.*, 2006, **6**, 2060–2065.

201 N. Verellen, P. Van Dorpe, D. Vercruysse, G. A. E. Vandenbosch and V. V. Moshchalkov, *Opt. Express*, 2011, **19**, 11034–11051.

202 Z. Liao, Y. Luo, A. I. Fernández-Domínguez, X. Shen, S. A. Maier and T. J. Cui, *Sci. Rep.*, 2015, **5**, 9590.

203 A. Kinkhabwala, Z. Yu, S. Fan, Y. Avlasevich, K. Müllen and W. E. Moerner, *Nat. Photonics*, 2009, **3**, 654.

204 A. V. Kabashin, P. Evans, S. Pastkovsky, W. Hendren, G. A. Wurtz, R. Atkinson, R. Pollard, V. A. Podolskiy and A. V. Zayats, *Nat. Mater.*, 2009, **8**, 867–871.

205 A. E. Cetin and H. Altug, *ACS Nano*, 2012, **6**, 9989–9995.

206 H.-H. Jeong, A. G. Mark, M. Alarcón-Correa, I. Kim, P. Oswald, T.-C. Lee and P. Fischer, *Nat. Commun.*, 2016, **7**, 11331.

207 M. Mesch, B. Metzger, M. Hentschel and H. Giessen, *Nano Lett.*, 2016, **16**, 3155–3159.

208 D. Rodrigo, O. Limaj, D. Janner, D. Etezadi, F. J. García de Abajo, V. Pruneri and H. Altug, *Science*, 2015, **349**, 165.

209 A. E. Cetin, A. F. Coskun, B. C. Galarreta, M. Huang, D. Herman, A. Ozcan and H. Altug, *Light: Sci. Appl.*, 2014, **3**, e122.

210 N. Liu, M. L. Tang, M. Hentschel, H. Giessen and A. P. Alivisatos, *Nat. Mater.*, 2011, **10**, 631.

211 T. Srivastava and R. Jha, *IEEE Photonics Technol. Lett.*, 2018, **30**, 319–322.

212 M. Moskovits, *J. Chem. Phys.*, 1978, **69**, 4159–4161.

213 S. Nie and S. R. Emory, *Science*, 1997, **275**, 1102.

214 E. S. Grabbe and R. P. Buck, *J. Am. Chem. Soc.*, 1989, **111**, 8362–8366.

215 G. Baker and D. Moore, *Anal. Bioanal. Chem.*, 2005, **382**, 1751–1770.

216 K. Kelly, E. Coronado, L. Zhao and G. Schatz, *J. Phys. Chem. B*, 2003, **107**, 668–677.

217 M. Fleischmann, P. J. Hendra and A. J. McQuillan, *Chem. Phys. Lett.*, 1974, **26**, 163–166.

218 K. Kneipp, Y. Wang, H. Kneipp, L. T. Perelman, I. Itzkan, R. R. Dasari and M. S. Feld, *Phys. Rev. Lett.*, 1997, **78**, 1667–1670.

219 V. M. Shalaev and A. K. Sarychev, *Phys. Rev. B: Condens. Matter Mater. Phys.*, 1998, **57**, 13265–13288.

220 H. M. Lee, S. M. Jin, H. M. Kim and Y. D. Suh, *Phys. Chem. Chem. Phys.*, 2013, **15**, 5276–5287.

221 J.-M. Nam, J.-W. Oh, H. Lee and Y. D. Suh, *Acc. Chem. Res.*, 2016, **49**, 2746–2755.

222 Z.-Q. Tian, B. Ren and D.-Y. Wu, *J. Phys. Chem. B*, 2002, **106**, 9463–9483.

223 Y. Wang and S. Schlücker, *Analyst*, 2013, **138**, 2224–2238.

224 W. Zhang, J. Liu, W. Niu, H. Yan, X. Lu and B. Liu, *ACS Appl. Mater. Interfaces*, 2018, **10**, 14850–14856.

225 T. Yang, X. Guo, Y. Wu, H. Wang, S. Fu, Y. Wen and H. Yang, *ACS Appl. Mater. Interfaces*, 2014, **6**, 20985–20993.

226 J. F. Li, Y. F. Huang, Y. Ding, Z. L. Yang, S. B. Li, X. S. Zhou, F. R. Fan, W. Zhang, Z. Y. Zhou, D. Y. Wu, B. Ren, Z. L. Wang and Z. Q. Tian, *Nature*, 2010, **464**, 392–395.

227 S.-Y. Ding, J. Yi, J.-F. Li, B. Ren, D.-Y. Wu, R. Panneerselvam and Z.-Q. Tian, *Nat. Rev. Mater.*, 2016, **1**, 16021.

228 D. Xu, F. Teng, Z. Wang and N. Lu, *ACS Appl. Mater. Interfaces*, 2017, **9**, 21548–21553.

229 C. Zhu, G. Meng, P. Zheng, Q. Huang, Z. Li, X. Hu, X. Wang, Z. Huang, F. Li and N. Wu, *Adv. Mater.*, 2016, **28**, 4871–4876.

230 K. Xu, Z. Wang, C. F. Tan, N. Kang, L. Chen, L. Ren, E. S. Thian, G. W. Ho, R. Ji and M. Hong, *ACS Appl. Mater. Interfaces*, 2017, **9**, 26341–26349.

231 S. Sanchez-Cortes, C. Domingo, J. V. Garcia-Ramos and J. A. Aznarez, *Langmuir*, 2001, **17**, 1157–1162.

232 A. Hakonen, P. O. Andersson, M. S. Schmidt, T. Rindzevicius and M. Käll, *Anal. Chim. Acta*, 2015, **893**, 1–13.

233 L. A. Lane, X. Qian and S. Nie, *Chem. Rev.*, 2015, **115**, 10489–10529.

234 L.-J. Xu, C. Zong, X.-S. Zheng, P. Hu, J.-M. Feng and B. Ren, *Anal. Chem.*, 2014, **86**, 2238–2245.

235 L. Guerrini, Ž. Krpetić, D. van Lierop, R. A. Alvarez-Puebla and D. Graham, *Angew. Chem.*, 2015, **127**, 1160–1164.

236 W. L. Barnes, *J. Mod. Opt.*, 1998, **45**, 661–699.

237 E. Fort and S. Grésillon, *J. Phys. D: Appl. Phys.*, 2008, **41**, 013001.

238 J. A. Schuller, E. S. Barnard, W. Cai, Y. C. Jun, J. S. White and M. L. Brongersma, *Nat. Mater.*, 2010, **9**, 193.

239 S. Khatua, P. M. R. Paulo, H. Yuan, A. Gupta, P. Zijlstra and M. Orrit, *ACS Nano*, 2014, **8**, 4440–4449.

240 Z. Wang, Z. Dong, Y. Gu, Y.-H. Chang, L. Zhang, L.-J. Li, W. Zhao, G. Eda, W. Zhang, G. Grinblat, S. A. Maier, J. K. W. Yang, C.-W. Qiu and A. T. S. Wee, *Nat. Commun.*, 2016, **7**, 11283.

241 R. Regmi, J. Berthelot, P. M. Winkler, M. Mivelle, J. Proust, F. Bedu, I. Ozerov, T. Begou, J. Lumeau, H. Rigneault, M. F. García-Parajó, S. Bidault, J. Wenger and N. Bonod, *Nano Lett.*, 2016, **16**, 5143–5151.

242 E. Tiguntseva, A. Chebykin, A. Ishteev, R. Haroldson, B. Balachandran, E. Ushakova, F. Komissarenko, H. Wang, V. Milichko, A. Tsypkin, D. Zuev, W. Hu, S. Makarov and A. Zakhidov, *Nanoscale*, 2017, **9**, 12486–12493.

243 F. Neubrech, C. Huck, K. Weber, A. Pucci and H. Giessen, *Chem. Rev.*, 2017, **117**, 5110–5145.

244 G. Biener, A. Niv, V. Kleiner and E. Hasman, *Opt. Lett.*, 2007, **32**, 994–996.

245 F. Le, D. W. Brandl, Y. A. Urzhumov, H. Wang, J. Kundu, N. J. Halas, J. Aizpurua and P. Nordlander, *ACS Nano*, 2008, **2**, 707–718.

246 K. Weber, M. L. Nesterov, T. Weiss, M. Scherer, M. Hentschel, J. Vogt, C. Huck, W. Li, M. Dressel, H. Giessen and F. Neubrech, *ACS Photonics*, 2017, **4**, 45–51.

247 A. E. Miroshnichenko, S. Flach and Y. S. Kivshar, *Rev. Mod. Phys.*, 2010, **82**, 2257–2298.

248 C. Wu, A. B. Khanikaev, R. Adato, N. Arju, A. A. Yanik, H. Altug and G. Shvets, *Nat. Mater.*, 2012, **11**, 69–75.

249 C. Huck, J. Vogt, M. Sendner, D. Hengstler, F. Neubrech and A. Pucci, *ACS Photonics*, 2015, **2**, 1489–1497.

250 E. Cubukcu, S. Zhang, Y.-S. Park, G. Bartal and X. Zhang, *Appl. Phys. Lett.*, 2009, **95**, 043113.

251 L. V. Brown, X. Yang, K. Zhao, B. Y. Zheng, P. Nordlander and N. J. Halas, *Nano Lett.*, 2015, **15**, 1272–1280.

252 L. Dong, X. Yang, C. Zhang, B. Cerjan, L. Zhou, M. L. Tseng, Y. Zhang, A. Alabastri, P. Nordlander and N. J. Halas, *Nano Lett.*, 2017, **17**, 5768–5774.

253 A. E. Cetin, D. Etezadi and A. Hatice, *Adv. Opt. Mater.*, 2014, **2**, 866–872.

254 K. Chen, R. Adato and H. Altug, *ACS Nano*, 2012, **6**, 7998–8006.

255 H. Aouani, H. Šípová, M. Rahmani, M. Navarro-Cia, K. Hegnerová, J. Homola, M. Hong and S. A. Maier, *ACS Nano*, 2012, **7**, 669–675.

256 H. Hu, X. Yang, F. Zhai, D. Hu, R. Liu, K. Liu, Z. Sun and Q. Dai, *Nat. Commun.*, 2016, **7**, 12334.

257 B. Guillaume and Q. Romain, *Laser Photonics Rev.*, 2012, **7**, 171–187.

258 J. R. Cole, N. A. Mirin, M. W. Knight, G. P. Goodrich and N. J. Halas, *J. Phys. Chem. C*, 2009, **113**, 12090–12094.

259 K. Yang, J. Wan, S. Zhang, B. Tian, Y. Zhang and Z. Liu, *Biomaterials*, 2012, **33**, 2206–2214.

260 D. F. Ollis and H. Al-Ekabi, *Photocatalytic Purification and Treatment of Water and Air: Proceedings of the 1st International Conference on TiO$_2$ Photocatalytic Purification and Treatment of Water and Air, London, Ontario, Canada, 8-13 November, 1992,* Elsevier Science Ltd, 1993.

261 K. Hashimoto, H. Irie and A. Fujishima, *Jpn. J. Appl. Phys.*, 2005, **44**, 8269–8285.

262 M. R. Hoffmann, S. T. Martin, W. Choi and D. W. Bahnemann, *Chem. Rev.*, 1995, **95**, 69–96.

263 J.-M. Herrmann, *Catal. Today*, 1999, **53**, 115–129.

264 N. I. Landy, S. Sajuyigbe, J. J. Mock, D. R. Smith and W. J. Padilla, *Phys. Rev. Lett.*, 2008, **100**, 207402.

265 M. Pu, C. Hu, M. Wang, C. Huang, Z. Zhao, C. Wang, Q. Feng and X. Luo, *Opt. Express*, 2011, **19**, 17413–17420.

266 Y. Cui, K. H. Fung, J. Xu, H. Ma, Y. Jin, S. He and N. X. Fang, *Nano Lett.*, 2012, **12**, 1443–1447.

267 Q. Feng, M. Pu, C. Hu and X. Luo, *Opt. Lett.*, 2012, **37**, 2133–2135.

268 N. K. Grady, J. E. Heyes, D. R. Chowdhury, Y. Zeng, M. T. Reiten, A. K. Azad, A. J. Taylor, D. A. R. Dalvit and H.-T. Chen, *Science*, 2013, **340**, 1304–1307.

269 Y. Guo, Y. Wang, M. Pu, Z. Zhao, X. Wu, X. Ma, C. Wang, L. Yan and X. Luo, *Sci. Rep.*, 2015, **5**, 8434.

270 M. Pu, M. Wang, C. Hu, C. Huang, Z. Zhao, Y. Wang and X. Luo, *Opt. Express*, 2012, **20**, 25513–25519.

271 S. Yin, J. Zhu, W. Xu, W. Jiang, J. Yuan, G. Yin, L. Xie, Y. Ying and Y. Ma, *Appl. Phys. Lett.*, 2015, **107**, 073903.

272 X. Zang, C. Shi, L. Chen, B. Cai, Y. Zhu and S. Zhuang, *Sci. Rep.*, 2015, **5**, 8091.

273 M. R. S. Dias, C. Gong, Z. A. Benson and M. S. Leite, *Adv. Opt. Mater.*, 2018, **6**, 1700830.

274 J. Hao, L. Zhou and M. Qiu, *Phys. Rev. B: Condens. Matter Mater. Phys.*, 2011, **83**, 165107.

275 W. Li, U. Guler, N. Kinsey, G. V. Naik, A. Boltasseva, J. Guan, V. M. Shalaev and A. V. Kildishev, *Adv. Mater.*, 2014, **26**, 7959–7965.

276 Y. Huang, L. Liu, M. Pu, X. Li, X. Ma and X. Luo, *Nanoscale*, 2018, **10**, 8298–8303.

277 L. Zhou, Y. Tan, D. Ji, B. Zhu, P. Zhang, J. Xu, Q. Gan, Z. Yu and J. Zhu, *Sci. Adv.*, 2016, **2**, e1501227.

278 N. J. Hogan, A. S. Urban, C. Ayala-Orozco, A. Pimpinelli, P. Nordlander and N. J. Halas, *Nano Lett.*, 2014, **14**, 4640–4645.

279 H. Maeda, J. Wu, T. Sawa, Y. Matsumura and K. Hori, *J. Controlled Release*, 2000, **65**, 271–284.

280 J. L. West and N. J. Halas, *Annu. Rev. Biomed. Eng.*, 2003, **5**, 285–292.

281 X. Huang, P. K. Jain, I. H. El-Sayed and M. A. El-Sayed, *Lasers Med. Sci.*, 2007, **23**, 217.

282 L. M. Maestro, P. Haro-González, M. C. Iglesias-dela Cruz, F. SanzRodríguez, Á. Juarranz, J. G. Solé and D. Jaque, *Nanomedicine*, 2012, **8**, 379–388.

283 L. R. Hirsch, R. J. Stafford, J. A. Bankson, S. R. Sershen, B. Rivera, R. E. Price, J. D. Hazle, N. J. Halas and J. L. West, *Proc. Natl. Acad. Sci. U. S. A.*, 2003, **100**, 13549–13554.

284 X. Huang, I. H. El-Sayed, W. Qian and M. A. El-Sayed, *J. Am. Chem. Soc.*, 2006, **128**, 2115–2120.

285 H. Chatterjee, D. S. Rahman, M. Sengupta and S. K. Ghosh, *J. Phys. Chem. C*, 2018, **122**, 13082–13094.

286 N. W. S. Kam, M. O'Connell, J. A. Wisdom and H. Dai, *Proc. Natl. Acad. Sci. U. S. A.*, 2005, **102**, 11600–11605.

287 S. Ghosh, S. Dutta, E. Gomes, D. Carroll, R. D'Agostino, J. Olson, M. Guthold and W. H. Gmeiner, *ACS Nano*, 2009, **3**, 2667–2673.

288 K. Yang, S. Zhang, G. Zhang, X. Sun, S.-T. Lee and Z. Liu, *Nano Lett.*, 2010, **10**, 3318–3323.

289 J. T. Robinson, S. M. Tabakman, Y. Liang, H. Wang, H. Sanchez Casalongue, D. Vinh and H. Dai, *J. Am. Chem. Soc.*, 2011, **133**, 6825–6831.

290 C. Loo, A. Lin, L. Hirsch, M.-H. Lee, J. Barton, N. Halas, J. West and R. Drezek, *Technol. Cancer Res. Treat.*, 2004, **3**, 33–40.

291 C. Ayala-Orozco, C. Urban, M. W. Knight, A. S. Urban, O. Neumann, S. W. Bishnoi, S. Mukherjee, A. M. Goodman, H. Charron, T. Mitchell, M. Shea, R. Roy, S. Nanda, R. Schiff, N. J. Halas and A. Joshi, *ACS Nano*, 2014, **8**, 6372–6381.

292 M. R. K. Ali, M. A. Rahman, Y. Wu, T. Han, X. Peng, M. A. Mackey, D. Wang, H. J. Shin, Z. G. Chen, H. Xiao, R. Wu, Y. Tang, D. M. Shin and M. A. El-Sayed, *Proc. Natl. Acad. Sci. U. S. A.*, 2017, **114**, E3110–E3118.

293 M. S. Yavuz, Y. Cheng, J. Chen, C. M. Cobley, Q. Zhang, M. Rycenga, J. Xie, C. Kim, K. H. Song, A. G. Schwartz, L. V. Wang and Y. Xia, *Nat. Mater.*, 2009, **8**, 935.

294 S. Wang, P. Huang, L. Nie, R. Xing, D. Liu, Z. Wang, J. Lin, S. Chen, G. Niu, G. Lu and X. Chen, *Adv. Mater.*, 2013, **25**, 3055–3061.

295 A. M. Smith, M. C. Mancini and S. Nie, *Nat. Nanotechnol.*, 2009, **4**, 710.

296 H. A. Atwater and A. Polman, *Nat. Mater.*, 2010, **9**, 205.

297 Y. A. Akimov, W. S. Koh, S. Y. Sian and S. Ren, *Appl. Phys. Lett.*, 2010, **96**, 073111.

298 M. S. Branham, W.-C. Hsu, S. Yerci, J. Loomis, S. V. Boriskina, B. R. Hoard, S. E. Han and G. Chen, *Adv. Mater.*, 2015, **27**, 2182–2188.

299 D. Ha, C. Gong, M. S. Leite and J. N. Munday, *ACS Appl. Mater. Interfaces*, 2016, **8**, 24536–24542.

300 M.-G. Kang, T. Xu, H. J. Park, X. Luo and L. J. Guo, *Adv. Mater.*, 2010, **22**, 4378.

301 A. Raman, Z. Yu and S. Fan, *Opt. Express*, 2011, **19**, 19015–19026.

302 K. Q. Le, A. Abass, B. Maes, P. Bienstman and A. Alù, *Opt. Express*, 2012, **20**, A39–A50.

303 A. Lenert, D. M. Bierman, Y. Nam, W. R. Chan, I. Celanovic, M. Soljacic and E. N. Wang, *Nat. Nanotechnol.*, 2014, **9**, 126–130.

304 M. W. Knight, H. Sobhani, P. Nordlander and N. J. Halas, *Science*, 2011, **332**, 702.

305 A. Sobhani, M. W. Knight, Y. Wang, B. Zheng, N. S. King, L. V. Brown, Z. Fang, P. Nordlander and N. J. Halas, *Nat. Commun.*, 2013, **4**, 1643.

306 Y. Liu, R. Cheng, L. Liao, H. Zhou, J. Bai, G. Liu, L. Liu, Y. Huang and X. Duan, *Nat. Commun.*, 2011, **2**, 579.

307 F. H. L. Koppens, T. Mueller, P. Avouris, A. C. Ferrari, M. S. Vitiello and M. Polini, *Nat. Nanotechnol.*, 2014, **9**, 780.

308 J. Tong, W. Zhou, Y. Qu, Z. Xu, Z. Huang and D. H. Zhang, *Nat. Commun.*, 2017, **8**, 1660.

309 F. Bonaccorso, Z. Sun, T. Hasan and A. C. Ferrari, *Nat. Photonics*, 2010, **4**, 611–622.

310 X. Gan, K. F. Mak, Y. Gao, Y. You, F. Hatami, J. Hone, T. F. Heinz and D. Englund, *Nano Lett.*, 2012, **12**, 5626–5631.

311 X. Gan, R.-J. Shiue, Y. Gao, I. Meric, T. F. Heinz, K. Shepard, J. Hone, S. Assefa and D. Englund, *Nat. Photonics*, 2013, **7**, 883–887.

312 X. Zhang, Y. L. Chen, R. S. Liu and D. P. Tsai, *Rep. Prog. Phys.*, 2013, **76**, 046401.

313 G. T. Forcherio, D. R. Baker, J. Boltersdorf, A. C. Leff, J. P. McClure, K. N. Grew and C. A. Lundgren, *J. Phys. Chem. C*, 2018, **122**, 28901–28909.

314 H. Ali and N. R. Jana, *Photochem. Photobiol. Sci.*, 2018, **17**, 628–637.

315 C. Boerigter, U. Aslam and S. Linic, *ACS Nano*, 2016, **10**, 6108–6115.

316 T. Bora, D. Zoepfl and J. Dutta, *Sci. Rep.*, 2016, **6**, 26913.

317 F. Dong, T. Xiong, S. Yan, H. Wang, Y. Sun, Y. Zhang, H. Huang and Z. Wu, *J. Catal.*, 2016, **344**, 401–410.

318 Y. Kim, D. Dumett Torres and P. K. Jain, *Nano Lett.*, 2016, **16**, 3399–3407.

319 S. Linic, U. Aslam, C. Boerigter and M. Morabito, *Nat. Mater.*, 2015, **14**, 567–576.

320 R. Long, Y. Li, L. Song and Y. Xiong, *Small*, 2015, **11**, 3873–3889.

321 C. Wang and D. Astruc, *Chem. Soc. Rev.*, 2014, **43**, 7188–7216.

322 X.-J. Chen, G. Cabello, D.-Y. Wu and Z.-Q. Tian, *J. Photochem. Photobiol., C*, 2014, **21**, 54–80.

323 S. Linic, P. Christopher and D. B. Ingram, *Nat. Mater.*, 2011, **10**, 911–921.

324 L. Zhou, D. F. Swearer, C. Zhang, H. Robatjazi, H. Zhao, L. Henderson, L. Dong, P. Christopher, E. A. Carter, P. Nordlander and N. J. Halas, *Science*, 2018, **362**, 69.

325 M. Pu, P. Chen, Y. Wang, Z. Zhao, C. Huang, C. Wang, X. Ma and X. Luo, *Appl. Phys. Lett.*, 2013, **102**, 131906.

326 M. Pu, Y. Guo, X. Ma, X. Li and X. Luo, *Adv. Opt. Mater.*, 2019, 1801376.

327 X. Luo, M. Pu, X. Li and X. Ma, *Light: Sci. Appl.*, 2017, **6**, e16276.

328 K. Y. Bliokh, F. J. Rodriguez-Fortuno, F. Nori and A. V. Zayats, *Nat. Photonics*, 2015, **9**, 796–808.

329 H. A. Atwater, *Sci. Am.*, 2007, **296**, 56–62.

330 D. Lin, P. Fan, E. Hasman and M. L. Brongersma, *Science*, 2014, **345**, 298–302.

331 A. Arbabi, Y. Horie, M. Bagheri and A. Faraon, *Nat. Nanotechnol.*, 2015, **10**, 937–943.

332 A. I. Kuznetsov, A. E. Miroshnichenko, M. L. Brongersma, Y. S. Kivshar and B. Luk'yanchuk, *Science*, 2016, **354**, aag2472.

333 P. Lalanne and P. Chavel, *Laser Photonics Rev.*, 2017, **11**, 1600295.

334 D. Ye, Z. Wang, K. Xu, H. Li, J. Huangfu, Z. Wang and L. Ran, *Phys. Rev. Lett.*, 2013, **111**, 187402.

335 M. Zhang, F. Zhang, Y. Ou, J. Cai and H. Yu, *Nanophotonics*, 2019, **8**, 117–125.

336 C. A. Dirdal and J. Skaar, *Phys. Rev. A: At., Mol., Opt. Phys.*, 2013, **88**, 033834.

337 Y. Huang, J. Luo, M. Pu, Y. Guo, Z. Zhao, X. Ma, X. Li and X. Luo, *Adv. Sci.*, 2019, 1801691.

338 K. Trofymchuk, A. Reisch, P. Didier, F. Fras, P. Gilliot, Y. Mely and A. S. Klymchenko, *Nat. Photonics*, 2017, **11**, 657–663.

339 R. Chikkaraddy, B. de Nijs, F. Benz, S. J. Barrow, O. A. Scherman, E. Rosta, A. Demetriadou, P. Fox, O. Hess and J. J. Baumberg, *Nature*, 2016, **535**, 127.

340 R. Zhang, Y. Zhang, Z. C. Dong, S. Jiang, C. Zhang, L. G. Chen, L. Zhang, Y. Liao, J. Aizpurua, Y. Luo, J. L. Yang and J. G. Hou, *Nature*, 2013, **498**, 82–86.

341 S. Kako, C. Santori, K. Hoshino, S. Götzinger, Y. Yamamoto and Y. Arakawa, *Nat. Mater.*, 2006, **5**, 887.

342 T. M. Babinec, B. J. M. Hausmann, M. Khan, Y. Zhang, J. R. Maze, P. R. Hemmer and M. Lončar, *Nat. Nanotechnol.*, 2010, **5**, 195.

343 Y.-M. He, Y. He, Y.-J. Wei, D. Wu, M. Atatüre, C. Schneider, S. Höfling, M. Kamp, C.-Y. Lu and J.-W. Pan, *Nat. Nanotechnol.*, 2013, **8**, 213.

344 J. Claudon, J. Bleuse, N. S. Malik, M. Bazin, P. Jaffrennou, N. Gregersen, C. Sauvan, P. Lalanne and J.-M. Gérard, *Nat. Photonics*, 2010, **4**, 174.

345 F. Lu, W. Zhang, L. Huang, S. Liang, D. Mao, F. Gao, T. Mei and J. Zhao, *Opto-Electron. Adv.*, 2018, **1**, 180010.

346 G. X. Ni, A. S. McLeod, Z. Sun, L. Wang, L. Xiong, K. W. Post, S. S. Sunku, B.-Y. Jiang, J. Hone, C. R. Dean, M. M. Fogler and D. N. Basov, *Nature*, 2018, **557**, 530–533.

347 A. Woessner, M. B. Lundeberg, Y. Gao, A. Principi, P. Alonso-González, M. Carrega, K. Watanabe, T. Taniguchi, G. Vignale, M. Polini, J. Hone, R. Hillenbrand and F. H. L. Koppens, *Nat. Mater.*, 2014, **14**, 421.

348 H. Yan, X. Li, B. Chandra, G. Tulevski, Y. Wu, M. Freitag, W. Zhu, P. Avouris and F. Xia, *Nat. Nanotechnol.*, 2012, **7**, 330–334.

349 D. Wang, W. Wang, M. P. Knudson, G. C. Schatz and T. W. Odom, *Chem. Rev.*, 2018, **118**, 2865–2881.

350 Y. Hashimoto, G. Seniutinas, A. Balčytis, S. Juodkazis and Y. Nishijima, *Sci. Rep.*, 2016, **6**, 25010.

351 K. Yoshihara, M. Sakamoto, H. Tamamitsu, M. Arakawa and K. Saitow, *Adv. Opt. Mater.*, 2018, **6**, 1800462.

352 P. Li, I. Dolado, F. J. Alfaro-Mozaz, F. Casanova, L. E. Hueso, S. Liu, J. H. Edgar, A. Y. Nikitin, S. Vélez and R. Hillenbrand, *Science*, 2018, **359**, 892.

353 S.-H. Gong, F. Alpeggiani, B. Sciacca, E. C. Garnett and L. Kuipers, *Science*, 2018, **359**, 443.